

Practical application of molecular modeling in heterogeneous catalysis

Citation for published version (APA):

van Daelen, M. A. W. M. (1996). *Practical application of molecular modeling in heterogeneous catalysis*. [Phd Thesis 1 (Research TU/e / Graduation TU/e), Chemical Engineering and Chemistry]. Technische Universiteit Eindhoven. <https://doi.org/10.6100/IR470007>

DOI:

[10.6100/IR470007](https://doi.org/10.6100/IR470007)

Document status and date:

Published: 01/01/1996

Document Version:

Publisher's PDF, also known as Version of Record (includes final page, issue and volume numbers)

Please check the document version of this publication:

- A submitted manuscript is the version of the article upon submission and before peer-review. There can be important differences between the submitted version and the official published version of record. People interested in the research are advised to contact the author for the final version of the publication, or visit the DOI to the publisher's website.
- The final author version and the galley proof are versions of the publication after peer review.
- The final published version features the final layout of the paper including the volume, issue and page numbers.

[Link to publication](#)

General rights

Copyright and moral rights for the publications made accessible in the public portal are retained by the authors and/or other copyright owners and it is a condition of accessing publications that users recognise and abide by the legal requirements associated with these rights.

- Users may download and print one copy of any publication from the public portal for the purpose of private study or research.
- You may not further distribute the material or use it for any profit-making activity or commercial gain
- You may freely distribute the URL identifying the publication in the public portal.

If the publication is distributed under the terms of Article 25fa of the Dutch Copyright Act, indicated by the "Taverne" license above, please follow below link for the End User Agreement:

www.tue.nl/taverne

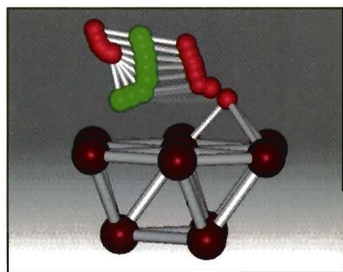
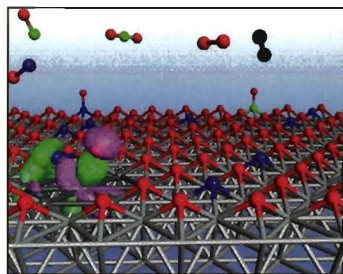
Take down policy

If you believe that this document breaches copyright please contact us at:

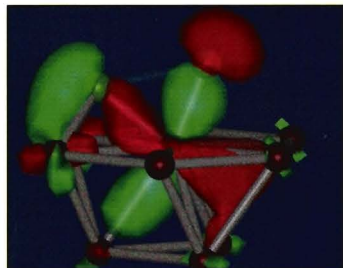
openaccess@tue.nl

providing details and we will investigate your claim.

Practical Application of Molecular Modeling in Heterogeneous Catalysis



Ton van Daelen



Practical Application of Molecular Modeling in Heterogeneous Catalysis

TECHNISCHE UNIVERSITEIT EINDHOVEN

Practical Application of Molecular Modeling in Heterogeneous Catalysis

PROEFSCHRIFT

ter verkrijging van de graad van doctor aan
de Technische Universiteit Eindhoven, op gezag
van de Rector Magnificus, prof.dr. M. Rem,
voor een commissie aangewezen door het Col-
lege van Dekanen in het openbaar te verdedigen
op dinsdag 22 oktober 1996 om 16.00 uur

door

Ton van Daelen

geboren te Waalwijk

Dit proefschrift is goedgekeurd door de promotoren:

prof.dr. R.A. van Santen

en

prof.dr. E.J. Baerends

Copromotor: prof.dr. J.M. Newsam



The work described in this thesis has been funded by Molecular Simulations Inc., San Diego.

CIP-DATA KONINKLIJKE BIBLIOTHEEK, DEN HAAG

Van Daelen, Ton

Practical Application of Molecular Modeling in Heterogeneous Catalysis/

Ton van Daelen. - Eindhoven :

Eindhoven University of Technology

Thesis Technische Universiteit Eindhoven. - With ref. -

With summary in Dutch.

ISBN 90-386-0298-7

Subject headings: molecular modeling / heterogeneous catalysis.

Every attempt to employ mathematical methods in the study of chemical questions must be considered profoundly irrational and contrary to the spirit of chemistry ... If mathematical analysis should ever hold a prominent place in chemistry - an aberration which is happily almost impossible - it would occasion a rapid and widespread degeneration of that science.

Auguste Comte, Philosophie Positive, Paris, 1838

voor mijn ouders
voor Hilde

Contents

1	Introduction	1
1.1	Catalysis	1
1.2	Experimentation versus Modeling	3
1.3	Surface Reactivity from First Principles	4
1.4	In this thesis	6
	References	7
2	Practical Methods in Heterogeneous Catalysis	9
2.1	Background	9
2.2	A Cascade of Modeling Approaches	10
2.3	Catalyst Structure Determination	11
2.4	Modeling of Spectra	16
2.5	Modeling Physisorptive Phenomena	18
2.6	Conclusions	24
	References	25
3	Density Functional Methods in Materials Design	29
3.1	Abstract	29
3.2	Density Functional Theory: General Principles	30
3.3	Implementation Issues	32
3.3.1	Numerical Atomic Orbital Approach: DMol	34
3.3.2	Pseudopotential Plane-Wave Approach: Plane_Wave	35
3.3.3	Harris Functional Method: Fast_Structure/Simulated_Annealing	36
3.4	Implementation on Parallel Architectures	36
3.4.1	DMol	36

3.4.2	Plane-Wave	39
3.5	Applications	40
3.5.1	Structure and Energetics of Cu ₁₃ Clusters	40
3.5.2	Structure and Dynamics of Doped Fullerene Complexes	41
3.5.3	Electronic Structure Calculations of a Tris-Quaternary Ammonium Cation	44
3.5.4	Oxygen Defect Structure and Energetics in Bulk SiO ₂	45
3.5.5	Fast Structure/Simulated Annealing Applied to Transition- Metal Compounds	46
3.6	Summary	48
	References	49
4	NO and CO dissociation on Cu(100) and Cu(111)	53
4.1	Abstract	53
4.2	Introduction	54
4.3	Methodology and Theoretical Background	59
4.3.1	Computational Details	59
4.3.2	Transition State Theory	62
4.4	Results and Discussion	64
4.4.1	Cluster Size Dependence: CO Top Adsorption	65
4.4.2	Reactant and Product States for the Surface Dissociation	68
4.4.3	Transition States for Dissociation	73
4.4.4	Normal Modes and Pre-exponential Factors	79
4.5	Conclusions	82
	References	83
5	Reactivity of Diatomic Molecules on Cu(100)	87
5.1	Abstract	87
5.2	Introduction	88
5.3	Methodology and Theoretical Background	90
5.4	Results and Discussion	93
5.4.1	CO and NO Dissociation	95
5.4.2	O ₂ and N ₂ Dissociation	100
5.4.3	Dissociation and Recombination Trends	104
5.4.4	Reaction Rates	105
5.5	Conclusions	107

References	108
6 Ethylene epoxidation on Ag(110)	111
6.1 Abstract	111
6.2 Introduction	112
6.3 Computational Details	114
6.4 Results and Discussion	116
6.4.1 Adsorption of Atomic Oxygen	116
6.4.2 Epoxidation of Ethylene	122
6.5 Conclusions and Recommendations	124
References	125
7 Selectivity of Dehydrogenation of α-Limonene	127
7.1 Abstract	127
7.2 Introduction	128
7.3 Methodology	129
7.3.1 Catalyst Preparation	129
7.3.2 α -Limonene Conversion	129
7.3.3 Simulations	131
7.4 Results and Discussion	131
7.4.1 Experimental	131
7.4.2 Simulations	133
7.5 Conclusions	136
References	137
Summary	139
Samenvatting	143
Dankwoord	147
Curriculum Vitae	149

Chapter 1

Introduction

1.1 Catalysis

Catalysis has long been and will continue to be a cornerstone of the chemical industry. Few chemical processes exist which do not, in one way or another, employ a catalyst to enhance efficiency, by increasing either the selectivity of a reaction or by lowering its energetic cost. Enhanced selectivity leads to production of more of the wanted products, and less of undesired products, sometimes as a result of a particular reaction route to the desired products being made available, something which would not occur without employing a catalyst.

The essence of catalysis is that the catalyst lowers energy barriers for certain pathways, making reactions possible, that would require severe reaction conditions without the help of a catalyst. Although the catalyst takes part in the reaction, it will by definition be largely unchanged after the reaction is finished and can therefore perform the same reaction again and again until deactivation processes lower the activity below practical levels.

A distinction can be made between homogeneous catalysis, that typically involves soluble compounds that are active in the same, liquid phase as the reactants, and heterogeneous catalysis, based on solid materials such as metals and metal oxides. The reactions take place here at the phase boundaries of the solid catalyst and the gaseous or liquid reactant phases.

An illustrative example of the catalytic principles is the decomposition of nitric oxides and carbon monoxide in automotive exhaust streams. Because these gases are environmentally damaging, conversion to non-hazardous gases is desirable. In the case of NO, this is ideally converted into nitrogen (N_2),

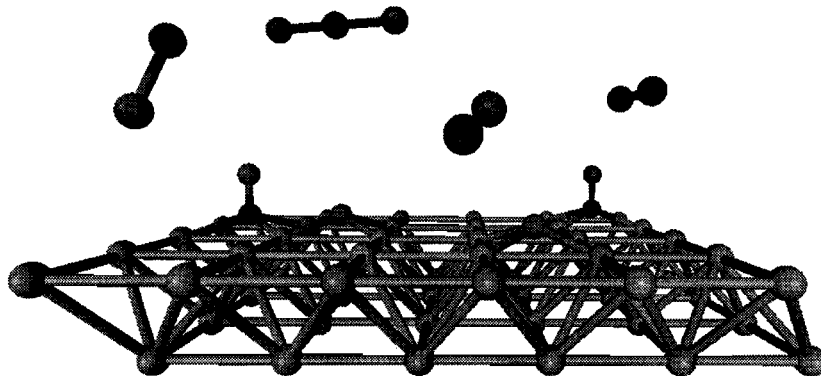


Figure 1.1. Reactants and products on a surface model of an automotive exhaust catalyst. Reactions take place after reactants adsorb from the gas phase. Reaction products desorb from the surface into the gas phase (see text).

and, when combined with carbon monoxide, into carbon dioxide (CO_2), a common component of the earth's atmosphere. The essential reaction step appears in many cases to be the dissociation of the N–O bond to form surface atoms that can then recombine on the catalyst surface to produce the environmentally friendly products. The NO bond is comparatively strong (162 kcal/mol), and even at high temperatures in a car engine, it will not dissociate spontaneously. This is where the catalyst does its work. An energetically favorable route for NO dissociation is for the molecule to first adsorb on a metal surface, after which the catalyst assists in breaking the N–O bond. The catalyst lowers the activation energy for bond breakage, so that isolated atoms N and O then become available on the catalyst surface. A diverse set of reactions on the surface can then follow, among which are those that form “clean” species like N_2 and CO_2 . These latter species are very stable compounds, i.e. low free energy; thermodynamics, therefore, favors their formation. The catalyst is needed to lower the energy barrier that separates the products from the reactants [1].

Another class of catalysts, in particular zeolites, base part of their effectiveness on the principles of shape selectivity. ZSM-5 is used commercially to convert ortho and meta isomers of xylene to the para isomer (Figure 1.2). The acid properties of the zeolite allow the isomerization of the xylenes. Should

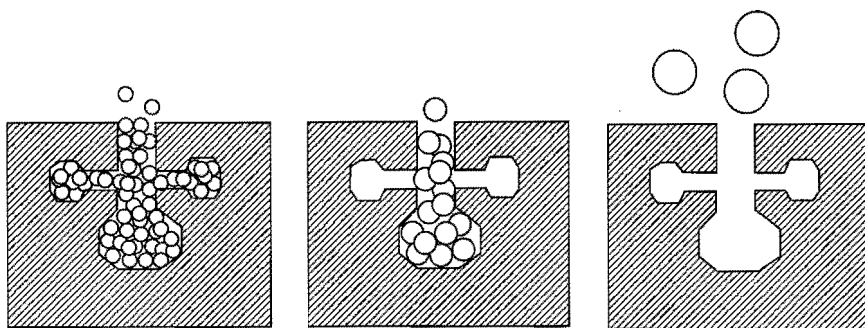


Figure 1.2. Schematic depiction of a porous catalyst. Some shape selective catalysts preferentially convert reactants that are able to diffuse into the pore system within which the catalytically active sites are located (see text).

this reaction be performed by a solid surface or by employing a homogeneous acid catalyst, the xylenes would be isomerized in thermodynamic equilibrium composition, and molecules that are much larger than xylenes would be converted. Now, in a microporous catalyst the reactions can take place selectively based on the very different diffusive properties for each molecule. The more branched ortho and meta isomers will stay longer in the zeolite channels and have a higher probability to react. Once these have reacted to form the straight para isomer, this form will diffuse out of the pore system relatively fast, resulting in a high degree of conversion towards the para isomer [2]. Molecules larger than xylenes will not enter the pore system and will not react.

1.2 Experimentation versus Modeling

For a catalyst to be commercially viable, important considerations are activity and durability. However, suitability for fundamental study is not a requirement and that has slowed down considerably the progress in the understanding of the basic mechanisms that govern the catalytic activity. Improvements in catalyst design over the years have been largely due to experimental trial and error procedures, relying heavily on equipment, material and human resources.

On the experimental side a lot has been learned about basic mechanism by means of surface science techniques applied to model catalytic systems

that resemble essential elements of the catalyst. These well defined systems allow careful study of a particular aspect of that system, but, at the risk of oversimplification. In addition, the conditions in these experiments usually differ from practical conditions. Many experiments are done at extremely low pressures which is sometimes considered a serious disadvantage. Nevertheless, the literature contains many examples where confident extrapolations from low-pressure studies to high pressure conditions have been made (see e.g. [3]).

Theoretical modeling fulfills in many respects a similar role as surface science experimentation has in the experimental community, as to first and foremost increase our fundamental knowledge of a complex catalytic system. However, the idealization serves different useful purposes. The physical state of the model catalyst can be accurately defined and controlled with a high degree of system uniformity. This definition allows one to study the effects of structure and composition on surface reactivity, or highlight particular aspects of the catalyst.

Questions that can be answered by applying modeling are typically of the *what if* kind:

- *What* will happen to the selectivity *if* the temperature increases.
- *How* is the stability of the catalyst affected *if* the pressure of the system is increased.
- *How* does the activation barrier for a metal surface reaction change *if* the surface is doped with a second metal.

Finding answers for such questions can gradually increase our knowledge about the catalyst that is being studied.

1.3 Surface Reactivity from First Principles

The innovative aspect of the studies described in this thesis is the determination of properties of transition states from a full optimization of its geometry which is a prerequisite to consider reactivity (Figure 1.3). From the relative energy of the transition state with respect to the product and reactants states

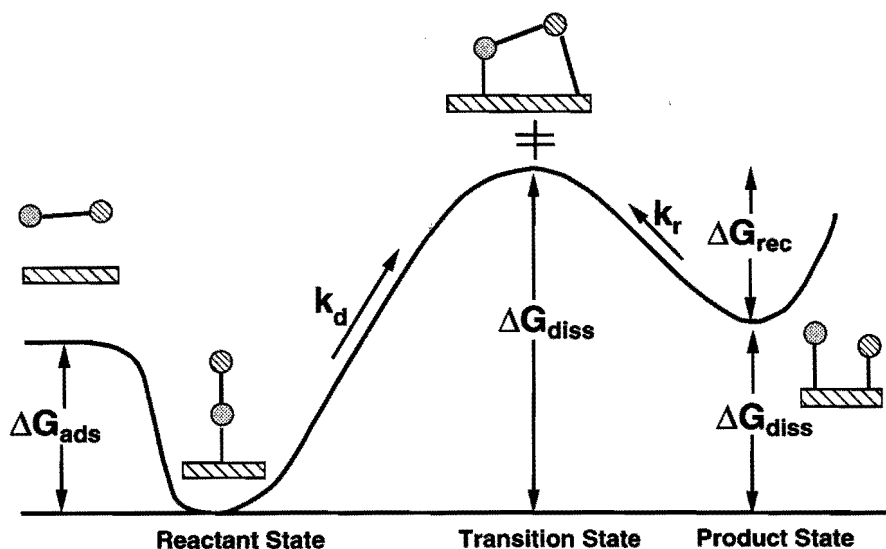


Figure 1.3. Schematic energy profile for a surface reaction. Indicated are the reactant, transition, and product states for a dissociation reaction, and the relevant thermodynamic and kinetic parameters.

one can derive the energy barrier that has to be overcome for the reaction to take place. This barrier defines the energetical component of the rate equation. The entropy contribution is concentrated in the pre-exponential factor of the rate equation and can be estimated by analyzing the partition functions of the transition and reactant states. These can be calculated from the vibrational properties of the system (Chapter 4).

Calculations are usually performed on cluster models representing single crystal surfaces. Location of a transition state structure is a computationally demanding procedure as it involves a large number of energy and gradient evaluations in order to locate a saddle point on a complex multi-dimensional potential energy surface. Calculations involving finite sized models are somewhat more efficient than “slab” approaches that incorporate periodicity, although this comes with the compromise of potential boundary effects [4]. Structure and vibrational properties are typically well described using the cluster approach, but care should be taken in interpreting the cluster energetics. Using larger clusters is a logical way to achieve higher accuracy, but this increases the computer time that is needed substantially. For the future it will be interesting to see whether the cluster or slab approach will be deliv-

ering the most accurate results while using not more computer time than is commercially practical. Improvements in theory have also gone hand in hand with increasing capacity of hardware. Calculations that were performed on a supercomputer like a CRAY-YMP a few years ago are now routinely done in the lab on modestly sized workstations.

1.4 In this thesis . . .

In this thesis we start with an overview of key facets of the contemporary applications of heterogeneous catalyst modeling. We will focus in later chapters on density functional calculations on reactions on metal surfaces. We also devote attention to a “classical” study of the diffusive behavior of sorbates in zeolites.

In Chapter 2 we review some molecular modeling techniques, not based on quantum mechanics, as applied to heterogeneous catalytic systems. We will show examples of modeling methods applied to catalyst characterization, physisorptive phenomena, and catalyst reactivity.

In Chapter 3 we describe the theoretical principles of density functional theory, in particular the implementation in the programs *DMol*, *Plane_Wave*, and *Fast_Structure/Simulated_Annealing*. We will address parallelization of some of the codes to multi-processor platforms and discuss applications to new materials, e.g. the structure and dynamics of doped fullerene complexes, the structure of a tris-quaternary ammonium zeolite templating agent, and an oxygen defect structure in bulk quartz.

Applications of density functional theory in a number of diverse areas are described in the following chapters, reflecting the current state of the art in surface reaction modeling. Chapter 4 describes two important steps in the NO decomposition process over Cu(100) and Cu(111) surfaces. The transition states are described for the surface dissociation of CO and NO along various reaction pathways. The activation barriers indicate the energetically most favorable reaction pathways and explain differences in reactivity between the Cu(111) and Cu(100) surfaces. Entropy changes for the reactions are calculated by a vibrational analysis of transition, product, and reactant states. Classical transition state theory is used to calculate pre-exponential factors for the dissociation and recombination reactions.

Chapter 5 describes dissociation of the diatomics N₂, O₂, CO, and NO on three distinct surface sites on Cu(100). We analyze the geometries and

electronic structure of the transition states, describe the trends in reactivity for the different molecules, and compare the optimal dissociation pathway for the molecules.

Chapter 6 describes a study of the reaction mechanism of the epoxidation of ethylene on Ag(110) surfaces, in particular the promoting effect of chlorine on the epoxidation mechanism. We study the effect of the promoter on the surface bond strength of adsorbed oxygen atoms and on changes in the energy barrier for an ethylene molecule approaching the surface. We also analyze how the location of chlorine affects its promoting activity.

Lastly, we describe in Chapter 7 a combined experimental and theoretical study to investigate the diffusion of cymenes in a ZSM-5 and zeolite-Y catalyst.

References

- [1] K.C. Taylor, *Catal. Rev.-Sci. Eng.* **35**, 457 (1993).
- [2] J.G. Wang, Y.W. Li, S.Y. Chen, and S.Y. Peng, *Catal. Lett.* **26**, 189 (1994).
- [3] H.J. Borg, PhD thesis, Eindhoven University of Technology (1995).
- [4] G. te Velde and E.J. Baerends, *Chem. Phys.* **177**, 399 (1993).

Chapter 2

Practical Methods in Molecular Modeling of Heterogeneous Catalysts¹

2.1 Background

The steady increase in computational power and graphics capabilities of modern computers coupled to the availability of these machines to the practical catalytic chemist, have rapidly advanced the field of atomic level computer modeling. The application of atomistic modeling and simulation is most mature in the life sciences sector in the fields of macromolecular structure research and rational drug design. More recently, the area of heterogeneous catalysis modeling has undergone significant growth. Computer visualization and computation are now routinely used as a first step in developing fundamental knowledge of a complex catalytic system.

From the viewpoint of modeling applications it is useful to distinguish between three major types of solid catalysts each of which warrant a different modeling approach. Metal oxides and zeolites have been the focus of most of the early efforts in the area of catalysis modeling. An underlying reason is that a mature classical theoretical framework exists that allows an adequate description of the structural characteristics of the oxide structure. Interactions between molecules and the oxidic catalyst can usually be described in simple terms of Coulomb and van der Waals interactions, making them

¹M.A. van Daelen, C.M. Freeman, and J.M. Newsam, to be published.

suitable for rapid classical simulations of the sorbate–catalyst interactions. In addition, modeling can complement experimental and analytical crystallographic techniques like powder diffraction and Rietveld refinement to identify catalyst structure. These methodologies are reviewed in this chapter.

Progress in the modeling of metal catalysts has traditionally been slower resulting from the fact that metal–metal and metal–adsorbate interactions are typically complex. With few exceptions methods used to describe these interactions are non–classical, involving rigorous quantum calculations. One popular quantum technique is based on density functional theory which combines an accurate energetic and structural description with reasonable computational efficiency. This method is reviewed and some applications are described in the following chapters.

In the current chapter we present an overview of the current state of the art of computational catalyst design that is not based on quantum mechanics. We focus on three major areas: *catalyst characterization*, *modeling of spectra*, *physisorptive phenomena on catalyst surfaces*, and *catalytic reaction modeling*. We discuss these areas by means of a few exemplary areas that illustrate part of the breadth of application of atomistic simulation. We will present results of recent work rather than present details on computational methods that are amply covered by excellent textbooks and overview articles [1, 2]

2.2 A Cascade of Modeling Approaches

Because of the complexity of most practical heterogeneous catalysts, the application of atomistic modeling and simulation methods has traditionally been slow. Our understanding of the detailed chemistry that takes place at the surface of a heterogeneous catalyst is typically modest, providing an incentive for the development of new methods and approaches to fill in the pieces that are missing in the complex, overall picture. Molecular modeling can complement experiment at different levels, and is often used to improve our knowledge of basic catalytic properties. As we understand more about the catalyst of interest we can increase the degree of sophistication of the modeling technique to be applied (Figure 2.1).

As with experiment, one strives to apply the appropriate tools to answer key questions. It is important that these questions have been clearly identified and prioritized in order to operate most efficiently. The tool that is to

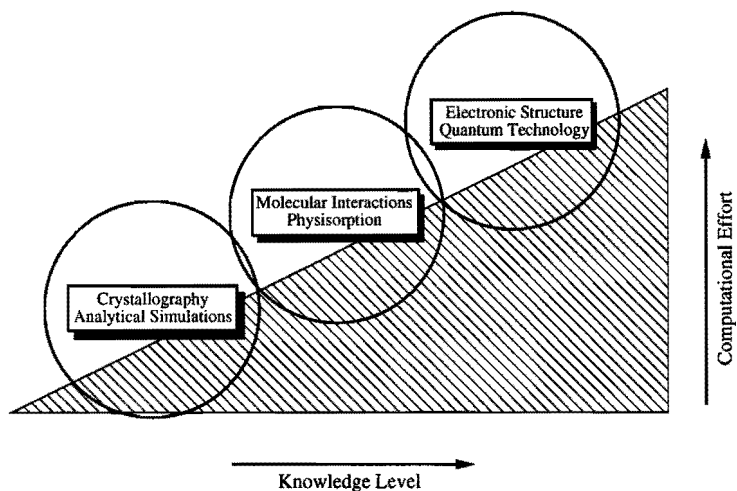


Figure 2.1. Modeling wedge

be applied is the one that is the simplest and most direct approach to solve that question, while neglecting unnecessary detail or complexity.

2.3 Catalyst Structure Determination

Many heterogeneous catalysts are based on crystalline solids. Modeling tools applied to these materials make use of crystallographic principles that allow the construction and evaluation of new structural models. These methods include symmetry manipulations and displays, techniques for combining structural building blocks such as cages, polyhedra and layers, and the automatic determination of space group symmetries from atomic models. These tools are now generally applied to zeolitic systems and, to a lesser extent, also to metal oxides.

Structure Simulation

Solid state materials can be described at the atomic level by constructing a suitable description of the potential energy of the system as a function of its geometrical structure. The most important use of such simulations is to function as a bridge between experimental measurements and structural

identification. This is based on a match between measured and computed spectra of experimental observables.

Classical methods can, in contrast to quantum mechanical techniques this neglects an explicit treatment of the electrons, now be applied to a wide range of solid systems. Different approaches can be used to construct the potential model. The *Born* model considers the atoms and ions in the system interacting by means of long and short range forces. This model has traditionally been used for modeling solids and ionic systems. The *shell* model is an extension to the Born model that takes into account electron polarizability of the system. This latter model is therefore better suited for more covalent frameworks as zeolites [2]. A third method is based on a description of the system in terms of a covalently bonded network. Here, the total energy is defined by potentials describing bond lengths, angles, torsions, and higher order terms. This is also known as the *forcefield* approach. It has traditionally been used in organic chemistry and biochemistry, but more recently also in oxidic systems [3, 4]. A non empirical extension to the shell model uses *ab initio* derived partial charges and dipole moments [5].

Computational simulation techniques have as their core expressions for the potential energy of the molecular system as a function of its configurational variables. In general the potential energy E_{pot} of the system can be represented as a sum of many-body terms of increasing order in number of particles:

$$E_{\text{pot}} = \sum_{ij} \frac{q_i q_j}{r_{ij}} + \sum_{ij} \Phi_{ij}(r_{ij}) + \sum_{ijk} \Phi_{ijk}(r_{ijk}) + \sum_{ijkl} \Phi_{ijkl}(r_{ijkl}) + \dots \quad (2.1)$$

The first term on the right hand side of Equation 2.1 describes the Coulomb energy; for periodic systems this sum may be evaluated using the Ewald technique [6, 7]. Subsequent terms are sums over all pairs, triplets, and higher order arrangements of particles. A generalized expression such as Equation 2.1 provides a convenient form for the evaluation of the potential energy of the solid system. In non-polar systems the long range Coulomb contribution may be small in comparison with the short range component of interaction energies and it may be practical to ignore this term. In the simulation of zeolite frameworks without hydrocarbon sorbates it may be possible to truncate Equation 2.1 simply at the two body term. These descriptions are an integral part of the structure determination process, as is demonstrated in the examples in the following section.

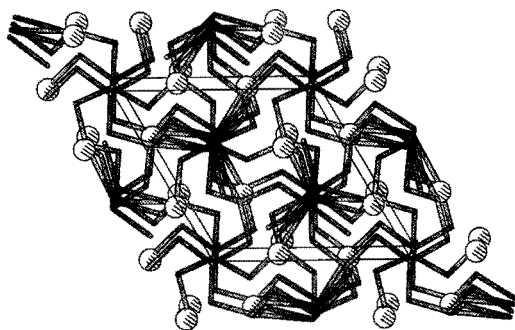


Figure 2.2. The framework structure of a new sodium zinc arsenate phase solved by simulated annealing.

Structure Solution

It is often straightforward to obtain a unit cell size and likely space group symmetry for a new crystalline material by indexing the powder X-ray diffraction pattern. Structure solution by simulated annealing is an important aid in the structure determination process [8] and is a good example of a new approach to a traditionally challenging problem that has become viable through developments in algorithms and hardware performance. Framework structure solution is the step of determining approximate positions for the tetrahedrally coordinated, heavy atoms (T-atoms) within the unit cell of a crystalline structure. After an initial structural model has been derived, modeling can also aid structure completion, the location of any structural components missing from the initial model.

At the heart of the simulated annealing process lies a function that quantifies the viability of a given arrangement of T-atoms in the unit cell. This shows similarity with the energy function used in ordinary annealing procedures as it is defined in terms of distances and angles between T-atoms. However, it may also include variables as T-atom coordination number, space group symmetry constraints, pore dimensions, or the difference between simulated and experimental powder patterns. The simulating annealing procedure uses Boltzmann statistics to cool the system down to its global energy minimum. The resulting structural models are then analyzed by visual inspection and oxygen atoms are filled in for structurally promising candidates. These models can then be further refined using crystallographic refinement programs such as DLS [9] that minimizes the structural model using a least squares procedure based on a set of target bond distances.

Using this approach the structure of a new sodium zinc arsenate phase

was successfully determined. Since this material was only produced in polycrystalline form, conventional crystallographic approaches to structure determination were not directly applicable. Application of a direct space approach to structure solution based on simulated annealing to this framework case yielded the correct framework model [10]. In this particularly favorable case, the required input were the input cell dimensions, lowest likely space group symmetry, $P6_3$, and the framework density; the entire structure solution process took about 30 minutes on a workstation (Figure 2.2). The effectiveness of this approach has also been demonstrated by test applications to the known structures of zeolites [8, 11] and other more condensed oxidic materials. When diffraction pattern matching constraints are included, simulated annealing appears to be a viable and potentially general route to *ab initio* structure solutions of polycrystalline inorganic materials [8, 11, 12, 13] and organic and organometallic systems [14].

Structure Refinement

An important part of crystal structure determination is the reproduction of the experimental powder pattern based on the crystal structure model and various instrument dependent parameters. The refinement process involves the optimization of structural and experimental parameters of an initial model so as to minimize the discrepancy between observed and simulated data. The difficulty in obtaining sizable single crystals for many materials has led to the development of methods for polycrystalline materials (i.e. powders). The method first developed by Rietveld [15] uses the complete experimental powder diffraction profile obtained by powder X-ray or neutron diffraction as the basis for structure refinement.

Structure refinement usually involves some strategy in application because of the many structural and instrumental parameters that can be refined. Refinable parameters include not only atom positional, thermal, and site-occupancy parameters but also parameters for the background, the crystal lattice, instrumental features, amorphous components and profile broadening factors such as crystallite size. Refinement usually proceeds iteratively until satisfying agreement between simulated and measured spectra is obtained. Powerful programs that encompass these algorithms are widely distributed and in a few cases integrated in a graphical user interface to display the observed, calculated, and difference plots [16, 17]. The value of the graphics capability is in most cases significant since errors in important parameters

can be recognized at once by visual inspection, which is difficult from numerical output alone. The graphical interface is then ideally used as the control panel from which the refinement process is guided.

Work exemplifying the combined effort of crystal structure simulation and structure refinement using the powder X-ray pattern was the determination of the structure of the high silica 10-ring zeolite NU-87 [18]. The unit cell dimensions, space group symmetry, and rough atomic positions were determined by inspecting the electron diffraction pattern. An initial refinement resulted in a model with some small discrepancies with the experimental X-ray pattern. This structure was then minimized using a shell model potential [19]. This resulted in a reduction of the symmetry from $Fm\bar{3}m$ to $P2_1/c$, the correct space group for this material. In a final refinement procedure the atomic positions were optimized in this space group, including the positions of extra framework water molecules. This work demonstrates that successful determination of crystal structure often involves a combination of different techniques.

Morphology

Transmission electron microscopy (TEM) is an important technique applied to catalyst samples to reveal particle size and shapes, and thermodynamical and kinetic factors that are at play during crystallization. Since small crystals have habits, when grown under equilibrium conditions, that are determined by the relative surface energetics, inspection of morphologies observed by TEM allows an estimate of the stability of the various single crystal surfaces. Alternatively, calculation of surface energetics using a viable potential model [2] can lead to a prediction of the morphology [20]. The interplay between TEM observations and prediction of surface stabilities is a means of addressing issues dealing with surface structure, in particular the effect of substituents on the stability of a surface. If a particular crystal surface exhibits enhanced catalytic activity one can design specific promoters that increase the stability of that particular surface, making it more pronounced in the macroscopic crystallite.

Inorganic surface structure simulation uses similar potential models for the simulation of bulk structure [2]. Methodologies explicitly targeted at surfaces have become available that can handle surface relaxation phenomena, and impurity segregation while effectively treating long range electrostatic effects [21].

Morphology control is a vital issue in many technological fields including thin coatings on iron surfaces for the production of stainless steel. Chromia, Cr_2O_3 , has a rhombohedral structure that is isomorphous with α -alumina. The preferred morphological appearance of chromia is plate like, which results in optimal binding to the iron surface and most efficient formation of a thin film. Simulation has been used to study the effect of Al^{3+} for Cr^{3+} surface substitution on the surface stability and, hence, the crystal habit [22]. Increasing the aluminum content was found to stabilize the [0001] faces, enhancing the plate like character of the crystal morphology. Inclusion of surface relaxation effects was found to be crucial for predicting these morphologies.

Predictions for metal morphologies have also been performed using surface energetics derived from parameterizations of first principles methods as, for instance, the embedded atom method (EAM) for fcc metals [23]. These methods have yet to be extended to more heterogeneous systems like alloys and metal oxides.

2.4 Modeling of Spectra

There is great practical value in obtaining a detailed understanding of the heterogeneous catalyst structure. However, due to the non-regularity of most systems, atomic level characterization is often difficult. Usually one has to rely on a combination of different analytical techniques since a single analytical method does generally not uniquely characterize the structure. Modeling methodologies that complement various analytical techniques applied to heterogeneous catalyst samples have proven to be of great importance in modern catalyst research. Recent advances have seen the application of simulation to such analytical techniques as infra-red spectroscopy (IR), solid state ^{29}Si -NMR, Extended X-ray Absorption Fine Structure (EXAFS), and Temperature Programmed Desorption (TPD).

The infra-red and Raman spectra of the lattice vibrational modes are sensitive and easily available observable characteristics of an oxidic material. Based on classical potential models, lattice modes of zeolites and metal oxides can be predicted from dynamical simulations or directly from the force constant matrix [2, 5, 24]. Spectral features in the far IR region (~ 40 – 350 cm^{-1}) are associated with non-framework cation motion and can suggest coordination geometries. Studies of the effects of modifications in structure or

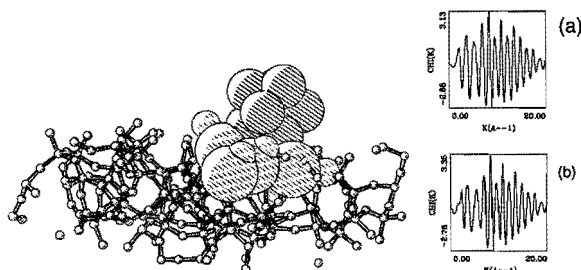


Figure 2.3. The simulated L-edge EXAFS spectra for (a) an octahedral Pt_6 cluster, and (b) an identical cluster supported on a vitreous silica surface.

composition on the simulated spectra can thus be associated with changes in the experimental spectra.

As an analytical technique that probes local coordination environments in a bulk sample, EXAFS can be simulated fairly accurately for 3D structural models. These simulations are based on a parameterization of *ab initio* single scattering EXAFS calculations, stored in a database for all elements of the periodic system [25, 26]. Such a parameterization allows quick interactive updates of the simulated spectra as the model is edited to investigate the effect of change in coordination of the adsorbing atom (Figure 2.3). Other techniques predict 3D structural parameters on the basis of an experimental EXAFS spectrum [27]. Whilst these methods are still relatively novel, requiring more specialist knowledge, they have already been successful in solving practical problems [28].

Another technique used to study coordination environments particularly in aluminosilicate zeolites is ^{29}Si NMR. Simulation of these spectra is based on a parameterization of empirical chemical shifts that incorporate both composition and geometric factors [29, 30]. This methodology estimates the chemical shifts with a sufficient degree of accuracy to aid in the assignment or interpretation of certain spectral features (Figure 2.4).

Simulation of temperature programmed desorption (TPD) spectra for metal-adsorbate systems has shown value as an aid in the interpretation of experimental desorption data. An overview on the theoretical approaches available for describing the kinetics of adsorption, diffusion, desorption, and reactions on metal surfaces can be found in references [31, 32, 33]. Almost all these approaches describe the binding between the adsorbate and the surface with simplified empirical expressions that have been parameterized using either *ab initio* or experimental results. Activation barriers that are important to describe the dynamics of such systems can also be described using bond

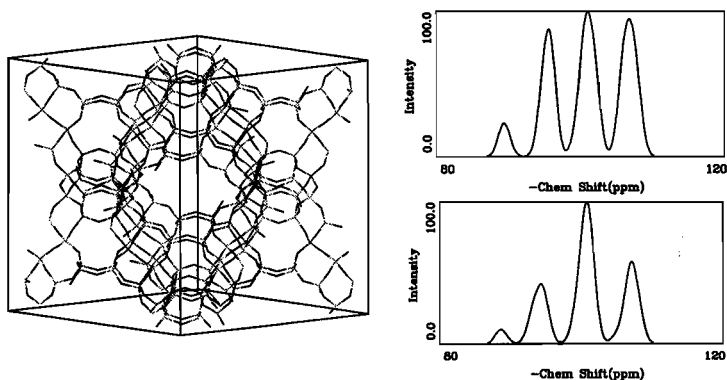


Figure 2.4. Simulated ^{29}Si NMR spectra for Faujasite framework materials with a pure SiO_2 composition (top), and for Si:Al ratios between 8.5 and 3.5 with random distributions in the framework subject to Loewenstein's rule of Al–O–Al linkage avoidance.

order conservation theory [34]. These methods have shown to be able to predict spectra in satisfactory agreement with experiment despite the complexity of surface–adsorbate interactions. However, quantitative agreement can only be obtained if accurate data for the individual processes is available, either from surface science experimentation or *ab initio* calculations.

2.5 Modeling Physisorptive Phenomena

Visualization Tools and Static Simulation

On a computer it is straightforward to build a series of complex zeolitic structures, and investigate the possibility of a steric fit of a guest molecule into the pores of that structure using energetics or simply via visual inspection. Some of these graphical tools are illustrated in Figure 2.5.

In addition to a graphical and geometrical analysis of steric factors controlling interactions between reactants and the solid catalyst, an evaluation of the potential energy of the *host–guest* system at varying levels of theory has become widely established. As discussed in Section 2.3 minimization of the potential energy of a zeolite or metal oxide framework is a means to optimize the structural topology. Recently, much attention has focused on interactions

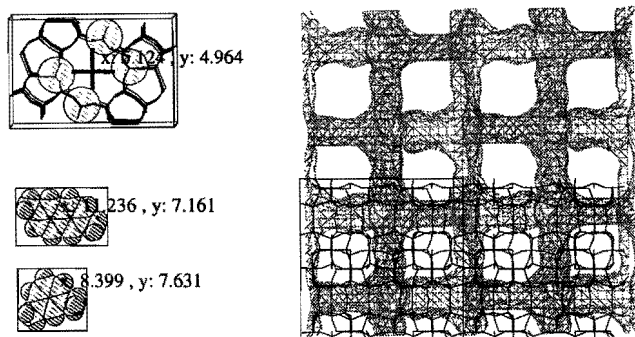


Figure 2.5. Graphical tools used to analyze a zeolite pore system. A pore ruler is used to inspect pore dimensions and cross dimensions of sorbates (left). On the right the volume of the zeolite pore that is accessible to a probe molecule of specific dimensions is visualized.

between the zeolite framework and either extra framework cations or organic molecules. In most cases a potential energy function is used that has been derived from *ab initio* or experimental data. These have been used extensively to simulate molecules in zeolites, for predicting low energy adsorption sites and diffusion properties. Conventional modeling of molecular systems at metal and semiconductor surfaces have almost exclusively been done at the quantum level. Only a limited number of these systems has been parameterized to work within a classical framework, and we have yet to reach the point that these simulations will provide predictive power in practical application areas.

The introduction of molecules into models designed to describe the zeolite framework does add some complexity. Many zeolite potential functions are based on a highly ionic description, where the nearest neighbor interactions (Si-O, Al-O) are represented largely by ionic forces. Conventional molecular mechanics, however, typically ignore electrostatic interactions between bonded atoms and use Coulomb interactions almost exclusively for the description of intermolecular rather than intramolecular interactions. Straightforwardly applying such an ionic potential may alter the interaction with a polar sorbate dramatically, necessitating a separation of the treatments of host-guest and framework interactions, or a more general approach to the potential parameter development [3, 4].

Pore Diffusion

Although molecular graphics provides a qualitative rationalization of the observed differences in diffusion, a quantitative description would demand a detailed molecular dynamics study. With the assistance of modern molecular modeling procedures, diffusion mechanisms can be extracted from the temporal evolution of the system. However, the use of molecular dynamics calculations is limited when studying diffusion processes. A simulation extending to the nanosecond domain will entail on the order of 10^6 energy and derivative calculations which is still a considerable computational investment. Large sorbates can, however, diffuse more slowly than can be accessed by such lengthy calculations.

Several strategies are evolving to alleviate these problems. By making assumptions about possible diffusion pathways it is possible to use constrained minimization and vibrational analysis methods in investigating the transport properties of sorbates in zeolites. Here it is possible to probe transport too slow to be accessible to molecular dynamics calculations at the expense of detailed mechanistic information. These calculations are really looking at the thermodynamic component of pore diffusion rather than the kinetic aspect. Several workers have removed the structural flexibility of the zeolite from the simulation [35]. This has the effect of focusing computational effort on the diffusing entity rather than the host lattice. However, there is evidence that framework flexibility influences the motion of sorbed species [36].

Subtle changes in either host or guest molecule can have dramatic effects on intra-zeolite processes. For example, trimethylbenzene diffuses around 1 million fold more slowly in zeolite ZSM-5 than the para-dimethylbenzene molecule. The origin of this dramatic difference is readily apparent when the size and shape of both guest molecules are compared with the pore dimensions of ZSM-5 using interactive molecular graphics. Trimethylbenzene is unable to fit within the lattice without significant strain, and, furthermore, this strain must be increased in the process of diffusion. In contrast the para-dimethylbenzene (p-xylene) molecule fits neatly into the channel structure of the zeolite and it can be seen that diffusion is not significantly sterically hindered.

Another example entails 2,6-isopropylnaphtalene (DIPN), a desirable precursor to performance polymers which is difficult to synthesize selectively or separately from the 2,7-isomer. Acid zeolites with potential for selective 2,6-DIPN synthesis were screened based on relative activation barriers for

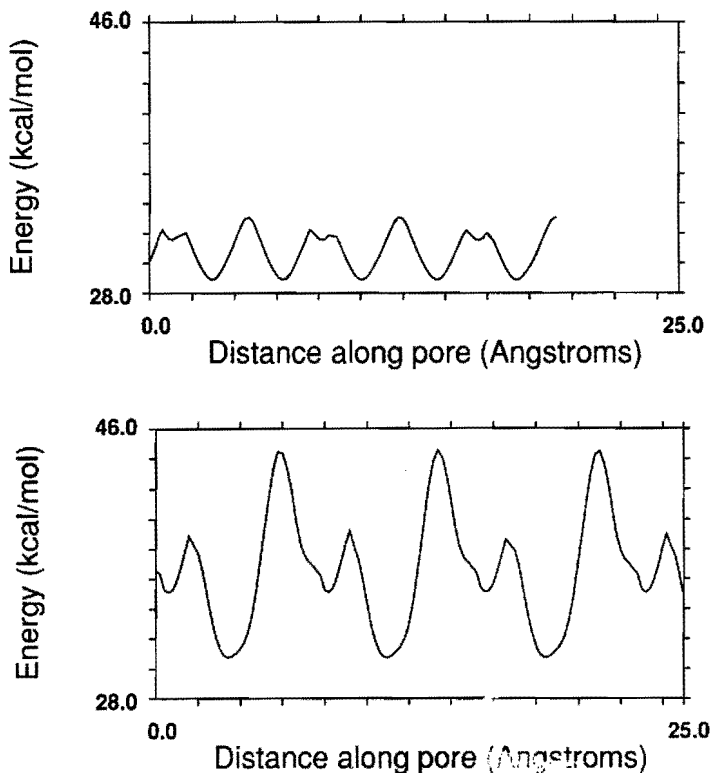


Figure 2.6. Minimum energy profile for diffusion of (a) 2,6-DIPN and (b) 2,7-DIPN in mordenite. The zero of energy corresponds to the empty zeolite plus sorbate in the ideal gas phase.

diffusion of the isomers along the zeolite channels. Reactor tests of mordenite gave a 2.7:1 selectivity for 2,6 versus 2,7 isomer production (Figure 2.6). In contrast, zeolite-L under the same conditions has marginal selectivity for the 2,7 isomers. These results correlate with the predicted relative diffusion barriers [37]. Modeling was efficiently used here to focus experimentation on the most promising candidates based on the simulation result.

Monte Carlo Docking

Since Equation 2.1 and its analogs provide the potential energy of the zeolite system for a given configuration we can use computational statistical

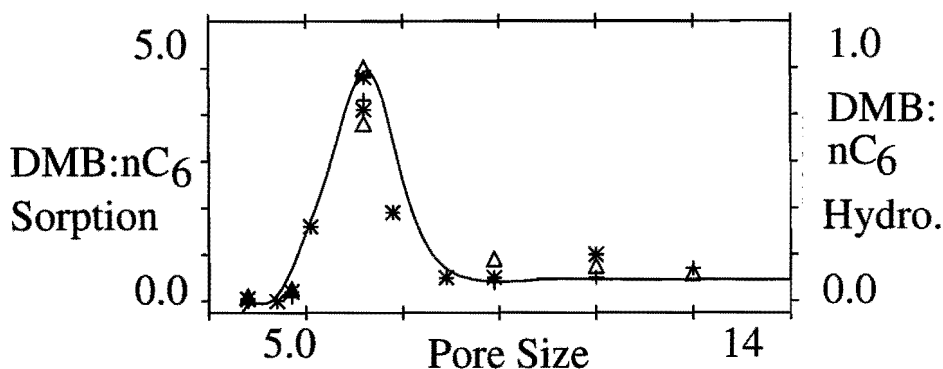


Figure 2.7. Experimental and calculated DMB:nC6 ratios of pore size in Å. Sorption experiments labeled (+), hydrocracking data (Δ), and calculated values (*). (With permission from [40])

mechanics to obtain thermodynamic information for a particular system. In practice the necessary configurational integrals are performed numerically using the Metropolis importance sampling scheme [38]. Such procedures have been extensively employed in the simulation of zeolite–sorbate interactions.

This approach has been used to study adsorption sites preferred by benzene in faujasite-type zeolites [39]. Recently, the same approach was applied to locate cation positions in zeolite-A and L [14]. This has traditionally been a challenging area because of the complexity of the interaction between cations and an aluminum containing framework.

Another practical example is the industrial exploitation of shape selectivity, where the steric constraints of the zeolite can exert a direct influence over the reactions catalyzed within its framework [40]. As in pharmaceutical modeling, molecular graphics and molecular modeling techniques are an effective tool for studying the shape selectivity imposed by a particular zeolite structure. However, the influence exhibited by the host lattice can be subtle. For example “inverse shape selectivity” is manifested for C6–C7 paraffinic hydrocarbons by molecular sieves containing void spaces of around 7 Å in diameter. Here molecules whose size and shape match the void space are preferentially sorbed over smaller or isomerically related molecules. Hence the shape selectivity is attractive in its action as opposed to the normal, repulsive or excluding selectivity.

Figure 2.7 also highlights the variation of the calculated and experimentally observed DMB:nC6 ratio as a function of void space size for a range

of molecular sieve structures. This figure shows the effect of inverse shape selectivity for structures with void spaces of about 7 Å which results from the preferential DMB sorption. This modeling study demonstrates that it is, in principle, now possible to examine the potential inverse shape selectivity of a given zeolite in advance of experimental investigation.

Sorption

Monte Carlo procedures within the grand canonical ensemble also provide a means of estimating the loading favored by zeolites interacting with potential sorbates at a particular temperature and pressure. Here, rather than simply displacing sorbate particles as in the standard Metropolis scheme, particle insertions and deletions are also made so that the number of sorbate molecules can evolve to equilibrium values appropriate to a specified sorbate chemical potential or partial pressure.

Sorption studies have been performed on N₂ and O₂ in zeolites to investigate the applicability in air separation [41], and on the adsorption behavior of CH₄ in zeolite-A [42, 43]. Good agreement with experiment in such studies can be obtained provided that the accuracy to which the interatomic interactions are described is sufficient. An important aspect of improving the quality of the simulations in this area is the validation of such potential functions based on *ab initio* calculations or fitting to experimental data. A potential for silica's, and alumina-silicate zeolites has been developed using a first principles approach [3, 4].

For larger molecules random Monte Carlo insertions into the zeolite lattice would infrequently result in an acceptable fit because the chance of overlap with one of the framework atoms grows sharply when the size of the molecule increases. A new procedure, configurational biased Monte Carlo (CBMC), has been developed that allow the molecule to "grow" in the zeolite channels in such a way that overlaps are avoided. Recent work addressed the docking of large hydrocarbons [44, 45, 46, 47, 48, 49]. Smit calculated adsorption isotherms for flexible alkanes (Figure 2.8) and observed a phase transition when at certain loadings the alkane chains "freeze" in the zeolite lattice to form a secondary network.

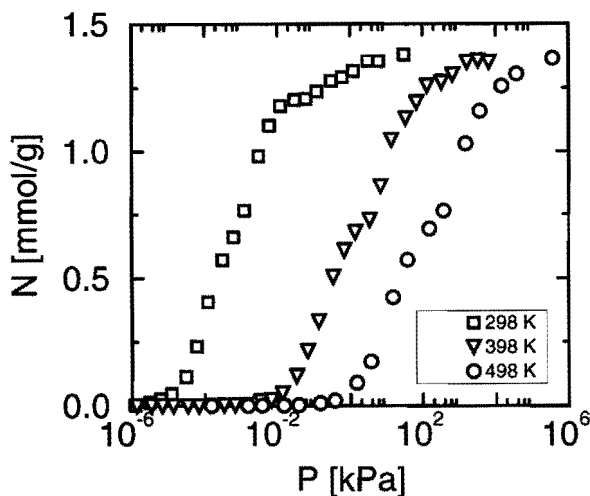


Figure 2.8. Temperature dependence of the adsorption isotherms of hexane in silicalite (With permission from [44]).

2.6 Conclusions

In this chapter we have reviewed typical modeling applications in heterogeneous catalyst research. Recent progress in this field has been substantial and has led to a wide range of successful application studies. Computational techniques now impact catalyst characterization, sorptive and electronic property determination, and rational materials selection and design programmes. As we have illustrated in the area of zeolite-sorbate interactions, computational protocols have now assumed a routine and practical role in the analysis of systems of industrial importance.

It is clear that modeling will grow in importance in catalytic research. This expansion will be driven by: improving accuracy in simulation techniques stemming from the development of reliable interatomic potentials, algorithmic improvements which extend the scope of simulation methodologies to greater length and time scales, and at a fundamental technical level, the inexorable advance of raw computational capabilities. Furthermore, the evolution of an open molecular modeling development environment, which permits the facile exploitation of innovative techniques through an advanced modeling infrastructure and a familiar and an easy-to-use interface, will undoubtedly extend the influence of computational methodologies.

The development of computational applications in catalyst rationalization and development, will also be underpinned by thorough study, development and validation of methods which focus on specific problem types. In this

thesis our major focus is that of gas-surface interactions, an area where ab initio molecular orbital theory offers the promise of considerably improved technical understanding and where direct experimentation is difficult. In the following chapter we review the theoretical basis of modern density functional theory, with a specific emphasis on its application to surface catalytic chemistry.

References

- [1] A.K. Cheetham and P. Day, eds., *Solid state chemistry: techniques*; Clarendon Press, Oxford (1987).
- [2] C.R.A. Catlow and W.C. Mackrodt, eds., *Computer simulation of solids*; Springer, Berlin (1982).
- [3] J.-R. Hill and J. Sauer, *J. Phys. Chem.* **98**, 1238 (1994).
- [4] J.-R. Hill and J. Sauer, *J. Phys. Chem.* **99**, 9536 (1995).
- [5] K. de Boer, A.P.J. Jansen, and R.A. van Santen, *Phys. Rev. B.* **52**, 12579 (1995).
- [6] P.P. Ewald, *Ann. Phys.* **64**, 253 (1921).
- [7] M.W. Deem, J.M. Newsam, and S.K. Sinha, *J. Phys. Chem.* **94**, 8356 (1990).
- [8] M.W. Deem and J.M. Newsam, *J. Am. Chem. Soc.* **114**, 7189 (1992).
- [9] W.M. Meier and H. Villiger, *Zeit. Kristallogr.* **129**, 411 (1969).
- [10] T.M. Nenoff, W.T.A. Harrison, G.D. Stucky, J.M. Nicol, and J.M. Newsam, *Zeolites* **13**, 506 (1993).
- [11] M.W. Deem and J.M. Newsam, *Nature* **342**, 260 (1989).
- [12] C.M. Freeman and C.R.A. Catlow, *J. Chem. Soc., Chem Comm.*, 89-91 (1991).
- [13] C.M. Freeman, J.M. Newsam, S.M. Levine, and C.R.A. Catlow, *J. Mater. Chem.* **3**, 531 (1993).
- [14] C.M. Freeman and J.M. Newsam, in: *Computer Modeling in Inorganic Crystallography*, to appear (1996).
- [15] H.M. Rietveld, *J. Appl. Cryst.* **2**, 65 (1969).
- [16] A.C. Larson and B. von Dreele, *Generalized Structure Analysis System*; Los Alamos National Laboratory, Los Alamos (1985).
- [17] D.B. Wiles and R.A. Young, *J. Appl. Cryst.* **14**, 149 (1981).
- [18] M.D. Shannon, J.L. Casci, P.A. Cox, and S.J. Andrews, *Nature* **353**, 417 (1991).

- [19] S.C. Parker, A.N. Cormack, and C.R.A. Catlow, *Acta Crystallogr. B* **40**, 200 (1984).
- [20] M.A. van Daelen, Characterize/Morphology module in InsightII, unpublished (1992).
- [21] D.H. Gay and A.L. Rohl, *J. Comp. Chem.* **91**, 925 (1994).
- [22] S.C. Parker, P.J. Lawrence, C.M. Freeman, S.M. Levine, and J.M. Newsam, *Catal. Lett.* **15**, 123 (1992).
- [23] M.S. Daw, S.M. Foiles, and M.I. Baskes, *Mat. Sci. Reports* **9**, 251 (1993).
- [24] A.J.M. de Man and R.A. van Santen, *Zeolites* **13**, 269 (1992).
- [25] J.J. Rehr, J.M. de Leon, S.I. Zabinsky, and R.C. Albers, *J. Am. Chem. Soc.* **113**, 5135 (1991).
- [26] Excurve package, Daresbury Laboratory, U.K.
- [27] M. Vaarkamp, I. Dring, R.J. Stern, and D. Koningsberger, *Phys. Rev. B* **50**, 7872 (1994).
- [28] M. Vaarkamp, B.L. Mojet, M.J. Kappers, and J.T. Miller, *J. Phys. Chem.* **99**, 16067 (1995).
- [29] J.M. Newsam, *J. Phys. Chem.* , p. 2002 (1985).
- [30] G. Engelhardt and D. Michel, *High Resolution Solid State NMR of Silicates and Zeolites*; Wiley, Rochester (1987).
- [31] S.J. Lombardo and A.T. Bell, *Surf. Sci. Reports* **13**, 1 (1991).
- [32] J.W. Niemantsverdriet, *Spectroscopy in Catalysis: an Introduction*; Weinheim, New York (1993).
- [33] A.M. de Jong and J.W. Niemantsverdriet, *Surf. Sci.* **223**, 355 (1990).
- [34] E. Shustorovich, *Adv. Catal.* **37**, 101 (1990).
- [35] S.D. Pickett, A.K. Nowak, J.M. Thomas, B.K. Peterson, J.F.P. Swift, A.K. Cheetham, C.J.J. den Ouden, B. Smit, and M.F. Post, *J. Chem. Soc., Chem. Comm.* **94**, 1233 (1990).
- [36] P. Demontis and G.B. Suffritti, in: *Modelling of Structure and Reactivity in Zeolites*, C.R.A. Catlow, ed. Academic press, London, U.K. (1992).
- [37] J.A. Horsley, J.D. Fellmann, E.G. Derouane, and C.M. Freeman, *J. Catal.* **147**, 231 (1994).
- [38] N. Metropolis, A.W. Rosenbluth, M.N. Rosenbluth, A.H. Teller, and G. Teller, *J. Chem. Phys.* **21**, 1087 (1953).
- [39] L.M. Bull, N.J. Henson, A.K. Cheetham, J.M. Newsam, and S.J. Heyes, *J. Phys. Chem.* **97**, 11776 (1993).
- [40] D.S. Santilli, T.V. Harris, and S.I. Zones, *Microporous Materials* **1**, 329 (1993).

- [41] K. Watanabe and N. Austin, to be published.
- [42] R.Q. Snurr, A.T. Bell, and D.N. Theodorou, *J. Phys. Chem.* **97**, 13742 (1993).
- [43] R.Q. Snurr, A.T. Bell, and D.N. Theodorou, *J. Phys. Chem.* **98**, 5111 (1994).
- [44] B. Smit and T.L.M. Maesen, *Nature* **374**, 42 (1995).
- [45] B. Smit and J.I. Siepmann, *Science* **264**, 1118 (1994).
- [46] B. Smit and J.I. Siepmann, *J. Phys. Chem.* **98**, 8442 (1994).
- [47] B. Smit, S. Karaborni, and J.I. Siepmann, *J. Chem. Phys.* **102**, 2126 (1995).
- [48] B. Smit, *Mol. Phys.* **85**, 153 (1995).
- [49] B. Smit, *J. Phys. Chem.* **99**, 5597 (1995).

Chapter 3

Density Functional Methods as Computational Tools in Materials Design¹

3.1 Abstract

This chapter gives a brief overview of density functional theory and discusses three specific implementations: a numerical localized basis approach, a pseudopotential plane-wave method, and a fast structure code based on the Harris functional approach. Characteristic examples are described that encompass properties of Cu_{13} clusters, Li-, K-, and O-endo-hedral fullerenes, tris-quaternary ammonium cations as zeolite templates, and oxygen defects in α -quartz. The calculations reveal the energetically favorable structures (bond lengths estimated to be within $\pm 0.02 \text{ \AA}$ of experiment), the energetics of changes in the geometry, and the electronic structure underlying the bonding mechanisms.

Two of the codes were ported to machines with a parallel architecture. A characteristic DMol calculation on a 128-node nCUBE 2 parallel computer shows speedup of about 107 over a single processor. A plane-wave calculation on a unit cell with 64 Si atoms using 1024 nCUBE 2 processors runs about five times faster than on a single-processor CRAY-YMP.

¹This work has been published: *Density Functional Methods as Computational Tools in Materials Design*, Y. S. Li, M. A. van Daelen, M. Wrinn, D. King-Smith, J. M. Newsam, B. Delley, E. Wimmer, T. Klitsner, M. P. Sears, G. A. Carlson, J. S. Nelson, D. C. Allan, and M. P. Teter, *J. Comp. Aid. Mat. Des.* **1**, 199 (1993)

3.2 Density Functional Theory: General Principles

First-principles calculations are emerging as the preferred route for determining the geometric and electronic structures, and associated properties of bulk solids, surfaces, defects, atomic clusters, and molecules [1, 2], avoiding expensive experiments and ambiguous empirical calculations. These calculations provide a detailed understanding of the relationship between atomic-scale structures and the physical, thermodynamic, and chemical properties of such systems. Thus, first-principles calculations are likely to play an increasingly important role in future design of new materials.

Several factors have contributed to the present success of first-principles calculations of real materials problems. These include the development of density functional theory for describing the complicated interactions between electrons, efficient algorithms and implementations, and the development of techniques for calculating total energies, forces, and dynamics. Equally important is the availability and continuing evolution of high speed computers, in particular, fast workstations and parallel computers.

Density functional theory (DFT) in the local density approximation (LDA) [3, 4] offers computational advantages over Hartree-Fock based *ab initio* techniques of quantum chemistry due to the wider applicability of DFT, and its computational efficiency (approximately a third power dependence on the number of basis functions). The LDA, in particular in combination with nonlocal gradient corrections [5, 6], is quite accurate since electron correlation is included, which is especially important in metallic systems. These characteristics have made DFT now widely accepted in physics, chemistry, and materials science as a reliable and efficient *ab initio* technique for studying atomic scale phenomena. This method provides an opportunity for large scale electronic structure calculations on increasingly complex systems, which lead to deeper insights into material structures and properties at an atomic and electronic level.

The work of Hohenberg, Kohn, and Sham in the mid 1960's provides the foundation of modern density functional theory [3, 4]. They showed that the total energy of a system is a functional of the electron density and proved that the total energy, expressed as a functional of the electron density, is minimized for the ground state density. This theory is fundamentally different from the Hartree-Fock based *ab initio* approaches in the sense that the

electron density replaces the many-electron wave function as the fundamental physical quantity. The local density approximation provides a simple yet surprisingly accurate way to evaluate the exchange-correlation energy. DFT with the LDA forms the basis of a number of band structure codes for bulk solids and surfaces, which have evolved over the past decades. In the same period, the foundation was laid for atomic cluster and molecular codes using Slater type [7], Gaussian type [8, 9, 10], or numerical atomic basis functions [11, 12]. The implementation of analytic gradients into density functional computer codes [13, 14] made it possible to perform structure optimization efficiently. This feature is crucial for investigations of molecular structures which usually have many degrees of geometric freedom.

Nonlocal corrections or gradient corrected techniques [15, 16, 17, 18] were proposed to improve the accuracy of DFT total energies. These corrections give DFT an accuracy comparable to Hartree-Fock MP2 methods (successfully used by many quantum chemists) for a great variety of chemically and technologically important systems. A major step would be schemes in which the computational effort scales linearly and not with a third power as a function of system size. Such efforts are currently being pursued and include approaches such as the recursion technique [19, 20, 21], density matrix methods [22, 23], and a localized basis approach [24, 25].

In this chapter, we briefly review the density functional approach and present two specific implementations: a localized orbital, numerical mesh based code for molecules and clusters (DMol) [12, 26], and a pseudopotential plane-wave approach for periodic systems (Plane.Wave) [27, 28]. We also discuss some theory of the Fast_Structure/Simulated_Annealing code based on the Harris-functional [29, 30, 31], which is closely related to the density functional approach.

Characteristic applications are presented to demonstrate the capabilities of these approaches in predicting and simulating geometric structure and properties. The examples include metal clusters, molecular dissociation on metal surfaces, endohedral fullerenes, tris-quaternary ammonium cations, and oxygen defects in SiO₂. This chapter does not discuss other density functional solid state approaches such as methods based on augmented plane waves and scattering theory. These methods have been particularly successful for transition metals, magnetic materials, and even lanthanides and actinides. The interested reader is referred to reviews such as that by Wimmer *et al.* [32].

Density functional calculations are computationally intensive and require substantial computing time and memory storage, still limiting their application to rather small and perhaps over-simplified models. Currently, in a typical *ab initio* electronic structure calculation on a workstation or vector supercomputer, up to about one hundred atoms can be handled. A full geometry optimization of a system with 100 atoms might require more than 100 hours of computer time and over 100 megabytes of random access memory. The current generation of massively parallel computers offers the potential of gigaflop computational speeds and gigabytes of internal memory. These massively parallel computers will enable electronic structure calculations on more realistic models, provided that the potential performance gain can be realized by appropriate software engineering. The simulation of the 7x7 Takayanagi reconstruction of the Si(111) surface is one typical example [33, 34]. Here, we describe implementations of density functional codes on nCUBE 2 parallel computers, which demonstrates the feasibility and the performance of density functional methods on distributed-memory parallel computers.

3.3 Implementation Issues

Density functional theory uses a variational concept to derive the ground-state electronic structure of a given electron system. DFT is formally exact, but practical applications require approximations to describe the complicated interactions among the electrons. The local density approximation [3, 4] offers a simple, but surprisingly accurate solution. Within LDA, the total energy of a system can be expressed as,

$$E_t = \sum_i^{\text{occ}} \epsilon_i - \frac{1}{2} \int d\mathbf{r} V_C[\rho(\mathbf{r})]\rho(\mathbf{r}) - \int d\mathbf{r} V_{xc}[\rho(\mathbf{r})]\rho(\mathbf{r}) + \int d\mathbf{r} \epsilon_{xc}[\rho(\mathbf{r})]\rho(\mathbf{r}) + E_{ion,ion}. \quad (3.1)$$

Here, $V_C[\rho(\mathbf{r})]$ is the Coulomb potential due to the electron charge density $\rho(\mathbf{r})$ and $V_{xc}[\rho(\mathbf{r})]$ is a local exchange correlation potential [35] which is usually taken from a first-principles calculation on the electron gas [36, 37]. $\epsilon_{xc}[\rho(\mathbf{r})]\rho(\mathbf{r})$ is the exchange-correlation energy density and $E_{ion,ion}$ is the ionic repulsive energy. The electron density $\rho(\mathbf{r})$ and the LDA eigenvalues ϵ_i in the ground state can be obtained by a self-consistent solution of the Kohn-Sham equations [4],

$$\left[-\frac{1}{2} \nabla^2 + V_C(\mathbf{r}) + V_{xc}[\rho(\mathbf{r})] + V_N(\mathbf{r}) \right] \psi_i(\mathbf{r}) = \epsilon_i \psi_i(\mathbf{r}), \quad (3.2)$$

$$\rho(\mathbf{r}) = \sum_i^{\text{occ}} |\psi_i(\mathbf{r})|^2. \quad (3.3)$$

Here ψ_i is the i -th one-particle wave function (Kohn–Sham orbital) with eigenvalue ϵ_i , V_N represents the electron–nuclear attraction. A variational basis set is generally employed to represent the Kohn–Sham orbital ψ_i ,

$$\psi_i(\mathbf{r}) = \sum_{\mu} C_{i,\mu} \phi_{\mu}(\mathbf{r}), \quad (3.4)$$

where ϕ_{μ} is the basis wave function. Popular basis sets include plane waves, Gaussian orbitals, and Slater-type orbitals. Using a non-orthogonal basis set, the Kohn–Sham equations can be rewritten as a generalized matrix eigenvalue equation,

$$\sum_{\nu} H_{\mu,\nu} C_{i,\nu} = \epsilon_i \sum_{\nu} S_{\mu,\nu} C_{i,\nu}, \quad (3.5)$$

where

$$\begin{aligned} H_{\mu,\nu} &= \int d\mathbf{r} \phi_{\mu}^* H \phi_{\nu} \\ &= \int d\mathbf{r} \phi_{\mu}^* \left[-\frac{1}{2} \nabla^2 + V_C(\mathbf{r}) + V_{xc}(\mathbf{r}) + V_N(\mathbf{r}) \right] \phi_{\nu}, \end{aligned} \quad (3.6)$$

and

$$S_{\mu,\nu} = \int d\mathbf{r} \phi_{\mu}^* \phi_{\nu}. \quad (3.7)$$

are the elements of the Hamiltonian and overlap matrices, respectively. The major computational effort is the evaluation of these matrix elements and the calculation of the associated eigenvalues and eigenvectors. There exists a variety of approaches to achieve these tasks and we describe two particular schemes here: a localized orbital, numerical mesh based approach, and a pseudopotential plane-wave method. Because of the density dependence of the Hamiltonian matrix, it is necessary to solve Equation 3.5 using a self-consistent field (SCF) iterative procedure. There exist several schemes for achieving self-consistency. One approach is illustrated in the flow-chart in Figure 3.1. Typically, for an organic system, semiconductor or insulator, about ten iterations are required to obtain a convergence of $|\rho^{\text{out}} - \rho^{\text{in}}| < 10^{-5}$ electron/bohr³. For metallic systems, often 25–100 iterations are required because of charge fluctuations originating from a high density of states near the Fermi level. Generally, the deep core electrons do not play any role in the chemical bonding and can be eliminated in the SCF calculations by employing the frozen core approximation or the pseudopotential approach.

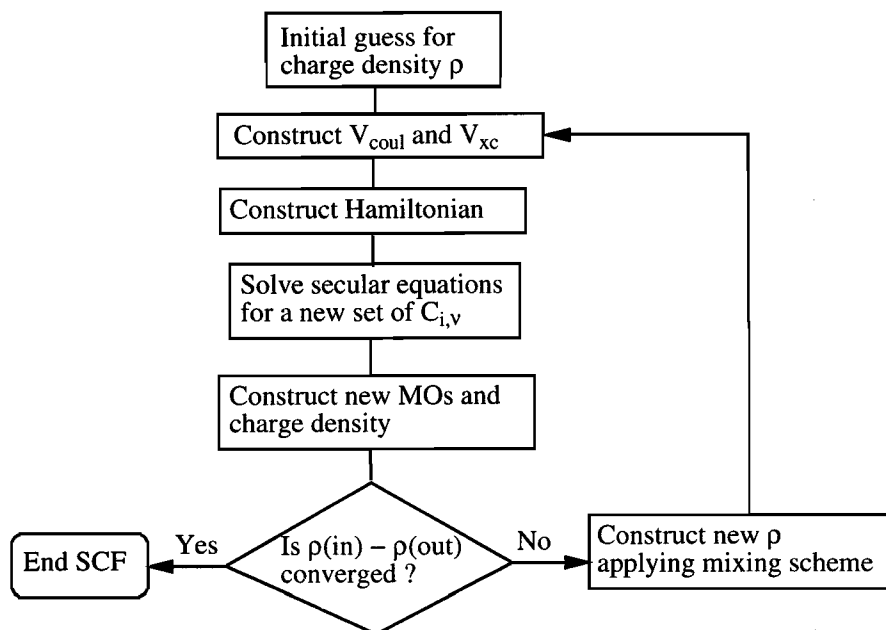


Figure 3.1. Self-consistent field (SCF) scheme used to solve the Kohn–Sham equations.

3.3.1 Numerical Atomic Orbital Approach: DMol

A vast experience in quantum chemistry shows that a linear combination of atomic orbitals (LCAO) provides an accurate, compact, and physically intuitive representation of electronic wave functions in molecules and clusters. The Kohn–Sham equations of DFT offer greater freedom in the selection of basis sets. The best atomic functions are the exact solutions of the Kohn–Sham equations for free atoms; they have automatically the correct shape close to the nucleus and at large distances. By construction, the dissociation limit of a molecule or cluster into free atoms is also correctly described.

DMol [12, 26] incorporates these features in an optimized and flexible implementation of density functional theory for isolated systems. This code employs numerically generated atomic wave functions as a basis set. The Hamiltonian and overlap matrix elements are obtained by numerical integration. To this end, a set of grid points is used to construct the Coulomb potential, charge density, Hamiltonian and overlap matrices, and the exchange–

correlation potential. The computational accuracy and time can be tuned by adjusting the number of grid points. The grid points are generated in a spherical pattern around each atomic center. Quasi-logarithmically spaced mesh points are used along the radial direction, which generate a set of spheres. On each sphere, the Lebedev scheme [38, 39] is used for generating the angular points. Typically, 1000 to 2000 mesh points per atom are used in DMol. This numerical mesh makes DMol a code which is well suited for a massively parallel computational environment. The electronic states are calculated using a straight matrix diagonalization in each SCF iteration. This approach is implemented entirely in real space; it is highly efficient and suitable for isolated molecules and atomic clusters. Finite cluster calculations can also be applied to studying aspects of extended systems, such as surface adsorption and dissociation processes, in which localized interactions play a dominant role, as will be shown below in the context of heterogeneous catalysis.

3.3.2 Pseudopotential Plane-Wave Approach: Plane_Wave

For extended systems which are periodic in three dimensions, delocalized plane-wave basis functions can be used to represent the Kohn-Sham orbitals, leading to a representation of the Kohn-Sham equations in momentum space [40]. This approach provides not only the total energies, forces, and charge densities, but also the detailed energy band structure. For systems with three dimensional periodicity, plane waves form a complete basis set to represent the Kohn-Sham orbitals. With proper choices, the Hamiltonian and overlap matrix elements are very simple and extremely fast to compute, since fast Fourier transform techniques can be used. However, a large number of plane waves is required even if the rapid oscillations originating from the nuclei and core electrons are replaced by a pseudopotential. Therefore, the break-through in the pseudopotential plane-wave methods came with the development of iterative methods [40] which avoid direct diagonalization of large matrices. In this iterative approach, key components of the computation include the operation of the Hamiltonian on the wave function, Gram-Schmidt (GS) orthogonalization of a large number of wave functions, and calculation of the charge density. Fast Fourier Transforms (FFT's) are used in the Hamiltonian operations and in computing the charge density from the plane-wave basis set. The pseudopotential approach has a long and estab-

lished history in studying semiconductors and simple metals. With newly developed pseudopotentials [41, 42, 43, 44], this method is being increasingly used to calculate properties of large and more complex semiconductor systems, with extension to oxides and transition metal compounds.

3.3.3 Harris Functional Method: Fast_Structure/ Simulated_Annealing

The development of a first principles method that predicts accurate structures at a lesser computational cost than correlated *ab initio* methods has been pursued for many years. A very promising procedure has come to be known as the Harris functional [29, 30, 31]. This functional possesses the same stationary points as the Kohn–Sham functional but the energy is now a maximum property. Maximizing E is then equivalent in this approach to minimizing Kohn–Sham orbitals. A maximum energy, however, can be obtained without the requirement of self-consistency, as is common in Kohn–Sham theory. The scheme has been improved by Lin and Harris [45], the most important innovation being the provision for charge transfer which proves crucial in general applications. Geometry optimization can be carried out either directly using for instance a BFGS scheme [46], with or without optimization of the charge parameters, or by dynamical methods.

3.4 Implementation on Parallel Architectures

In this section, we outline the implementation of DMol and the Plane–Wave code [47] on hypercube parallel computers. Benchmark calculation results are presented to illustrate the performance of the parallel decomposition schemes.

3.4.1 DMol

In Figure 3.2, we show the typical distribution of the computational tasks in DMol. It can be seen that the computationally demanding sections are the evaluation of matrix elements, followed by the construction of the charge density, the calculation of the Coulomb and exchange–correlation potentials on the mesh points and the matrix diagonalization. The limiting factor for memory usage is storage of all of the mesh points and the various quantities

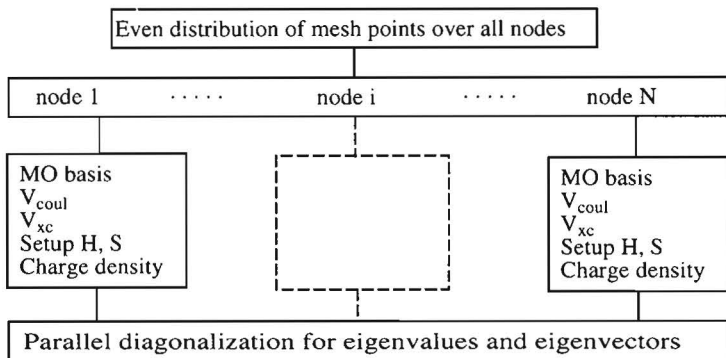


Figure 3.2. Parallelization scheme of DMol: the mesh points are evenly distributed across all the nodes. Matrix elements are distributed to each node using the torus wrap mapping method.

associated with each of the mesh points, such as the basis functions, the charge density and Coulomb potential. In a typical DMol calculation, 1000 to 2000 mesh points per atom are needed. Both the Hamiltonian and overlap matrices require a substantial amount of memory of the order of several megabytes.

Our parallelization strategy has involved the domain decomposition of mesh points and torus wrap mapping of the Hamiltonian and overlap matrices, as well as the eigenvectors [48]. This way, we can calculate all the physical quantities, in particular the contribution to the Hamiltonian and overlap matrix elements associated with each mesh point independently on each processor. This not only speeds up the calculation significantly, but also resolves the memory problem. Another advantage of this parallelization scheme is that we can limit the necessary extent of message passing by assembling the matrix elements instead of the charge density and various potentials from all the nodes. This procedure is outlined in detail in Figure 3.3.

There are many different mapping methods for parallelizing the matrix eigenvalue problem. Here we employ the torus wrap mapping to take advantage of its good load balancing [49]. To illustrate its efficiency, we show in Figure 3.4 the computational time for diagonalizing a 1000x1000 matrix as a function of the number of processors. The performance of the parallelized algorithms is shown in Table 3.1. It is clear that a significant speed improvement can be achieved using parallel computers with hundred or more nodes. It also is apparent that the performance of each node on the nCUBE 2 is

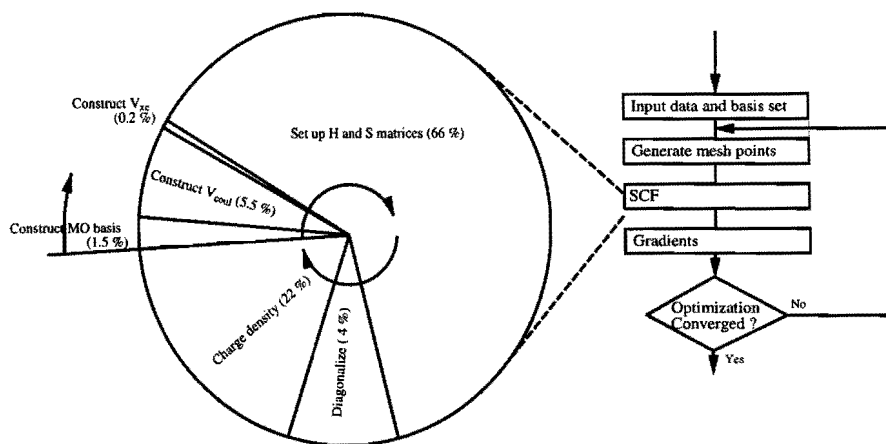


Figure 3.3. Distribution on a parallel platform of the major computational tasks in DMol, specifically the SCF cycle.

Table 3.1. DMol calculation time for one SCF iteration on nCUBE 2 parallel computers for a C_{20} cluster with 54686 mesh points and 280 basis functions. The calculated time needed for matrix diagonalization is also presented here. One can see that the time for diagonalization becomes insignificant for 128 processors because of the small matrix size. A similar calculation on a Silicon Graphics Indigo2 workstation takes about 10.8 min, on an IBM RS/6000 model 370 about 2.3 min, and on a single processor CRAY-YMP about 1.3 min. The DMol code has been optimized for SGI and IBM workstations and CRAY-YMP supercomputers.

Number of nodes	1	2	4	8	16	32	64	128
Total clock time (min)	129.0	64.6	32.5	16.3	8.1	4.1	2.2	1.2
Diagonalization (min)	3.62	1.90	1.06	0.57	0.38	0.22	0.16	0.12

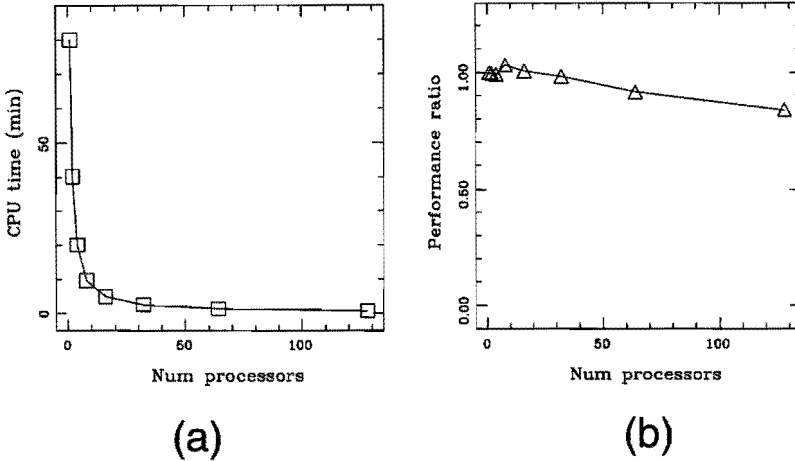


Figure 3.4. (a) The computational time (wall clock) needed to calculate all eigenvalues and eigenvectors of a 1000x1000 matrix as a function of the number of processors. (b) The performance ratio $R = \frac{t_1}{N \cdot t_N}$, where N is the number of processors, t_1 the total time needed on one processor, and t_N the total time needed on N processors.

rather slow compared with the SGI or particularly the IBM RISC processors. Thus, dramatic performance improvements can be anticipated with faster processing elements in the newer parallel machines, such as nCUBE 3.

3.4.2 Plane_Wave

In the iterative pseudopotential plane-wave method, the Fourier transforms and the calculation of the Hamiltonian matrix are the most time consuming components. The plane-wave coefficients and numerical grids associated with FFT's are the most memory demanding aspects. Our parallelization scheme thus consists here of a domain decomposition of the FFT grids and the plane-wave coefficients [47]. This allows for good node balancing and good memory usage. In Table 3.2, we list benchmark calculation results using this parallelized pseudopotential plane-wave code. It can be seen that the parallel code is about five times faster than that on a single processor of the CRAY-YMP for a solid state calculation with 64 Si atoms per unit cell.

Table 3.2. Calculation time for one SCF iteration on a 1024 node nCUBE 2 parallel computer as a function of the number of Si atoms in the unit cell. All the calculations are performed with one k point and a 10 Rydberg plane wave energy cutoff. For comparison, the timings for a single processor CRAY-YMP are also presented for the 8 and 64 atom unit cell cases.

nr. proc.	basis	bands	CPU (sec)	YMP (sec)
8	587	17	1.4	4.77
16	1173	33	3.8	
32	2335	65	12.9	
64	4625	129	51.3	226.1
128	9261	257	226.2	
256	18533	513	1160.8	

This performance, along with the ability to store large numbers of plane-wave coefficients and large FFT meshes, allows for a significant increase in the unit cell sizes up to several hundred atoms that can be investigated with this first-principles approach.

3.5 Applications

In this section, we describe a few selected applications. Using the DMol program, we show the results for the structure, dynamics, and catalytic properties of atomic and molecular clusters and metal surfaces. The energetics of an oxygen defect of bulk SiO₂ is presented as an example for using the Plane_Wave code.

3.5.1 Structure and Energetics of Cu₁₃ Clusters

Metal clusters play a key role in many materials and applications. For example, due to their large surface-to-volume ratios, small clusters are used as active components of many dispersed metal catalysts; the nucleation and growth of metal microclusters forms the basis of photographic processes; the special properties of small metal clusters, such as possible metal-insulator transitions, can be used in the design of novel sensors. These valuable characteristics warrant a detailed study of geometry, electronic structure, and related properties.

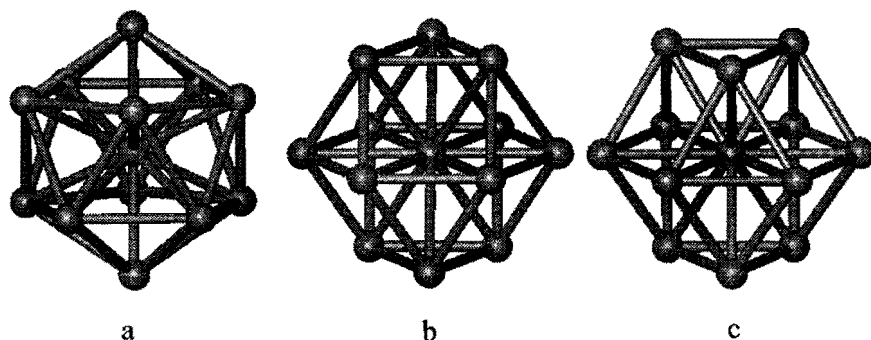


Figure 3.5. (a) Icosahedral, (b) fcc, and (c) hcp geometries for the LDA optimized structures of Cu_{13} clusters using the DMol program with a double numerical plus polarization basis set, frozen core, and medium mesh

We have used DMol to calculate the detailed structure of Cu_{13} clusters. We used numerical basis sets of double- ζ quality and additional polarization functions for Cu. The Von Barth–Hedin parameterization [50] of Ceperley and Alder’s homogeneous electron gas calculations [51] was used to describe the exchange–correlation energy. Becke–Perdew nonlocal gradient corrections [5, 6] were applied self consistently to the optimized geometries of the stationary points on the reaction paths. We focused our attention on the Cu_{13} clusters because of their potential catalytic applications and the possible icosahedral geometry. We have optimized the cluster structures from icosahedral, hcp, and fcc starting geometries, respectively. The final optimized configurations, shown in Figure 3.5, have binding energies of 33.4 eV for the hcp structure, 34.0 eV for the fcc structure, and 34.1 eV for the icosahedral geometry. The Cu–Cu bonds are significantly shortened compared to those in bulk copper. The calculations show that the icosahedral structure is the configuration with the lowest energy.

3.5.2 Structure and Dynamics of Doped Fullerene Complexes

The modification of Buckminster–Fullerene (C_{60}) complexes through internal “doping” to give endohedral complexes opens the door to tailoring the properties of these materials for a variety of novel applications ranging from high temperature superconductivity to carrier molecules for selective transport

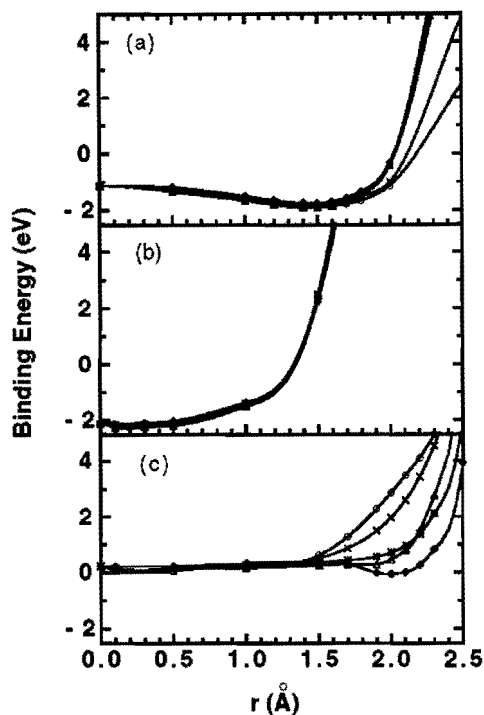


Figure 3.6. Calculated M-C₆₀ binding energy in M@C₆₀ endohedral complexes, as a function of the off-center distance of the enclosed atom. The results are given for (a) Li, (b) K, and (c) O based complexes. The high-symmetry displacement directions connect the center of C₆₀ and the C atom of the cage (Δ), the centers of the C-C single bonds ($*$), double bonds (\diamond), the centers of the hexagons (o), and the centers of the pentagons (x).

across membranes, and endohedral chemistry. We have studied the structure of these complexes and the interaction of encapsulated Li, K, and O atoms with the surrounding C₆₀ cage [52]. The differences in the bonding characteristics between different M@C₆₀ systems lead to significantly different low frequency angular motion ("rolling") and radial vibration ("rattling") modes of the enclosed atom.

The calculations are performed using the DMol code with a double numerical plus polarization basis and medium integration grid (for a detailed explanation of these computational parameters see Reference [52]). The M-C₆₀ interaction is determined in the following two steps. First, we freeze the C₆₀ cage and calculate the total energy while displacing the enclosed atom along several high symmetry directions, starting at the center of the cage. Next, we study the cage relaxation effect by optimizing the geometric structures of the cage with the enclosed atom. The detailed interaction potential is shown in Figure 3.6. We find that the Li atom in Li@C₆₀ is displaced away from the cage center by 1.5 Å due to the cage polarization effect. The K atom

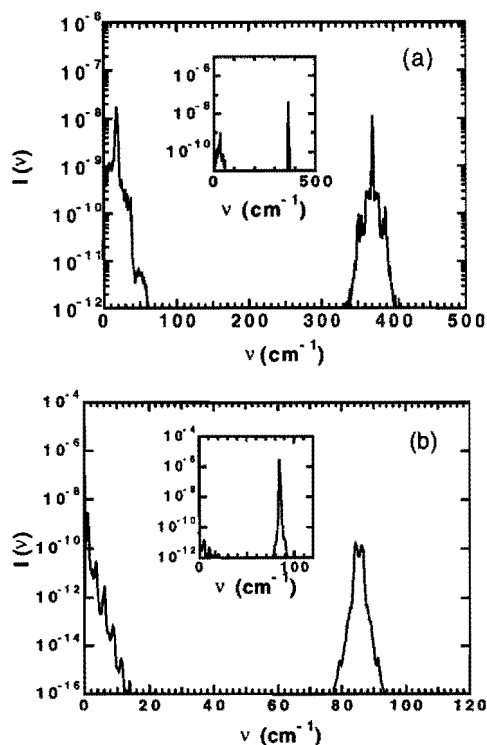


Figure 3.7. Vibrational spectra $I(\nu)$ of (a) Li in Li@C₆₀ and (b) K in K@C₆₀ at $T = 50$ K, obtained from quasi-classical molecular dynamics simulations using forcefield parameters tuned with the DMol results. The radial “rattling” modes, obtained from a radial projection of the atomic trajectories and shown in the inserts of (a) and (b), correspond to the high-frequency modes at 370 cm⁻¹ and 86 cm⁻¹ for Li and K, respectively. The low frequency peaks in the vibrational spectra correspond to the rolling modes of the encapsulated atoms.

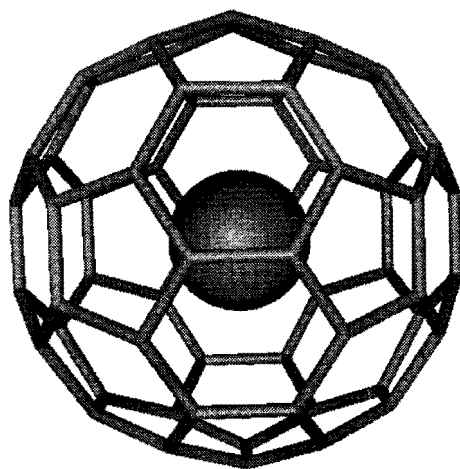


Figure 3.8. Equilibrium structure for K@C₆₀ optimized with DMol.

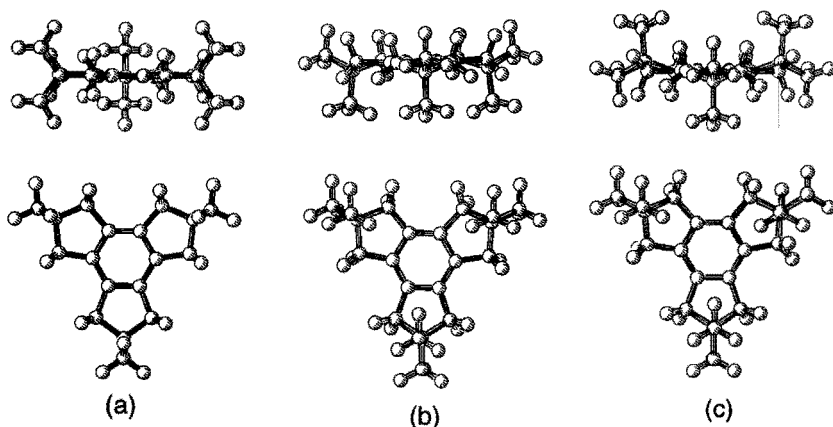


Figure 3.9. The results of LDA optimizations of the triquat molecular geometry: (a) D_{3h} , (b) C_{3v} , and (c) C_s symmetries. Both the top and side views are presented.

in $K@C_{60}$ is located in the cage center (Figure 3.8), and the endohedral O atom prefers to bind on a C=C bridge site by a strongly covalent bond which locally modifies the cage. The bonding configurations of the three complexes are quite different from each other. $K-C_{60}$ is ionic, $Li-C_{60}$ is moderately covalent, and $O-C_{60}$ is strongly covalent. We find that cage relaxation has little effect on the $Li@C_{60}$ and $K@C_{60}$ systems, due to the strong ionic interactions. For $O@C_{60}$, this cage relaxation stabilizes the system by 1.58 eV and significantly weakens the C–C double bond bridged by the oxygen atom, resulting in its elongation from 1.39 Å to 1.43 Å. As shown in Figure 3.7, these simple interactions lead to very different vibrational modes for the molecular complexes: high-frequency rattling and thermally activated rolling modes in $Li@C_{60}$, and low-frequency rattling and rolling modes in $K@C_{60}$. Due to the non-vanishing dipole moments of the endohedral complexes, these modes are predicted as observable in infrared spectra.

3.5.3 Electronic Structure Calculations of a Tris-Quaternary Ammonium Cation

The density functional approach can also be applied straightforwardly to organic systems. A tris-quaternary ammonium cation was first synthesized by

Ciric [53, 54] and is used as the template for the synthesis of zeolite ZSM-18 [53, 55]. The conformation of the organic moiety in the crystal structure of the tribromide dihydrate salt [54, 56] shows substantial puckering of the pyrrolium rings. Each nitrogen atom is displaced out of the aromatic ring plane by some 0.5 Å, yielding approximate C_{3v} symmetry. It is not clear how the crystal environment, in particular the electrostatic interactions, affects the molecular conformation. To this end, we have performed a series of first-principles DMol and Hartree-Fock calculations. From these electronic structure calculations, we have mapped out the detailed potential energy surface and the conformation energetics. As shown in Figure 3.10, the DMol calculations demonstrate that the D_{3h} conformation, in which the three quaternary nitrogen atoms are coplanar with the central aromatic ring, is a transition state. The C_{3v} conformation, with the three nitrogen atoms symmetrically displaced out of the plane, shows a puckering of the pyrrolium rings which is comparable to but smaller than that observed in the crystal structure of the tribromide dihydrate salt. However, this is only a local minimum; the global minimum has C_s symmetry with one pyrrolium ring puckered oppositely to the other two. The energy difference between C_{3v} and C_s conformations is small, 0.1 kcal/mol. The D_{3h} - C_s energy difference, the triple barrier to inversion, is 4.4 kcal/mol. These results agree well with the Hartree-Fock results. The low barrier to inversion and puckering allows substantial flexibility at a temperature of about 104°C at which the triquat cation is typically used to promote crystallization of zeolite ZSM-18.

3.5.4 Oxygen Defect Structure and Energetics in Bulk SiO_2

Recently, the pseudopotential program Plane.Wave [27] has been used to investigate the properties of the oxygen vacancy in α -quartz [57]. Understanding of this phenomenon has direct relevance to applications of quartz in optics. The calculations were performed on an orthorhombic 17 atom unit cell (a doubled hexagonal cell of α -quartz, with one oxygen defect per cell). The results presented here are for the defect in the +1 charge state. Brillouin zone summations were performed with a (2,2,2) Monkhorst-Pack mesh, which produced four inequivalent k-points, and the wave functions were expanded with a plane-wave kinetic energy cutoff of 60 Ry. The positions of the atoms were relaxed using the Hellmann-Feynman forces on the ions in

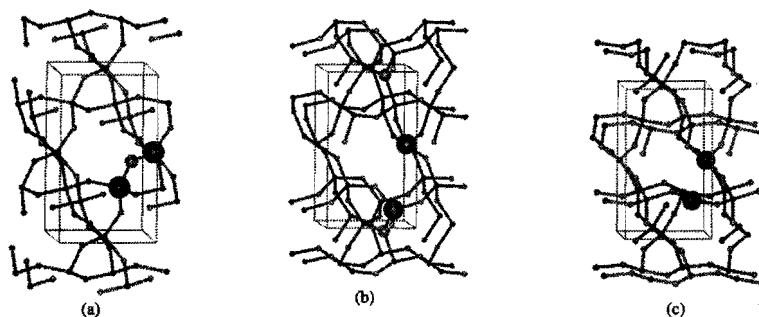


Figure 3.10. Ball and stick representation of bulk α -quartz (a) and oxygen defect structures: puckered (b) and dimer (c) configurations. The unit cell is shown in these figures by the boxes. In (a), the bridging oxygen atom (to be removed) and two nearby silicon atoms are highlighted by small and big balls, respectively. One can see the presence of three-fold oxygen atoms in the puckered configuration (b) and a weak Si-Si bond in the dimer structure (c). In (b), the three-fold oxygen atoms are shown as small CPK spheres.

combination with a BFGS relaxation scheme [58].

The calculations reveal two possible minima for the oxygen defect [57]. In the first conformation, the neighboring silicon atoms dimerize and create a weak Si-Si bond. The second configuration is produced by a puckering distortion of the crystal, and is illustrated in Figure 3.10. The puckered structure is stabilized by the presence of a 3-fold coordinated oxygen atom. The energy barrier between the two states was found to be about 0.5 eV. The barrier between the dimer and pucker conformations was not found in earlier cluster studies [59] but is reproduced in more recent studies of Snyder *et al.* [60] which use larger clusters. The calculations predict that the dimer configuration is higher in energy by 0.11 eV compared with the puckered structure.

3.5.5 Fast_Structure/Simulated_Annealing Applied to Transition-Metal Compounds

In a recent study the Fast_Structure/Simulated_Annealing code (FS/SA) was applied to determine the structure of the organometallic complex bis(N-methyl-5-nitrosalicylideneaminato) nickel(II) [61]. This is a square planar

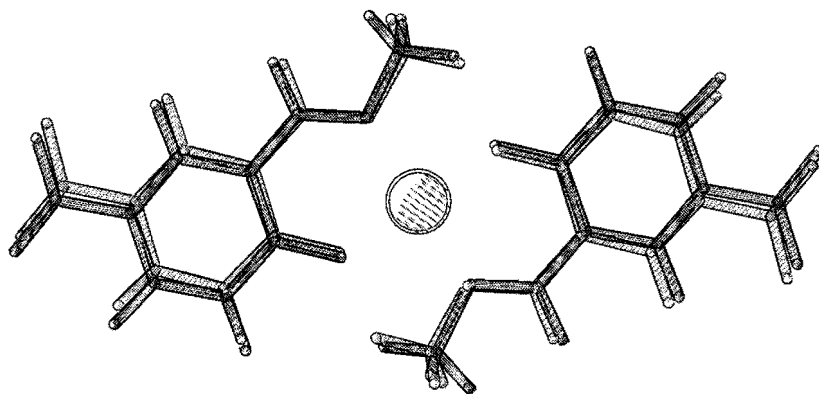


Figure 3.11. Experimental structure overlaid on the FS/SA optimized structure of bis(N-methyl-5-nitrosalicylideneaminato) nickel(II)

Table 3.3. Selected bond lengths and angles of the complex bis(N-methyl-5-nitrosalicylideneaminato) nickel(II) (With permission from reference [61]).

Parameter	DMol	FS/SA	exptl
r(Ni-N)	1.883	1.881	1.925
r(Ni-O)	1.815	1.816	1.826
r(N-CH ₃)	1.454	1.449	1.475
r(N-C)	1.299	1.264	1.296
r(O ₂ N-C)	1.434	1.397	1.449
r(O-C)	1.296	1.271	1.299
r(N-O)	1.239	1.239	1.225
r(C-C(benz))	1.412	1.390	1.431
r(C(benz)-C(benz))	1.417	1.366	1.411
∠(O-Ni-N)	93.4	91.2	93.2
∠(Ni-N-C)	124.8	125.9	124.8
∠(Ni-O-C)	131.0	128.6	131.0
∠(Ni-N-CH ₃)	121.3	119.4	120.4

compound with a total of 41 atoms [Figure 3.11]. From the picture it is clear that all the qualitative features of the experimental structure are reproduced. For a more qualitative assesment of the quality of the calculation selected bond lengths and bond angles are presented in Table 3.11 together with the DMol results. The FS/SA results are close to the DMol results, with a maximum difference of approximately 2%. The largest deviation can be found in the C–N bond of the nitro group and the O–Ni–N bond angle. Both DMol and FS/SA results are in satisfactory agreement with experiment. The FS/SA calculation, however, required only a third of the CPU–time needed for the DMol calculation. Improvements to the current FS/SA implementation are anticipated to substantially further increase this speed. The speed improvement over traditional DFT methods opens up exciting new application areas, for instance direct *ab initio* molecular dynamics.

3.6 Summary

We have outlined the methodology of density functional theory and its implementation in both the molecular localized orbital numerical and pseudopotential plane–wave approaches. We have highlighted electronic structure calculations on systems ranging from small Cu clusters, chemisorption on Cu surfaces, the structure and dynamics of doped fullerenes, the energetics of the conformations of a tri–quaternary ammonium cations to molecular dissociation processes on metal surfaces and defect structure and energetics in bulk materials. These examples illustrate the usefulness of density functional theory in materials simulations to predict geometric structures and the energetics of structural changes. DFT not only gives quantitative results for simulations that can be experimentally verified and, perhaps even more importantly, for unstable geometries (such as transition states, which are beyond the reach of experiments. Furthermore, the calculations provide insight and understanding of the underlying electronic structure effects. This knowledge sets the stage for the rational design of new materials.

To extend these powerful capabilities for studying larger and more complex models closer to real materials, we have implemented these density functional methods on massively parallel computers such as the nCUBE 2. The first benchmark calculations show a good speed improvement and node balancing. This indicates that such implementations on massively parallel

computers provides a real opportunity for large scale realistic materials simulations, especially as the performance of each processor increases.

References

- [1] Jozef T. Devreese and Piet van Camp, eds., *Electronic Structure, Dynamics, and Quantum Structural Properties of Condensed Matter*, Plenum Press, New York (1985).
- [2] J.K. Labanowski and J.W. Andzelm, eds., *Density Functional Methods in Chemistry*; Springer-Verlag, New York (1991).
- [3] P. Hohenberg and W. Kohn, *Phys. Rev. B* **136**, 864 (1964).
- [4] W. Kohn and L.J. Sham, *Phys. Rev. A* **140**, 1133 (1965).
- [5] A.D. Becke, *Phys. Rev. A* **38**, 3098 (1988).
- [6] J.P. Perdew, *Phys. Rev. B* **33**, 8822 (1986).
- [7] E. J. Baerends, D. E. Ellis, and P. Ros, *Chem. Phys.* **2**, 41 (1973).
- [8] H. Sambe and R. H. Felton, *J. Chem. Phys.* **61**, 3862 (1974).
- [9] B. I. Dunlap, J. W. D. Connolly, and J. R. Sabin, *J. Chem. Phys.* **71**, 4993 (1979).
- [10] D. R. Salahub, *Adv. Chem. Phys.* **69**, 447 (1987).
- [11] B. Delley and D. E. Ellis, *J. Chem. Phys.* **76**, 1949 (1982).
- [12] B. Delley, *J. Chem. Phys.* **92**, 508 (1990).
- [13] R. Fournier, J. Andzelm, and D. R. Salahub, *J. Chem. Phys.* **90**, 6371 (1989).
- [14] B. Delley, *J. Chem. Phys.* **94**, 7245 (1991).
- [15] J. P. Perdew, *Phys. Rev. Lett.* **55**, 1665 (1985).
- [16] J. P. Perdew and Y. Wang, *Phys. Rev. B* **33**, 8800 (1986).
- [17] A. D. Becke, *J. Chem. Phys.* **85**, 7184 (1986).
- [18] C. Lee, W. Yang, and R. G. Parr, *Phys. Rev. B* **37**, 785 (1988).
- [19] R. Haydock, *Solid State Phys.* **35**, 215 (1980).
- [20] M. J. Kelly, *Solid State Phys.* **35**, 295 (1980).
- [21] W. Zhong, D. Tomanek, and G.F. Bertsch, *Solid State Comm.* **86**, 607 (1993).
- [22] M. S. Daw, *Phys. Rev. B* **47**, 10895 (1993).
- [23] X.-P. Li, R. W. Nunes, and D. Vanderbilt, *Phys. Rev. B* **47**, 10891 (1993).
- [24] G. Galli and M. Parrinello, *Phys. Rev. Lett.* **69**, 3547 (1992).
- [25] F. Mauri, G. Gilla, and R. Car, *Phys. Rev. B* **47**, 9973 (1993).

- [26] DMol User Guide, version 3.0.0, Molecular Simulations, Inc., San Diego (1995).
- [27] M. P. Teter, M. C. Payne, and D. C. Allan, *Phys. Rev. B* **40**, 12255 (1989).
- [28] Plane-Wave User Guide, version 3.0.0, Molecular Simulations, Inc., San Diego (1995).
- [29] B. Delley, D.E. Ellis, A.J. Freeman, E.J. Baerends, and E.J. Post, *Phys. Rev. B* **27**, 2132 (1983).
- [30] J. Harris, *Phys. Rev. B* **31**, 1770 (1985).
- [31] W.M.C. Foulkes and R. Haydock, *Phys. Rev. B* **39**, 12520 (1989).
- [32] E. Wimmer, H. Krakauer, and A. J. Freeman, *Advances in Electronics and Electron Physics*; Vol. 35 , p. 357, Academic Press, New York (1985).
- [33] I. Stich, M. C. Payne, R. D. King-Smith, J-S. Lin, and L. J. Clarke, *Phys. Rev. Lett.* **68**, 1351 (1992).
- [34] K. D. Brommer, M. Needels, B. E. Larson, and J. D. Joannopoulos, *Phys. Rev. Lett.* **68**, 1355 (1992).
- [35] S. Lundqvist and N. H. March, eds., *Theory of the Inhomogeneous Electron Gas*; Plenum, New York (1983).
- [36] J. P. Perdew and A. Zunger, *Phys. Rev. B* **23**, 5048 (1981).
- [37] U. von Barth and L. Hedin, *J. Phys. C* **5**, 1629 (1972).
- [38] V. I. Lebedev, *Zh. Vychisl. Mat. Mat. Fiz.* **15**, 48 (1975).
- [39] V. I. Lebedev, *Zh. Vychisl. Mat. Mat. Fiz.* **16**, 293 (1976).
- [40] M.C. Payne, M. P. Teter, D. C. Allan, T. A. Arias, and J. Joannopoulos, *Rev. Mod. Phys.* **64**, 1045 (1992).
- [41] A. M. Rappe, K. M. Rabe, E. Kaxiras, and J. D. Joannopoulos, *Phys. Rev. B* **41**, 1227 (1990).
- [42] N. Troullier and J. L. Martins, *Phys. Rev. B* **43**, 1993 (1991).
- [43] D. Vanderbilt, *Phys. Rev. B* **41**, 7892 (1990).
- [44] M. Teter, *Phys. Rev. B* **48**, 5031 (1993).
- [45] Z. Lin and J. Harris, *J. Phys. Condens. Matter* **5**, 1055 (1992).
- [46] J. Baker, *J. Comp. Chem.* **7**, 385 (1986).
- [47] J. S. Nelson, S. J. Plimpton, and M. P. Sears, *Phys. Rev. B* **47**, 1765 (1993).
- [48] Y.S. Li, M.C. Wrinn, J.M. Newsam, and M.P. Sears, *J. Comp. Chem.* **16**, 226 (1995).
- [49] G. Fox, M. Johnson, G. Lyzenga, S. Otto, J. Salmon, and D. Walker,

- Solving Problems on Concurrent Processors*; Prentice Hall, New Jersey (1988).
- [50] U. von Barth and L. Hedin, *J. Phys. C* **5**, 1629 (1972).
- [51] D.M. Ceperley and B.J. Alder, *Phys. Rev. Lett.* **45**, 566 (1980).
- [52] Y.S. Li and D. Tomanek, *Chem. Phys. Lett.* **221**, 453 (1994).
- [53] J. Ciric, U. S. Patent 3 950 496, (1976).
- [54] J. Ciric, S. L. Lawton, G. T. Kokotailo, and G. W. Griffin, *J. Amer. Chem. Soc.* **100**, 2173 (1978).
- [55] S. L. Lawton and W. J. Rohrbaugh, *Science* **247**, 1319 (1990).
- [56] S. L. Lawton, J. Ciric, G. T. Kokotailo, and G. W. Griffin, *Acta Cryst.* **C41**, 1683 (1985).
- [57] D. C. Allan and M. P. Teter, *J. Am. Ceram. Soc.* **73**, 3247 (1990).
- [58] W. H. Press, B. P. Flannery, S. A. Teukolsky, and W. T. Vetterlin, *Numerical Recipes: The Art of Scientific Computing*; Cambridge University Press, Cambridge, England (1989).
- [59] K. R. Jayanta and W. B. Fowler, *Phys. Rev. B* **35**, 8223 (1987).
- [60] K. C. Snyder and W. B. Fowler, *Phys. Rev. B* **48**, 13238 (1993).
- [61] X.-P. Li, J. Andzelm, J. Harris, and A.M. Chaka, in: *Chemical Applications of Density Functional Theory*, B.B. Baird, R.B. Ross, and T. Ziegler, eds. , p. 388. ACS, Washington, D.C. (1996).

Chapter 4

Energetics and Dynamics for NO and CO dissociation on Cu(100) and Cu(111)¹

4.1 Abstract

The dissociation of NO and CO has been studied on cluster models representing the Cu (100) and Cu(111) single crystal faces using density functional quantum calculations. For each surface, several possible reaction paths are proposed, for which we fully optimized the reactant, product, and transition states at the local density level (LDA). Nonlocal density functional calculations (NLDA) were then performed on these optimized geometries. The clusters we used, varying in size between 10 and 31 atoms, produced dissociation barriers and energies that were reasonably well converged with cluster size. Classical transition state theory was used to calculate the rates of dissociation and recombination on the basis of computed frequencies of the predicted transition state and the reactant and product states. The transition states for NO and CO dissociation on all surfaces can be described as “tight” transition states corresponding to pre-exponentials for dissociation

¹This work has been published: *Transition States for NO and CO Dissociation on Cu(100) and Cu(111) Surface*, Y. S. Li, M. A. van Daelen, J. M. Newsam, and R.A. van Santen, *Chem. Phys. Lett.* **226**, 100 (1994); *Energetics and Dynamics for NO and CO Dissociation on Cu(100) and Cu(111)*, Y. S. Li, M. A. van Daelen, J. M. Newsam, and R.A. van Santen, *J. Phys. Chem.* **100**, 2279 (1996).

in the range 10^{10} – 10^{13} s⁻¹. The dissociation barrier for NO is significantly lower than that for CO. In addition, the more open Cu(100) surface is more reactive toward dissociation than the close packed Cu(111) surface. Nonlocal corrections to the LDA functional were found to have a small effect on dissociation barrier height, but the effect was found to be more profound on the recombination barrier and overall dissociation energies.

4.2 Introduction

The decomposition of NO_x species in traditional automotive catalytic converters by means of catalytic reduction has been the subject of many experimental and theoretical studies. Practical catalysts incorporate Rh and Pt, but the activity of Ru, Ni, and Cu has also been examined [1, 2, 3, 4, 5]. For an exhaust catalyst to be effective, it needs to facilitate the decomposition of NO_x species to atoms, which can then recombine to N₂. At the same time it should catalyze a nondissociative adsorption of CO followed by oxidation of adsorbed CO to CO₂. The dissociation of NO is often the rate limiting reaction step in this process [2, 6, 7]. The activity of Rh and Pt can be explained because of the low barrier towards NO dissociation while the CO barriers are high enough to preclude dissociation. The dissociation of CO itself is analogous to the NO dissociation and is of importance, among others, in the production of hydrocarbons from carbon monoxide and hydrogen, which are components of synthesis gas [8].

Progressively more stringent auto emission standards have necessitated the development of a new catalyst for NO reduction, most particularly, a catalyst that performs efficiently in the lean burn regime. Traditional catalysts, although sufficiently active in hydrocarbon (HC) and CO oxidation, deliver poor DeNO_x performance at these leaner levels. Converters with different catalysts for the oxidation and reduction stages are therefore being pursued. A promising candidate consists of zeolite supported copper clusters. In particular, the Cu/ZSM-5 system has shown extreme large activity toward NO reduction, orders of magnitude larger than systems based on other zeolites [9]. However, the mechanism of both their catalytic action and of their deactivation in the presence of water vapor is unknown. Also, the thermal stability of the zeolite framework is insufficient to make the application of this system commercially viable at present [10].

Additional research aimed at elucidating the mechanism and understanding how structural properties might affect the catalytic activity is needed for both zeolite- and metal-based catalysts. The first category is cumbersome to deal with computationally since little is known about the structure of the active sites in the zeolite. Metal catalysts are at this point more attractive since it is relatively well understood what the mechanism is for dissociation and what the structural properties are of the active centers. With the emerging of accurate and efficient quantum methods, this is a very attractive area to explore. In a span of about 5 years, the typical size of a metallic system that could be handled at the *ab initio* level has increased from a few (<5) to some 30–50 atoms at present. This allows the study of model systems of a size that is catalytically relevant, as was already shown for homogeneous catalytic systems by Ziegler [11].

Predicting the transition state and, hence, the energy barriers for the dissociation reactions on these metals is primary to determine their value as NO reduction catalysts. Studying the dynamical properties of these transition states allows, in addition, access to the rate for the reaction using transition state theory. The dissociation properties are closely related to the d-electronic structure of the metal, and therefore, elements neighboring those that are currently applied in the periodic system (Pt, Rh) are also principal candidates for effectively catalyzing the NO reduction. The present study concerned Cu, which is relatively easy to handle computationally since it is not a pure transition metal. In an ongoing study, we are addressing other metals like Ni [12].

There is ample experimental data available on the adsorption properties of NO and CO on copper surfaces. CO is known to adsorb linearly by the C-atom in low coordination sites on copper (111) and (100) surfaces, but the energy difference between different coordination sites is expected to be small [13]. This is supported by experiments showing that depending on coverage, a variety of sites are occupied by CO [14]. Molecular NO is usually adsorbed in a linear or bent configuration on top or bridge sites. However, dissociative adsorption is observed even at low temperatures [15, 16]. Ground-state vibrational frequencies have been measured using infrared-spectroscopy (IRS) and electron energy loss (EELS) techniques, providing information about frequencies associated with the metal-adsorbate bond stretching modes as well as the internal modes of the adsorbate. Also, bending modes of the adsorbate can be detected with EELS; however, the interpretation of intensities is

difficult because of competition in this low wavenumber range with atomic adsorbate modes and the surface phonon background.

The majority of the experimental data on reaction barriers and the dynamics of the dissociation process are of qualitative nature rather than quantitative. Balkenende *et al.* [17, 18] reported a higher activity for NO dissociation on the more open Cu(100) and Cu(110) surfaces than on the close-packed Cu(111) surface. In addition, they found the dissociation barrier for NO to be much lower than for CO; NO tends to adsorb dissociatively, while the barrier for CO precludes dissociative adsorption. Also for Pt, the (100) surface was found to be more active in inducing the dissociation of NO compared to the (111) surface [3]. Brodén *et al.* [19] made a comparison of available data for chemisorption of diatomic molecules and related the probability of the molecule to dissociate on a metal surface to the position of the metal in the periodic system. The height of the activation barrier decreases as one goes to the left in the periodic table. The transition from dissociative to associative adsorption is different for CO and NO (as NO dissociation barriers are usually lower) and is also a function of the surface geometry. Experimental pre-exponential factors for NO and CO dissociation measured on various metal surfaces lie within 1×10^9 and $1 \times 10^{12} \text{ s}^{-1}$ for diatomic dissociation reactions [20, 21]. These studies showed that the dissociation proceeds via a mechanism requiring a vacant nearest-neighbor site for the adsorbed diatomic. Kruse *et al.*, however, found a value of only 10^2 without observing this ensemble effect [22].

There are a number of theoretical studies on the energetics of CO and NO adsorption on copper surfaces. Post and Baerends [23] studied CO adsorption on small Cu clusters (1–7 atoms) using density functional theory and found reasonable agreement with experiment for bond distances and vibrational frequencies even for small CO/Cu_n systems. The adsorption energies, on the other hand, showed a strong dependence with cluster size, and for most clusters, they found hollow adsorption sites to be preferred over top sites. These results are due to the high degree of coordinative unsaturation of the cluster atoms compared to the bulk atoms. Typically, even a 10-atom cluster has only one atom coordinated to nine neighbors, similarly as in the bulk Cu(111) surface. In a recent study on CO adsorption on Cu(100), strong oscillations were reported for the CO binding energy on clusters up to 37 atoms [24]. These oscillations are found to be caused by very small changes in the density of states of clusters when the cluster size changes.

However, the clusters as used in their study consist predominantly of only a monolayer of metal atoms. Hence, the metal atom binding to the adsorbate is missing all neighbors in the second layer, resulting in unrealistic reactivity of this central atom. Bauschlicher has shown clusters with less than 14 atoms to be definitely too small, but clusters of 14–38 atoms to be possibly accurate. Siegbahn found a similar result; H on Ni₁₉(12,7) gives 27.5 kcal/mol and H on Ni₄₀(21,13,6) gives 46.5 kcal/mol, to be compared to experimental 63 kcal/mol. Siegbahn showed that oscillations in adsorption energies as a function of cluster size could be diminished by adsorbing on geometrically optimized clusters [25] or by exciting the cluster to a proper bonding state, reasoning that such a state would always be present at the extended surface [26]. The first procedure is valuable for studying cluster properties, but when bulk surfaces are studied, the optimized cluster geometry will usually distort from the bulk geometry, making them less appropriate to model an extended surface. Preparing the cluster for bonding is less practical for studying surface reactions since different stationary points on the reaction path might need different bond preparation for the cluster. We will address the issue of cluster size convergence in the present study, and we present clusters that give reasonable adsorption energies and good dissociation energetics.

Early studies on dissociation reactions on small clusters modeling metal surfaces involved hydrogen, and these delivered very valuable insights in the basic chemistry of molecules interacting with surfaces, notwithstanding the limited size of the clusters involved in these studies [27, 28]. More recently, Yang and Whitten [29] used a many-electron embedding theory to calculate barriers for H₂ dissociation on a Ni(100) surface, and obtained accurate bond energies, vibrational frequencies, and activation barriers for dissociation, and determined the site preference for H adsorption.

Earlier our group presented a quantum-chemical analysis of CO dissociation on different surfaces of Rh based on the ASED molecular orbital method, an adapted version of the semiempirical extended Hückel method [30]. This study permitted a qualitative description of the transition state for the surface dissociation and allowed a comparison of the activation barriers for dissociation along a number of different reaction paths. Dissociation follows a clear pattern. Starting from a position parallel to the surface normal, the oxygen atom tilts toward the metal surface and the C–O bond stretches. During this stretch, crossing of the C–O bond over a surface metal atom is favored. This maximizes the overlap between one of the 2π* orbitals of the

molecule and appropriate d orbitals on the metal atom. After dissociation, the carbon and the oxygen atom share the least number of surface metal atoms to minimize the repulsive interaction between the atomic species [31]. The study also indicated significant larger activity toward CO dissociation for a Rh(100) surface than for a Rh(111) surface. Van Langeveld *et al.* [32] performed extended Hückel calculations on CO dissociation on Ni(111) and found a dissociation barrier almost equal to the CO adsorption energy. A first attempt to model dissociation barriers for CO on copper surfaces was reported by Siegbahn, who performed MCPF calculations on CO adsorbed on a 12-atom cluster modeling a Cu(100) surface. A transition state for CO dissociation over a metal bridge site was approximated, resulting in a barrier of the order of 11 kcal/mol. While each of these studies provided useful information toward the qualitative understanding of metal catalyzed bond breaking in diatomics, the absence of a complete transition state optimization and limitations in the methods used precluded any quantitative energetics.

Recently, we have demonstrated the applicability of the density functional approach to predict the dynamic properties of transition states. Based on these results, the rate constant for the dissociative adsorption of methane on Ni clusters was computed [33, 34, 35], as well as the rate constant for hydrogen exchange and dehydrogenation of methane on a zeolitic acid site [36]. In the present study, we have applied the Density Functional approach to the dissociation of diatomics on single crystal copper surfaces represented by cluster models. We fully optimized the transition states with respect to all degrees of freedom for the adsorbate in the plane of symmetry. In addition to our recently reported study [37], we now also calculated the energetics by applying a Becke–Perdew nonlocal correction to repair the error in the exchange–correlation terms. Nonlocal corrections are routinely applied nowadays because they result in more accurate binding energies. In this study, we will investigate the importance of these corrections. The clusters we are using are also substantially larger than those that were used in the previous study in order to minimize finite cluster size effects. Having obtained one well-defined reaction path, we applied transition state theory to calculate the reaction rate constants for the dissociation and recombination along the particular path. We used a full vibrational analysis for all degrees of freedom of the adsorbate to calculate the partition functions for reactant, product, and transition states. We use this to estimate the entropy factor which

together with the activation energy defines the reaction rate constant.

In Section II we discuss the methodology of the calculations and the theory used to calculate the reaction rate constants for a surface reaction. Section III deals with the properties of the reactant and product states on the various dissociation paths; this includes adsorbate geometries, vibrational frequencies, and adsorption energies. We also discuss the transition states and the energy barriers for dissociation and recombination and present a normal mode analysis for the stationary points on the reaction paths and the calculated pre-exponential factors. Our conclusions are summarized in Section IV.

4.3 Methodology and Theoretical Background

4.3.1 Computational Details

The computations reported in this work were performed using the density functional program DMol, which is an implementation of the Kohn–Sham equations [38, 39]. We used numerical basis sets of double- ζ quality and polarization functions for Cu. The Von Barth–Hedin parameterization [40] of the results of Ceperley and Alder’s homogeneous electron gas calculations [41] was used to describe the exchange–correlation energy. Becke–Perdew nonlocal gradient corrections [42, 43] were applied self consistently to the optimized geometries of the stationary points on the reaction paths. To improve the convergence of the self consistent cycling for some systems, we allowed charge smearing for orbitals within 0.005 Ha of the Fermi level.

The energetics and dynamics of the dissociation of nitric oxide and carbon monoxide were investigated on clusters varying in size from 8 to 31 atoms that were clipped from the extended surface with a lattice constant of 3.61 Å, as to model the Cu(111) and Cu(100) surfaces. These cluster models give a reasonable geometrical representation of an extended surface since these surfaces are known to reconstruct only to a small extent [44, 45]. The sizes of some of the clusters are such that computed adsorption energies are still sensitive to electronic edge effects. The larger clusters were used to investigate the importance of these effects.

The reaction paths that we studied (Figure 4.1) were similar to the lowest energy paths for CO dissociation on Rh from a previous publication in our

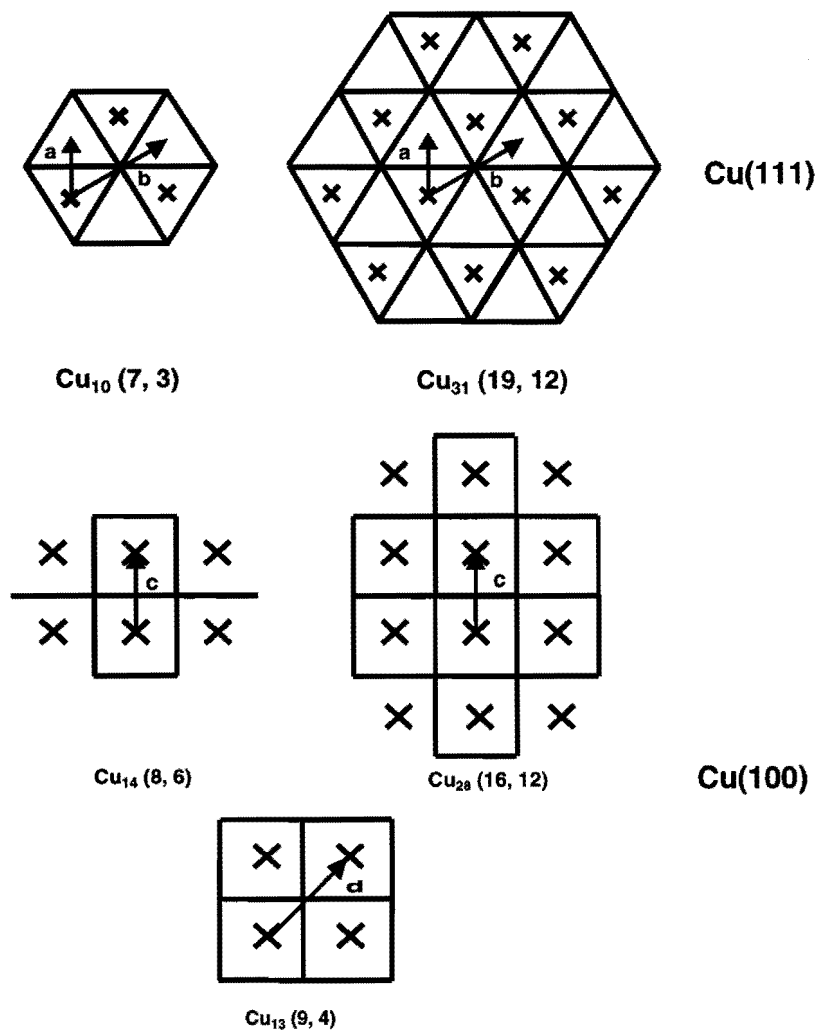


Figure 4.1. Pathways for CO and NO dissociation on cluster models of Cu(111) and Cu(100) surfaces. Drawn lines connect Cu atoms in the first layer. Crosses depict Cu atoms in the second layer. The pathways for dissociation are indicated by arrows which connect the site where the molecule is adsorbed in the reactant state and the site where the oxygen atom is positioned after dissociation. The molecule tilts in the direction of the arrow.

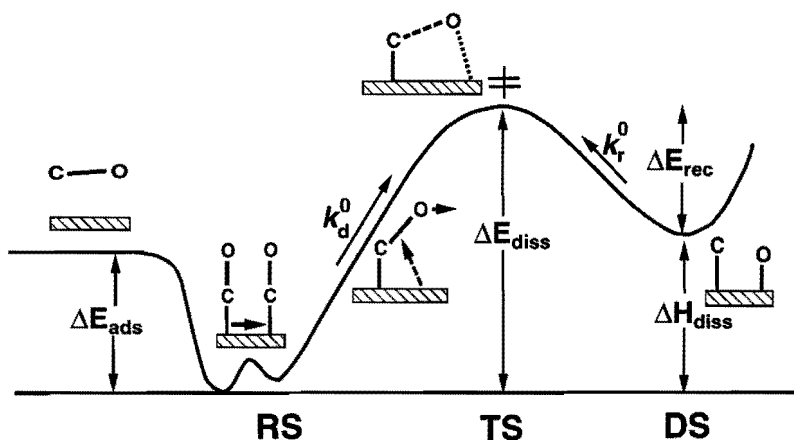


Figure 4.2. Schematic energy profile for the surface dissociation. The stationary points on the reaction path are the reactant state (RS), the product or dissociated state (DS) and the transition state (TS). The diffusion step is necessary for the adsorbate to migrate to a preferred site for dissociation (see text). The metal surface activates the intermolecular bond and facilitates the bond breaking. Energetic parameters of interest are the adsorption energy E_{ads} and the barriers for dissociation (ΔE_{diss}) and recombination (ΔE_{rec}). The kinetics are characterized by the pre-exponential factors for dissociation k_{d}^0 and recombination k_{r}^0 .

group [30]. For each Cu surface cluster, we studied two essentially different pathways, one in which the diatomic is bending over a bridge of two metal atoms (a, c), the other where it bends over a top site of the metal surface (b, d). We used 10- and 31-atom clusters to model the Cu(111) surface and 8-, 13-, 14-, and 28-atom clusters to model the Cu(100) surface. The 31- and 28-atom clusters consist of all first nearest-neighbors of the metal atoms coordinating to the dissociating diatomic. As is shown in Figure 4.2, we will refer to the initial state where the diatomic is molecularly adsorbed as the *reactant state* (RS). The final state with the atoms isolated on the surface will be referred to as the *product state* or *dissociated state* (DS). The saddle point connecting the reactant and product valley is the *transition state* (TS). All reaction paths lie in the C_s symmetry plane of the cluster.

The 3- and 4-fold hollow locations, which are the reactant state geometries, are known to be less stable than the top sites for both CO and NO.

So the molecule needs to move to a hollow site to be in a preferred position for dissociation. Since the difference in energy between the top and 3- or 4-fold hollow sites is small [13], the top-hollow site interchange will not be rate limiting.

The approximate location of the transition state was obtained by taking steps along the reaction path and optimizing the height of the oxygen atom while keeping the carbon atom fixed at the height of adsorbed C. This results in a good estimate for the location of the transition state that can then be used for further geometry refinement. We used a “normal mode following” algorithm developed and implemented by Baker [46] to optimize all the degrees of freedom for the adsorbing species in the plane of symmetry. Typically, 8–10 iterations were needed to locate the transition state. Speed up of this procedure was achieved by sharing the Hessian matrices between cluster-adsorbate systems of varying sizes. All calculations were performed on SGI Indigo 2 workstations and took between 1 h for the smaller clusters and up to 48 h for the largest systems to complete.

4.3.2 Transition State Theory

A diatomic molecule adsorbed on a surface will usually require a vacant nearest-neighbor site to dissociate. For instance, for NO dissociation,



where an asterisk denotes an adsorbed species or a vacant site. Moving on the reaction path from the reactant state to the dissociated state, the molecule will traverse through a transition state. We will use classical transition state theory [47] to compute rate constants from the local properties of these stationary points on the potential energy surface. For the surface dissociation and recombination, the rate constants k_{dis} and k_{rec} at temperature T are given by [47, 48]

$$k_{dis} = \frac{k_B T}{h} \frac{Q'^{TS}}{Q'^{RS}} e^{-\frac{E_0}{k_B T}} \quad (4.2)$$

and

$$k_{rec} = \frac{k_B T}{h} \frac{Q'^{TS}}{Q'^{DS}} e^{-\frac{E_0}{k_B T}} \quad (4.3)$$

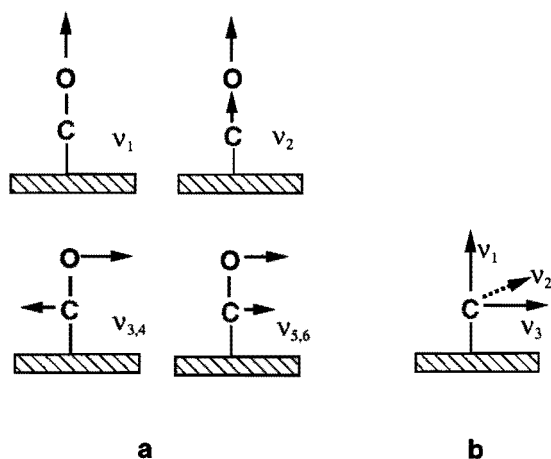


Figure 4.3. Normal modes for a diatomic (a) and monoatomic (b) surface adsorbate. Surface atoms are fixed and have no vibrational freedom.

with

$$Q' = Q \left(\prod_i e^{+\frac{1}{2} \frac{h\nu_i}{k_B T}} \right). \quad (4.4)$$

where k_B is Boltzmann's constant, h is Planck's constant, and E_0 is the difference in energy between the activated complex and the reactants, not corrected for the zero-point energy vibrations. Q'^{RS} , Q'^{TS} and Q'^{DS} are the partition functions at the reactant state, the transition state, and the dissociated state, respectively. The partition functions can approximately be factorized into translational, rotational, and vibrational factors. In the present study, the solid surface is assumed to be rigid; therefore, the partition functions for the surface are equal to unity and do not appear in the rate equation. In addition, if for a surface reaction the adsorbates and the activated complex are localized on the surface, there is no rotational or translational motion but there are only vibrational modes. For the vibrational partition function Q_{vib} , we have used the decomposition in normal modes ν_i using the harmonic approximation yielding

$$Q_{\text{vib}} = \prod_i^{\text{modes}} \frac{1}{1 - e^{-\frac{h\nu_i}{k_B T}}} \quad (4.5)$$

where Q_{vib} is the vibrational partition function for the $3N$ modes of the adsorbate ($3N - 1$ for the transition state) because surface atoms are fixed.

The normal modes for the RS and DS are schematically depicted in Figure 4.3. For the reactant state, a normal mode analysis yields a high frequency CO/NO stretch (ν_1), a Me-CO/NO stretch (ν_2), two degenerated hindered rotations (ν_3, ν_4), and two degenerated hindered translations (ν_5, ν_6). The degeneracy is a consequence of the C_{3v} and C_{4v} point groups of the adsorption sites, but when asymmetric clusters are used, the degeneracy will be lifted. The CO and NO stretch frequencies are usually 100–300 cm^{-1} below the equilibrium gas-phase stretch frequencies (2170 cm^{-1} for CO and 1820 cm^{-1} for NO [49]) depending on the adsorption geometry. The other modes are all expected to be below 800 cm^{-1} . Inspecting the expression for the vibrational partition functions tells us that only modes lower than 200 cm^{-1} will result in a partition function substantially larger than unity. Hindered translations typically have a very low frequency, sometimes below 100 cm^{-1} , and have the highest weight in the calculation of the partition functions. Alternatively, the zero-point energies contribution to the activation energy will mainly come from the high-frequency modes. The dissociated state is characterized by six frequencies that are roughly vibrations in x , y , and z for C/N and O, with possible coupling between these modes. For the transition state, we expect one imaginary frequency corresponding to the reaction coordinate and five real modes of rather complex nature.

The vibrational modes for the adsorbate were calculated harmonically by diagonalizing the second derivative matrix. Second derivatives were computed by taking finite differences of analytical first derivatives. The gradients were calculated for the equilibrium geometry and for the geometries with atoms displaced along the six degrees of freedom. The displacements were typically of the order of 0.01 bohr, but in cases of very flat energy wells, displacements up to 0.03 bohr were used. The reaction rates were calculated at temperatures in the range 300–800 K and fit to an Arrhenius equation to obtain values for the pre-exponential factor and the experimentally measurable activation energy.

4.4 Results and Discussion

The results are discussed in terms of (a) the energetic and geometric properties of CO adsorption as a function of cluster size, (b) the properties of the reactant and product states for CO and NO dissociation (c), the transition

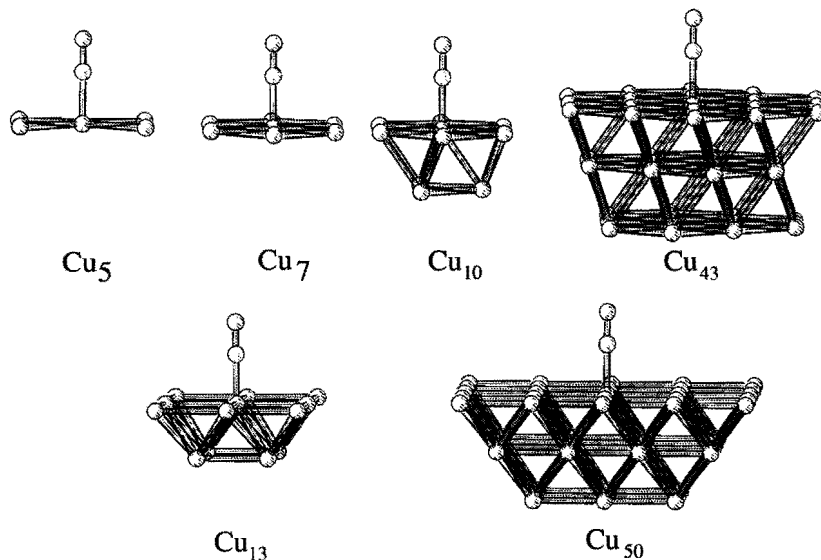


Figure 4.4. Clusters used to study size dependence of adsorption properties. The Cu₅, Cu₇, Cu₁₀, and Cu₄₃ clusters represent a Cu(111) surface, and the Cu₁₃ and Cu₅₀ clusters represent Cu(100). CO is in all cases end-on adsorbed in a top site, with the C-atom coordinating to the surface.

states and the resulting barriers for CO and NO dissociation and recombination, and (d) the normal modes for the adsorbates and pre-exponential factors for the reactions. Subsequent energy analyses are based primarily on the energies that include Becke and Perdew nonlocal corrections. A comparison with the local results will be made.

4.4.1 Cluster Size Dependence: CO Top Adsorption

To estimate the dependence of the energetics, the geometries, and the vibrational frequencies on cluster size, we studied in more detail the molecular adsorption of CO in a top site on clusters representing Cu(111) and Cu(100)

Table 4.1. Energetic (in kcal/mol), structural (in Å) and vibrational (in cm^{-1}) properties for CO adsorbed atop on clusters modeling Cu(111) and Cu(100) surfaces. The nonlocal energies are calculated for LDA optimized geometries. The structural and vibrational numbers were calculated at the local level. Clusters are shown in Figure 4.4.

Cluster	Surface	$E_{\text{ads}}^{\text{LDA}}$	$E_{\text{ads}}^{\text{NLDA}}$	h^a	$d_{\text{C-O}}$	$\nu_{\text{C-O}}$	$\nu_{\text{Cu-C}}$
Cu ₅	(111)	-26.0	-9.1	1.849	1.160	2028	388
Cu ₇		-24.4	-6.9	1.874	1.157	2029	318
Cu ₁₀		-19.5	-1.4	1.853	1.155	2044	336
Cu ₄₃		-21.6	-4.3	1.908	1.162	1993	339
exptl		12.0 ¹³		1.90 ¹³	1.15 ¹³	2079 ¹³	-
Cu ₁₃	(100)	-25.8	-6.7	1.795	1.153	2077	374
Cu ₅₀		-34.4	-15.6	1.805	1.159	2007	398
exptl		-16.7 ¹²		1.90 ⁶¹	1.16 ⁶¹	2064 ¹²	340 ⁶²

^a h is the distance between the carbon atom and the top plane of the Cu atoms

surfaces. Characteristics of CO adsorption on Cu_{*n*} clusters ($n = 5, 7, 10,$ and 43) modeling the Cu(111) and ($n = 13, 50$) modeling the Cu(100) surface (shown in Figure 4.4) are summarized in Table 4.1 and compared with experimental data. For these clusters, we could take advantage of either C_{2v}, C_{3v} and C_{4v} pointgroup symmetry in the calculations. The properties that have been studied for atop adsorption are the equilibrium height of CO above the surface (h) the CO internuclear distance ($d_{\text{C-O}}$), the CO stretch frequency ($\nu_{\text{C-O}}$) and the frequency of the CO vibration against the surface ($\nu_{\text{Cu-C}}$). The molecular adsorption energies are calculated by subtracting the binding energy for the bare cluster and the binding energy for the free molecule from the binding energy of the combined system:

$$E_{\text{ads}} = E_{\text{b}}(\text{Cu}_n\text{CO}) - E_{\text{b}}(\text{Cu}_n) - E_{\text{b}}(\text{CO}). \quad (4.6)$$

For NO, we will later use an analogous expression. We used calculated local (and nonlocal) dissociation energies (in kcal/mol) of -288.0 (-266.5) for gas-phase CO and -185.0 (-162.3) for gas-phase NO.

The calculated values for the adsorption height, the C-O bond length and the vibrational frequencies are within reasonable limits of the experimental

values and in agreement with the calculations of Post and Baerends [23]. The change in C–O equilibrium distance and in C–O vibrational frequency upon adsorption, corresponding to an elongation and weakening of the bond, shows fairly rapid convergence with increasing cluster size. These properties can therefore be called “localized”, since they appear to be converged even without the central metal atom being fully coordinated. The adsorption energies, on the other hand, are not well converged. In fact, on Cu(111), the absolute value of the adsorption energy decreases until the first nearest-neighbor shell of the metal atom is completed due to large energetic changes in the clusters themselves upon adsorption [50]. Adding second nearest neighbors (from Cu₁₀ to Cu₄₃) affects the binding energy only slightly. This behavior is consistent with Shustorovich’s bond order conservation principle [31], where each atom is thought to have a certain amount of “bonding power” shared between all of its neighbors. When the first neighbor shell is incomplete, there will be a greater availability of electrons for bond formation to adsorbed species than in the bulk surface. Hence, the adsorbates are usually overbound when the atom(s) coordinating to the adsorbate have unsaturated valencies. To obtain accurate adsorption energies one should at least satisfy the geometrical requirement to have a complete first nearest neighbor shell. As we will show later on, this requirement is less stringent for calculating relative energies, in particular reaction barriers and energies. The errors made in the reactant, product, and transition states will approximately cancel, resulting in reasonably accurate values for reaction energetics and barriers.

The local adsorption energies for Cu(111) appear to be smaller than the experimental number, given that LDA typically overestimates bond energies. The nonlocal corrections essentially overcorrect these numbers, and the problem of how to achieve high accuracy on chemisorptive bond strengths remains. For the Cu(100) surface, we see a large increase in the adsorption energy when adding the second shell of the metal atoms. This indicates that the Cu₁₃ cluster is still too small to represent the Cu(100) top adsorption site, which was also concluded by Bauschlicher [51]. For Cu(100), the Cu₅₀ cluster gives a nonlocal value of –15.6 kcal/mol which is in good agreement with experiment.

As we present the properties for hollow site adsorption in the next paragraph, we see a preference for hollow over top adsorption, which contradicts experiment [13]. This problem is still present, although less severe, after applying nonlocal corrections. Cluster size effects or coverage dependence may

Table 4.2. Energetic (in kcal/mol) and structural (in Å) properties for the reactant states for CO and NO dissociation.

adsorbate	path	cluster	surface	$E_{\text{ads}}^{\text{LDA}}$	$E_{\text{ads}}^{\text{NLDA}}$	h^a	$d_{\text{C-O}}$
CO	a, b	Cu ₁₀	(111)	-24.8	0.3	1.34	1.19
		Cu ₃₁		-37.7	-11.5	1.33	1.19
	c	Cu ₈	(100)	-39.8	-13.9	1.15	1.20
		Cu ₁₄		-35.6	-9.1	1.11	1.21
		Cu ₂₈		-31.9	-4.6	1.09	1.21
	d	Cu ₁₃		-36.4	-9.0	1.06	1.21
adsorbate	path	cluster	surface	$E_{\text{ads}}^{\text{LDA}}$	$E_{\text{ads}}^{\text{NLDA}}$	h^a	$d_{\text{N-O}}$
NO	a, b	Cu ₁₀	(111)	-44.5	-18.0	1.28	1.23
		Cu ₃₁		-48.4	-22.1	1.30	1.22
	c	Cu ₈	(100)	-52.5	-24.6	1.03	1.24
		Cu ₁₄		-51.9	-26.2	1.13	1.24
		Cu ₂₈		-45.6	-16.9	0.98	1.26
	d	Cu ₁₃		-47.2	-19.2	1.02	1.25

^a h is the distance between either the carbon or the nitrogen atom and the top plane of the Cu atoms

therefore still be of importance. Very promising results were reported using slab calculations for CO monolayer adsorption on Cu(100) [24, 52]. However, this matter is beyond the scope of this study since our prime interest is the dissociation reaction rather than chemisorption.

4.4.2 Reactant and Product States for the Surface Dissociation

On the proposed reaction paths as shown in Figure 4.1, we studied the adsorption properties for the reactant and product states in order to calculate the energetics for the dissociation reaction. The adsorption properties for the reactant states on the various reaction paths, i.e., NO and CO adsorbed in

Table 4.3. Energetic (in kcal/mol) and structural (in Å) properties for the dissociated states for CO and NO dissociation. Indicated are the coordinates for which the adsorbing atoms are optimized (z or xz). $E_{\text{ads}}^{\text{LDA}}$ and $E_{\text{ads}}^{\text{NLDA}}$ are the local and nonlocal total adsorption energy for the coadsorbed atoms. The energy values in brackets are the energy differences between the z and xz optimized geometries. Nonlocal energies were only calculated for the geometries that were used to evaluate the energy barriers (see text).

adsorb.	path	cluster	opt. coord.	$E_{\text{ads}}^{\text{LDA}}$	$E_{\text{ads}}^{\text{NLDA}}$	h_{C}^a	h_{O}^a	$d_{\text{C-O}}^b$
C + O	a	Cu ₁₀	xz	No minimum				
		Cu ₁₀	z	+41.2	+76.5	1.10	1.16	2.95
	b	Cu ₃₁	z	+37.6	–	1.15	1.15	2.95
			xz	+34.5 (–3.1)	+73.6	1.14	1.14	3.05
		Cu ₈	z	–4.9	+44.6	0.07	0.75	2.66
	c	Cu ₁₄	z	+13.5	+58.7	0.15	0.88	2.66
		Cu ₂₈	z	+11.7	–	0.15	0.84	2.65
			xz	+3.6 (–8.1)	+49.0	0.28	0.98	3.03
	d	Cu ₁₃	z	–18.4	–	0.17	0.74	3.66
			xz	–19.4 (–1.0)	+29.9	0.20	0.74	3.75
adsorb.	path	cluster	opt.	$E_{\text{ads}}^{\text{LDA}}$	$E_{\text{ads}}^{\text{NLDA}}$	h_{C}^a	h_{O}^a	$d_{\text{C-O}}^a$
N + O	a	Cu ₁₀	xz	No minimum				
		Cu ₁₀	z	–34.9	+0.4	1.08	1.16	2.95
	b	Cu ₃₁	z	–37.4	–	1.10	1.15	2.95
			xz	–38.5 (–1.1)	–3.0	1.11	1.15	3.10
		Cu ₈	z	–53.2	–3.8	0.10	0.80	2.66
	c	Cu ₁₄	z	–45.4	–3.3	0.38	0.63	2.56
		Cu ₂₈	z	–56.7	–	0.57	0.78	2.56
			xz	–63.2 (–6.5)	–21.7	0.56	0.92	2.92
	d	Cu ₁₃	z	–77.0	–	0.45	0.78	3.63
			xz	–79.2 (–1.8)	–35.0	0.50	0.76	3.82

^a h is the distance between the carbon/nitrogen atom and the top plane of the Cu atoms

^b d the distance between the atoms after dissociation

3- and 4-fold hollow sites, are given in Table 4.2. We optimized the height of the adsorbate, while leaving the other coordinates for the adsorbate frozen, in order not to break the local symmetry of the adsorption site. Especially for the smaller clusters, this appeared to be a necessity. Due to the high reactivity of the edge atoms, which is a cluster artifact, the diatomic tends to bend, and in a few cases the adsorbate actually relaxed to a 2-fold edge position. Fixing the diatomic symmetrically in that site and only optimizing perpendicular degrees of freedom will therefore give the most realistic energies in the absence of a local minimum.

Comparing adsorption for CO in the hollow sites with that for atop adsorption (Table 4.1) shows stronger bonding in higher coordination sites for the Cu(111) surface. For instance, compare the CO nonlocal binding energy of -4.3 kcal/mol atop the Cu₄₃ cluster with that of -11.5 kcal/mol for CO adsorption in the hollow site of the Cu₃₁ cluster. However, for Cu(100), the top site is preferred over the hollow site. Adsorption on the top site of Cu₅₀ shows a binding energy of -15.6 kcal/mol, whereas the binding energy for the hollow site on Cu₃₁ is -4.6 kcal/mol. The LDA results show the same trends. However, especially for hollow site adsorption, oscillations in the binding energy resulting from cluster size effects are large, making it difficult to predict the relative stability of the sites. No experimental data on hollow site adsorption for CO and NO are available, but for CO, it is expected to be close to the top adsorption energy. For that reason, the nonlocal adsorption energies for the largest clusters are very reasonable.

The adsorption properties for the dissociated states are reported in Table 4.3. The adsorption energies are calculated with respect to the bare cluster and the diatomic in the gas phase similarly as for the reactant state (Equation 6). These energies are a measure of the relative stability of the different product states. We first optimized the adsorbate coordinates perpendicular to the surface (rows z). We subsequently relaxed the coordinate in the plane of symmetry to account for the repulsion between the fragments (rows xz). For some of the smaller clusters, the adsorbate fragments relaxed to an edge position, again due to the coordinative unsaturation of the edge atoms. The energy well for atomic adsorption is apparently very flat in these cases causing a relaxation of unphysical nature. Therefore, for the clusters with 8, 10, and 14 atoms, we used the energies for the systems that were only optimized in the direction perpendicular to the surface for calculating the reaction energetics

The bending of CO and NO over a bridge on Cu(111) (reaction path *a*) was rejected as a likely reaction path because the dissociated states appeared to be unstable. When relaxing this state, the atomic fragments recombine without barrier because the “isolated” atoms coadsorbed at adjacent 3-fold sites in the DS (across a Cu–Cu bond) are relatively close (1.48 vs 1.15 Å in molecularly adsorbed CO). There is still an attractive interaction between these atoms, which implies that the molecular bond is not broken. This rules out dissociation along this particular path. A similar observation was reported for hydrogen dissociation along an identical pathway on Ni(111) [29].

The binding energies for the reactant and product state allow us to calculate the reaction energy for dissociation, which is defined here as the difference in total binding energies of RS and DS:

$$\Delta H_{\text{diss}} = E_{\text{b}}(\text{DS}) - E_{\text{b}}(\text{RS}). \quad (4.7)$$

These total energies are not listed, but the dissociation energy can alternatively be obtained by combining this expression with the expression for the molecular adsorption energy (Equation 6), yielding

$$\Delta H_{\text{diss}} = E_{\text{ads}}(\text{DS}) - E_{\text{ads}}(\text{RS}). \quad (4.8)$$

These are reported in Table 4.4.

Dissociation of CO is endothermic for all reaction paths. The differences in dissociation energies on the various surfaces can be explained from the geometries of the dissociated states. Both the lateral distance between the fragments and the adsorption site coordination are important. For reaction path *b* ($d_{\text{lat}} = 2.95$ Å) and *d* ($d_{\text{lat}} = 2.65$ Å), the atoms are adsorbed at adjacent sites, sharing one surface metal atom, while on reaction path *c* ($d_{\text{lat}} = 3.66$ Å), they are sharing two metal atoms. On Cu(111), reaction path *b* has an energy for C + O coadsorption of +74 kcal/mol (Cu₃₁), while on Cu(100), reaction paths *c* and *d* have coadsorption energies of +49 kcal/mol (Cu₂₈) and +30 kcal/mol (Cu₁₃), respectively. The first conclusion is that the isolated atoms are bonded stronger in the hollow sites on Cu(100) than in the 3-fold sites on Cu(111), agreeing with the commonly observed tendency for atoms to favor high coordination. Second, since the lateral spacing is significantly larger for the hollow sites on diagonal path *d* than on the bridged path *c*,

Table 4.4. Local (L) and nonlocal (NL) dissociation energies and activation barriers for dissociation and recombination (in kcal/mol) of CO and NO on the various reaction paths.

	path	cluster	surface	ΔH_{diss}		$\Delta E_{\text{diss}}^{\ddagger}$		$\Delta E_{\text{rec}}^{\ddagger}$	
				L	NL	L	NL	L	NL
CO	b	Cu ₁₀	(111)	+66	+76	97	99	31	23
		Cu ₃₁		+72	+85	108	108	36	23
	c	Cu ₈	(100)	+35	+58	79	91	44	32
		Cu ₁₄		+49	+68	76	88	27	20
		Cu ₂₈		+44	+65	74	85	38	31
d	Cu ₁₃		+18	+39	88	93	70	54	
NO	b	Cu ₁₀	(111)	+10	+18	62	62	52	44
		Cu ₃₁		+11	+20	54	54	43	34
	c	Cu ₈	(100)	-1	+21	46	54	47	33
		Cu ₁₄		+7	+23	39	50	32	27
		Cu ₂₈		-11	+3	35	38	46	34
	d	Cu ₁₃		-30	-9	41	44	71	54

there is more repulsion in the dissociated state of bridged reaction pathway, making the pathway more endothermic (+49 vs +30 kcal/mol). This trend is also manifested in the energy that is released when the adsorbate atoms are allowed to relax in lateral direction z in addition to the perpendicular direction x (Table 4.3). This relaxation energy is -8.1 kcal/mol on reaction path c (Cu₂₈) and only -3.1 and -1.0 kcal/mol on reaction path b and d (Cu₃₁ and Cu₁₃). For NO, we find the same trends of stronger atomic adsorption on Cu(100) than on Cu(111) and stronger repulsion when the atomic fragments are adsorbed at smaller distances.

Besides a distance argument, the high relaxation energy for the Cu₂₈ cluster could also be explained in terms of screening of the fragment interactions by a metal atom. This is more important when the fragments are adsorbed on adjacent sites sharing one surface atom, than when they are adsorbed across a Cu-Cu bridge. The stability of the dissociated state is not only important in the overall reaction energetics, but a stable end configuration also lowers the activation barrier [30], as we will show later.

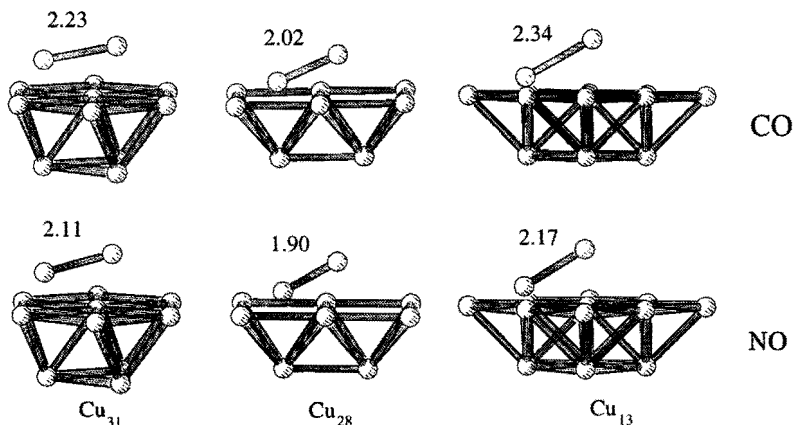


Figure 4.5. Optimized transition state geometries for CO (top) and NO dissociation (bottom) on Cu_{31} (Cu(111)), and Cu_{28} and Cu_{13} (Cu(100)) cluster models, corresponding to reaction paths b, c and d from Figure 4.1. CO and NO distances are indicated in angstroms.

4.4.3 Transition States for Dissociation

Except for reaction path *a*, where we don't expect a transition state, we were able to locate the transition states for all other proposed pathways (Figure 4.5). The activation barriers for the dissociation and recombination reactions are derived from the energies for these transition states

$$\Delta E_{\text{diss}}^{\ddagger} = E_{\text{b}}(\text{TS}) - E_{\text{b}}(\text{RS}) \quad (4.9)$$

and

$$\Delta E_{\text{rec}}^{\ddagger} = E_{\text{b}}(\text{TS}) - E_{\text{b}}(\text{DS}). \quad (4.10)$$

These energies are listed in Table 4.4.

We first consider the cluster size dependence of activation barriers and dissociation energies by comparing identical pathways *c* on clusters of increasing size. The differences between Cu_{10} and Cu_{31} for the barriers and reaction energies for both CO and NO are typically within 15 kcal/mol. For reaction paths *c*, the dissociation barriers for CO are 91, 88, and 85 kcal/mol for the 8-, 14- and 28-atom clusters. The recombination barriers are 32, 20,

and 31 kcal/mol, respectively, and the dissociation energies 58, 68, and 65 kcal/mol. However, the dissociated state for the first two clusters was not fully relaxed, so we should take into account the relaxation energy for the dissociated state on reaction path *c* of approximately 8 kcal/mol. Correcting for this, the barrier for recombination will increase by this amount, giving 40, 28, and 31 kcal/mol and the dissociation energies will be lowered resulting in the sequence 50, 60 and 65 kcal/mol. The differences between the 8- and 28-atom clusters are relatively large, but the values for the 14- and 28-atom clusters are within 5 kcal/mol. This is supposedly the upper limit for the error introduced by finite cluster effects. For NO, the differences in barriers and dissociation energies for the 14- and 28-atom clusters are somewhat larger (up to 14 kcal/mol); hence, the Cu₁₄ clusters might be too small to model the NO dissociation on Cu(100). It is difficult to estimate the error due to the finite cluster size on Cu₃₁. From these results, we conclude that errors due to the finite cluster size can still be considerable. The trends are, therefore, the most meaningful results of this study, rather than the absolute energetics.

The activation barriers for dissociation for CO are significantly higher than those for NO, as expected because of the greater bond strength of CO compared to NO. It is consistent with Shustorovich's bond order conservation (BOC) concept, which relates energy barriers to, among others, the strength of the molecular bond that is being broken. The geometries also indicate a late transition state; the geometries of the transition states are closest to those of the dissociated states. In addition, the dissociation of CO and for NO proceeds much easier on the more open Cu(100) surface than on the close packed Cu(111) surface, in agreement with experiments that show a greater reactivity for more open surfaces toward NO dissociation [17, 18, 53].

Another interesting conclusion can be made by comparing the bridged and diagonal reaction paths on either surface. On Cu(111), it is clearly the diagonal reaction path that is energetically favored for all systems studied, since we could rule out the bridged pathway that is too short for bringing about the dissociation. On Cu(100), however, the bridged pathway is indeed suitable to dissociate the diatomics, and it is, in fact, favored over the diagonal reaction pathway. This indicates that the two metal atoms are quite able to stabilize the transition state and, hence, lower the dissociation barrier. These findings are somewhat in contrast to earlier semiempirical calculations on CO dissociation on Rh. It would be interesting to extend the

DFT calculations to these Rh systems.

Examining the adsorption and dissociation energies for the molecules, it is worth noting that for CO, the dissociation barriers are substantially higher than the adsorption energies (on average 90 vs 10 kcal/mol). Under moderate reaction conditions, CO will upon adsorption not be able to overcome the dissociation barrier. For NO, the dissociation barrier and adsorption energies are 40 and 20 kcal/mol, respectively. Hence, a thermally activated NO molecule could be able to overcome the dissociation barrier. These findings are in agreement with Cu single crystal experiments where NO is observed to adsorb dissociatively while CO adsorbs molecularly [17, 18].

The nonlocal and local results show similar reactivity trends, although the absolute barriers and dissociation energy differ somewhat, as is explained in Figure 4.6. The correction for nonlocal effects appears to be largest for systems that have the strongest surface-adsorbate bonds. The dissociated state is obviously stronger bonded than the reactant state since atom-surface bonds are generally stronger than molecule-surface bonds. The bond between the transition state complex and the surface is likely of intermediate strength. If the correction for the transition state is larger than for the reactant state, it effectively increases the barrier for dissociation. We observed this for the majority of the systems that we studied (see Table 4.4). Since the DS is more corrected than the RS, the dissociation energy becomes more endothermic, and also, the barrier for recombination is lowered. An important conclusion is that it is justified to use the LDA approximation to predict trends in activation barriers. However, nonlocal corrections are essential to predict accurate reaction barriers and energies.

The mechanism for bond activation can be explained by analyzing the orbital interactions. For the Cu_{10} cluster, the fragment orbital density of states shows an increased importance of the contribution of the CO $2\pi^*$ to the adsorbate-surface interaction when the adsorbate tilts (Figure 4.7). For the linearly bound adsorbate, the $2\pi^*$ orbital mixes only to a small extent, and of course only with the lobe centered on the C-atom. Most of the surface-adsorbate interaction is therefore due to the CO 5σ orbital. However, when the adsorbate has tilted, there are many more possibilities for favorable overlap between the $2\pi^*$ orbital and surface orbitals, as is indicated by the increased density in the density of states spectrum.

To illustrate this further, Figure 4.8 shows a bonding orbital that is con-

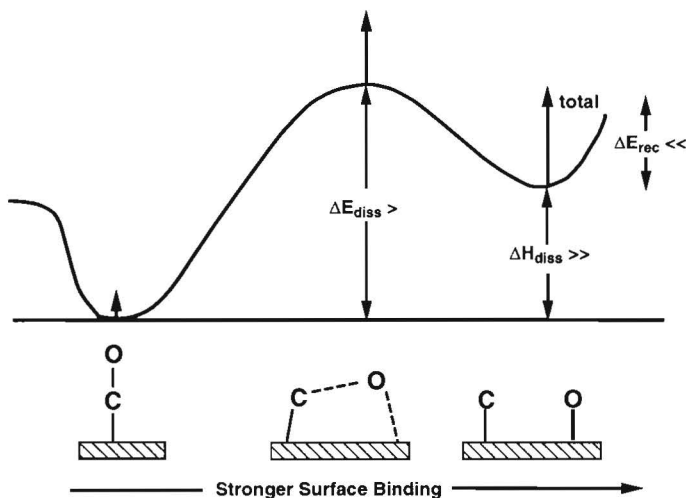


Figure 4.6. Schematic depiction of the influence of nonlocal corrections on reaction barriers and energetics. The dashed arrows show the energy change with respect to the local result. Indicated is the net effect on ΔH_{diss} , $\Delta E_{\text{diss}}^{\ddagger}$, and $\Delta E_{\text{rec}}^{\ddagger}$.

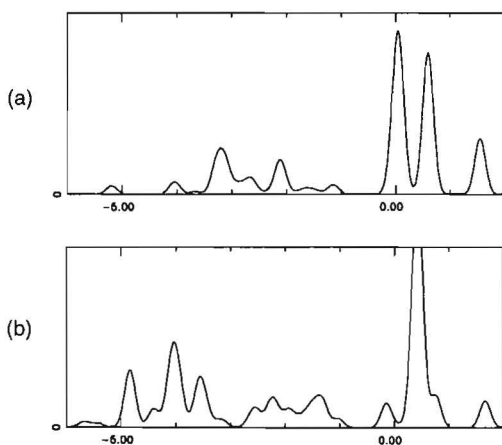


Figure 4.7. Projected CO $2\pi^*$ orbital density of states for (a) the reactant state and (b) the transition state of pathway b on the Cu_{10} cluster modeling the Cu(111) surface. The energies are with respect to the Fermi level (E_F).

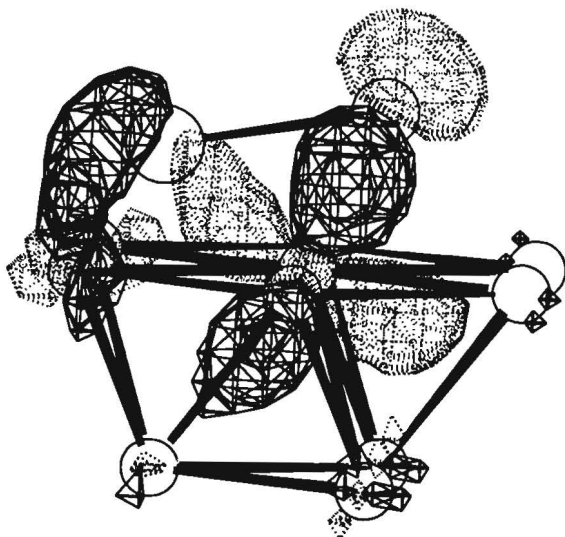


Figure 4.8. Bonding combination of CO $2\pi^*$ -orbital and Cu(111) surface in the transition state for the top pathway (path b in Figure 4.1). The Cu₁₀ framework is shown below, with seven atoms in the first layer and three atoms in the second layer. The carbon atom is located above the surface on the left side, and the oxygen atom is located on the right side. The density plot shows positive and negative values for the molecular wave function.

structed from the molecular $2\pi^*$ and a d orbital on the central Cu atom of the metal surface. This orbital is about 5 eV below the Fermi level (E_F) and stabilizes the transition state. In addition, the $2\pi^*$ -d interaction, although lowering the overall energy, results in a donation of electrons into the $2\pi^*$ orbital of the diatomic, hence destabilizing the molecular bond and facilitating the dissociation. This is the primary effect that explains the metal activated bond breaking and can be expected to be applicable to many similar reactions on metal surfaces.

Table 4.5. Vibrational frequencies (cm^{-1}) of CO at stationary points on the reaction paths. An index i denotes an imaginary frequency. The clusters on which the calculations were performed are indicated. For the RS we have listed the C–O stretch (ν_1), the Cu–CO stretch (ν_2), the degenerated hindered rotations (ν_3, ν_4) and the degenerated hindered translations (ν_5, ν_6) respectively. For the TS the modes are in order of decreasing frequency. ν_6 is the frequency corresponding to the reaction coordinate. For the DS we listed Cu–C stretch (ν_1) and bending modes (ν_2, ν_3), and Cu–O stretch (ν_4) and bending modes (ν_5, ν_6). The partition functions at 300 K corresponding to these modes are shown in the last column.

path	cluster	state	ν_1	ν_2	ν_3	ν_4	ν_5	ν_6	$Q_{\text{vib}, T=300}$
b	Cu ₁₉	RS	1802	315	205	202	57	54	60.6
	Cu ₁₀	TS	565	495	425	353	$i109$	$i388$	2.5
	Cu ₁₉	DS	534	375	375	502	360	360	2.5
c	Cu ₂₁	RS	1564	214	388	388	102	102	14.6
	Cu ₈	TS	570	520	474	353	227	$i294$	2.4
	Cu ₂₁	DS	206	749	749	353	389	389	2.9
d	Cu ₂₁	RS	1564	214	388	388	102	102	14.6
	Cu ₁₃	TS	619	581	568	238	$i135$	$i245$	2.7
	Cu ₂₁	DS	206	749	749	353	389	389	2.9

Table 4.6. Vibrational frequencies (cm^{-1}) and partition functions of NO at stationary points, analogous to Table V.

Path	Cluster	State	ν_1	ν_2	ν_3	ν_4	ν_5	ν_6	$Q_{\text{vib}, T=300}$
b	Cu ₁₉	RS	1481	214	263	236	90	90	26.1
	Cu ₁₀	TS	564	501	497	357	$i88$	$i427$	2.4
	Cu ₁₉	DS	537	425	425	502	360	360	2.3
c	Cu ₂₁	RS	1280	252	470	470	116	116	9.8
	Cu ₈	TS	529	478	380	250	230	$i337$	3.1
	Cu ₂₁	DS	298	528	528	353	389	389	2.7
d	Cu ₂₁	RS	1280	252	470	470	116	116	9.8
	Cu ₁₃	TS	590	540	526	299	$i112$	$i204$	2.5
	Cu ₂₁	DS	298	528	528	353	389	389	2.7

4.4.4 Normal Modes and Pre-exponential Factors

The vibrational frequencies of the adsorbates at the stationary points on the dissociation reaction pathways are reported in Table 4.5 and 4.6. These were used to calculate the partition functions and the transition state theory pre-exponential factors. A frequency calculation is computationally more demanding than a geometry optimization since one can take less advantage of the symmetry of the system when doing finite displacements for all degrees of freedom. We therefore performed the frequency analysis mainly on the smallest clusters representing each reaction path (Cu_{10} , Cu_8 , and Cu_{13}). A problem encountered when analyzing the normal modes for the diatomics and monoatomics on the surface was that the modes parallel to the surface are in some cases difficult to calculate. Unlike the stretching modes perpendicular to the surface, the bending modes appear to be more influenced by changes in the second nearest-neighbor shell of the adsorbate. Another difficulty is that the adsorption site does not have the same symmetry as the cluster. For instance, the reactant states for all reaction paths studied show a local C_{3v} or C_{4v} symmetry, whereas the whole cluster has only C_s symmetry. As a result, the adsorbate in a high-coordination adsorption site tends to move to the edge of the cluster, lowering its energy because of the coordinatively unsaturated edge atoms. This bending is an artifact of the cluster approach, and bending modes calculated for these distorted states cannot have great physical significance. To calculate accurate bending modes, we used larger clusters that have the same symmetry as the adsorption site as shown in Figure 4.9. We used a Cu_{19} cluster to model the 3-fold site on a Cu(111) surface and a Cu_{21} cluster to model the 4-fold site on a Cu(100) surface. The modes shown in Table 4.5 and 4.6 for the reactant and product states result from these calculations. For the DS, we calculated the modes for each atom separately on the same clusters, hence neglecting the coupling between the atomic modes. This coupling is difficult to calculate since an atomic mode parallel to the surface can potentially mix in with modes of adsorbed species on all neighboring sites. Our results will, therefore, best describe the reactivity at low coverages. We did not find any experimental data on CO and NO adsorption in hollow sites, but the shift in stretch frequencies is realistic. The calculated internal CO stretching frequencies are in good agreement with the lowering of CO stretching frequencies observed for higher coordination numbers [54]. The Me-CO stretch is usually less dependent on the adsorption

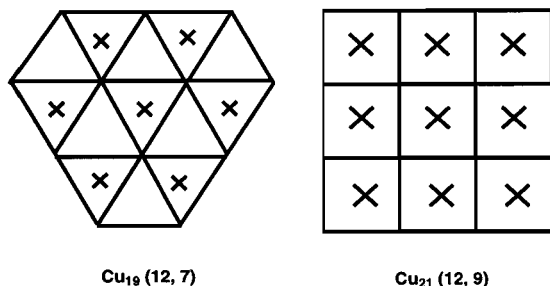


Figure 4.9. Cu_{19} and Cu_{21} clusters used to calculate the normal modes for diatomic and monoatomic adsorbates. Cluster representations as in Figure 4.1.

site, which makes it hard to draw conclusions for the calculated frequencies. A similar trend is found for the internal modes of chemisorbed NO. So *et al.* [15] reported NO stretching frequencies of 1808 and 1520 cm^{-1} on Cu(111) for atop and 2-fold adsorbed NO, respectively. We calculated NO stretch frequencies for 3-fold and 4-fold sites of 1481 and 1280 cm^{-1} , respectively, in line with their experiments.

Experimental data on the parallel vibrational modes for diatomics on copper are unavailable. We therefore compared our calculated values to experimentally available equivalent modes on other metals, which we do not expect to be significantly different. Hindered translations for CO have been observed in the 25–100 cm^{-1} range on Pt(111) by Lahee *et al.* [55] They found a value of 71 cm^{-1} for top adsorbed CO and for a two fold adsorbed CO values of 60 and 144 cm^{-1} (the degeneracy is lifted for the 2-fold site). Our values for NO and CO adsorbed in 4-fold hollow sites on Cu(100) are 100 and 116 cm^{-1} , respectively, in good agreement with their observations. Our values for CO adsorbed in a hollow site are 50 cm^{-1} on Cu(111) and 100 cm^{-1} on Cu(100). For NO, these values are 90 and 116 cm^{-1} , respectively, also in good agreement with their observations. The frequencies for hindered translations are expected to be lower on an open crystal surface than on a close packed surface, since on an open surface it is possible to rotate a molecule through a larger angle before an interaction with the surrounding atoms starts to occur [56]. Our results agree with this. For 3-fold adsorbed CO and NO, we calculated a translational frequency of about half the frequency of the hindered translation for the 4-fold site. Hartree-Fock calculations show somewhat lower frequencies for CO on Cu(100), but this might be due to the lack of electron correlation in these methods [57, 58]. For the hindered rotations, no experimental data are available, but they are expected to lie well above 150 cm^{-1} [55], in agreement with our findings.

For the vibrational frequencies of the atomic adsorbates, we were in some cases able to compare to experimental data. Sexton [59] measured a Cu(100)-O stretch between 290 and 330 cm^{-1} and Mohamed and Kesmodel [60] measured a Cu(100)-N stretch of 324 cm^{-1} . Typically our atom-surface stretch frequencies are within 50 cm^{-1} of the reported values.

For the transition states, the normal mode analysis for the Cu₁₀ and Cu₁₃ clusters yielded one more imaginary frequency besides the one corresponding to the reaction coordinate. This additional imaginary mode corresponds to the motion perpendicular to the symmetry plane, which implies that the calculated transition state is located on a maximum rather than a minimum for this degree of freedom. Further optimization of the transition state by releasing the C_s symmetry constraint moves CO/NO to the edge of the cluster due to the unsaturated edge atoms. This is an artifact due to cluster choice. To solve for this, the clusters have to be expanded to give a pure transition state. However, this requires a frequency calculation on a cluster of about 30 metal atoms, which is not yet computationally feasible. We therefore estimated the asymmetric vibration with the value of the corresponding mode on the Cu₈ cluster (227 cm^{-1} for CO and 230 cm^{-1} for NO).

The computed pre-exponentials are given in Table 4.7. Pre-exponentials lower than 10^{13} relate to a decrease in entropy. This is the case going from reactant to transition state. The theoretically predicted pre-exponential factors correspond to tight transition states, with little rotational and translational motion. This result appears physically quite reasonable and results from the strong interaction of CO and NO in the transition state with the metal surface.

Experimental results for the pre-exponential factors for dissociation show some variability but are generally well below the value of ek_{T}/h [20]. Borg *et al.* [21] report pre-exponentials of 10^{11} s^{-1} for NO on Rh(111) for the elementary surface reaction, in good agreement with our values. Astaldi *et al.* [61] report overall experimental pre-exponentials for CO dissociation on Ni(100) of 5.4×10^9 , and $1.2 \times 10^{16} \text{ s}^{-1}$ for recombination, showing similar changes in entropy going from reactants to products. Fink *et al.* [7] report rather high overall pre-exponentials for NO dissociation on Pt(100) of $2.0 \times 10^{15} \text{ s}^{-1}$. Lesley and Schmidt report a pre-exponential for dissociation of NO on Pt(100) of 10^{13} s^{-1} , in good agreement with our values. Oh and co-workers [4] studied the reduction of NO by CO on single crystal and poly-

Table 4.7. Pre-exponential factors (s^{-1}) for CO and NO dissociation.

	path	cluster	surface	k_{diss}^0	k_{rec}^0
CO	b	Cu ₁₀	(111)	1.5×10^{11}	1.4×10^{13}
	c	Cu ₈	(100)	1.0×10^{12}	1.3×10^{13}
	d	Cu ₁₃	(100)	1.1×10^{12}	1.3×10^{13}
NO	b	Cu ₁₀	(111)	3.4×10^{11}	1.6×10^{13}
	c	Cu ₈	(100)	3.8×10^{12}	2.2×10^{13}
	d	Cu ₁₃	(100)	2.0×10^{12}	1.1×10^{13}

crystalline Rh surfaces and found an activation barrier of about 20 kcal/mol for NO dissociation, and derived an overall rate constant pre-exponential factor for NO dissociation of $6 \times 10^{13} \text{ s}^{-1}$.

4.5 Conclusions

We have performed density functional calculations on the dissociation of NO and CO on clusters simulating single crystal surfaces of copper and calculated the energetics and the pre-exponential factors for the dissociation and recombination reaction. This serves as a model study for the conversion of NO and CO by exhaust catalysts. We have made a comparison of dissociation properties between NO and CO, between different reaction paths, and between the Cu(111) and Cu(100) surfaces.

The surfaces were represented by cluster models varying in size between 10 and 31 atoms. The barriers on the Cu(100) surface are significantly lower than on Cu(111) for both CO and NO. The activation barrier to dissociation appears to be correlated with the spacing between the nearest-neighbor sites. A large spacing results in low repulsion between the fragments after dissociation and a lower activation barrier for dissociation. A similar relation was found by Comrie *et al.* for NO dissociation on (111) surfaces of Pd, Pt, and Ni [62]. The dissociation barriers for NO on Cu(111) and Cu(100) were close to the NO adsorption energy. The barrier for CO dissociation, on the other hand, was at least 70 kcal/mol higher than its adsorption energy. This implies that NO can adsorb dissociatively on Cu(111) and Cu(100) surfaces,

but CO will adsorb molecularly. This agrees with experiments that observe dissociative adsorption of NO at Cu, even at low temperatures, but no dissociation for CO [17]. Applying nonlocal corrections does not alter the trends that we found using a local potential. However, the absolute values for especially the recombination barriers and the reaction enthalpy are affected considerably by introducing nonlocal corrections.

The effect of cluster size on the energetics that we described is still considerable. However, we found reliable trends even with relatively small clusters (10–14 atoms). The use of clusters with more than 20 atoms solved some of the problems that are related with clusters of smaller size, the main problem being the coordinative unsaturation of cluster atoms that are directly neighboring the adsorbate.

We have used transition state theory to calculate the pre-exponentials for dissociation. The normal modes were calculated for the reactant, transition, and product states to obtain the vibrational partition functions. It turned out to be important to increase the cluster size for calculating the normal modes parallel to the surface for the adsorbed species. We have used clusters of 19 and 21 atoms to get reliable values for these modes. The entropy factor appears to be more important for NO than for CO dissociation. The calculated pre-exponentials correspond to a tight transition state for dissociation.

References

- [1] K.C. Taylor, *Catal. Rev.-Sci. Eng.* **35**, 457 (1993).
- [2] B.E. Nieuwenhuys, *Surf. Sci.* **126**, 307 (1983).
- [3] T.W. Root, L.D. Schmidt, and G.B. Fisher, *Surf. Sci.* **134**, 30 (1983).
- [4] S.H. Oh, G.B. Fisher, J.E. Carpenter, and D.W. Goodman, *J. of Cat.* **100**, 360 (1986).
- [5] M. Shelef and G.W. Graham, *Catal. Rev., Sci. Eng.* **36**, 433 (1994).
- [6] B.A. Banse, D.T. Wickham, and B.E. Koel, *J. Catal.* **119**, 238 (1989).
- [7] Th. Fink, J.-P. Dath, M.R. Basset, R. Imbihl, and G. Ertl, *Surf. Sci.* **245**, 96 (1991).
- [8] P. Biloen and W.H.H. Sachtler, *Adv. Catal.* **30**, 165 (1981).
- [9] J.N. Armor, ed., *Appl. Catal. B: Environmental*, 2; Elsevier, Amsterdam (1993).

- [10] J.N. Armor, in *Catal. Today*, Vol. 26 (1995).
- [11] T. Ziegler, *Organometallics* **13**, 2252 (1994).
- [12] M.A. van Daelen, J.M. Newsam, and R.A. van Santen, Molecular Simulations, San Diego, to be published.
- [13] J.C. Tracy, *J. Chem. Phys.* **56**, 2748 (1972).
- [14] P. Hollins and J. Pritchard, *Surf. Sci.* **89**, 486 (1979).
- [15] S.K. So, R. Franchy, and W. Ho, *J. Chem. Phys.* **95**, 1385 (1991).
- [16] J.F. Wendelken, *J. Vac. Sci. Technol.* **20**, 884 (1982).
- [17] A.R. Balkenende, A.L.J. Gijzeman, and J.W. Geus, *Appl. Surf. Sci.* **37**, 189 (1989).
- [18] A.R. Balkenende, H. den Daas, M. Huisman, A.L.J. Gijzeman, and J.W. Geus, *Appl. Surf. Sci.* **47**, 341 (1991).
- [19] G. Brodén, T.N. Rhodin, C. Brucker, R. Benbow, and Z. Hurych, *Surf. Sci.* **59**, 593 (1976).
- [20] C.T. Campbell, Y.K. Sun, and W.H. Weinberg, *Chem. Phys. Lett.* **179**, 53 (1991).
- [21] H.J. Borg, J.F.C.J.M. Reijerse, R.A. van Santen, and J.W. Niemantsverdriet, *J. Chem. Phys.* **101**, 10052 (1994).
- [22] V. Schmatloch, I. Jirka, and N. Kruse, *J. Chem. Phys.* **100**, 8471 (1994).
- [23] D. Post and E.J. Baerends, *J. Chem. Phys.* **78**, 5663 (1983).
- [24] G. te Velde and E.J. Baerends, *Chem. Phys.* **177**, 399 (1993).
- [25] M.A. Nygren and P.E.M. Siegbahn, *J. Phys. Chem.* **96**, 7579 (1992).
- [26] P.E.M. Siegbahn, *Surf. Sci.* **269**, 276 (1992).
- [27] J. Harris and S. Andersson, *Phys. Rev. Lett.* **55**, 1583 (1985).
- [28] P.J. Feibelman, *Phys. Rev. Lett.* **67**, 461 (1991).
- [29] Yang and J. Whitten, *J. Chem. Phys.* **98**, 5039 (1993).
- [30] A. de Koster and R.A. van Santen, *Surf. Sci.* **233**, 366 (1990).
- [31] E. Shustorovich, *Adv. Catal.* **37**, 101 (1990).
- [32] A.D. van Langeveld, A. de Koster, and R.A. van Santen, *Surf. Sci.* **255**, 143 (1990).
- [33] H. Burghgraef, A.P.J. Jansen, and R.A. van Santen, *J. Chem. Phys.* **98**, 8810 (1993).
- [34] H. Burghgraef, A.P.J. Jansen, and R.A. van Santen, *Chem. Phys.* **177**, 407 (1993).
- [35] H. Burghgraef, A.P.J. Jansen, and R.A. van Santen, *J. Chem. Phys.* **101**, 11012 (1994).
- [36] S. Blaskowski, A.P.J. Jansen, M.A.C. Nascimento, and R.A. van Santen,

- J. Phys. Chem.* **98**, 12938 (1994).
- [37] M.A. van Daelen, Y.S. Li, J.M. Newsam, and R.A. van Santen, *Chem. Phys. Lett.* **226**, 100 (1994).
- [38] B. Delley, *J. Chem. Phys.* **92**, 508 (1990).
- [39] E.J. Baerends, D.E. Ellis, and P. Ros, *Chem. Phys.* **2**, 41 (1973).
- [40] U. von Barth and L. Hedin, *J. Phys. C* **5**, 1629 (1972).
- [41] D.M. Ceperley and B.J. Alder, *Phys. Rev. Lett.* **45**, 566 (1980).
- [42] A.D. Becke, *Phys. Rev. A* **38**, 3098 (1988).
- [43] J.P. Perdew, *Phys. Rev. B* **33**, 8822 (1986).
- [44] D.M. Lind, F.B. Dunning, G.K. Walters, and H.L. Davis, *Phys. Rev. B* **35**, 9037 (1987).
- [45] S.A. Lindgren, L. Wolldin, J. Rundgren, and P. Westrin, *Phys. Rev. B* **29**, 576 (1984).
- [46] J. Baker, *J. Comp. Chem.* **7**, 385 (1986).
- [47] K.J. Laidler, *Chemical Kinetics*; Harper and Row, New York 3 edition (1987).
- [48] S. Glasstone, K.J. Laidler, and H. Eyring, *The theory of rate processes*; McGraw-Hill, New York (1941).
- [49] K.P. Huber and G. Herzberg, *Molecular Spectra and Molecular Structure*; Van Nostrand-Reinhold, New York (1979).
- [50] R.A. van Santen, M. Zonneville, and A.P.J. Jansen, *Phil. Trans. R. Soc. Lond. A* **341**, 269 (1992).
- [51] C.W. Bauschlicher, *J. Chem. Phys.* **101**, 3250 (1994).
- [52] P.H.T. Philipsen, G. te Velde, and E.J. Baerends, *Chem. Phys. Lett.* **226**, 583 (1994).
- [53] D.W. Johnson, M.H. Matloob, and M.W. Roberts, *J. Chem. Soc., Faraday Trans. 1* **75**, 2143 (1979).
- [54] N. Sheppard and T.T. Nguyen, *Advances in Infrared and Raman Spectroscopy*; Vol. 5, Heyden, London (1978).
- [55] A.M. Lahee, J.P. Toennies, and Ch. Wöll, *Surf. Sci.* **177**, 371 (1986).
- [56] E. Schweizer, B.N.J. Persson, M. Tüshaus, D.Hoge, and A.M. Bradshaw, *Surf. Sci.* **213**, 49 (1989).
- [57] M. Head-Gordon and J. Tully, *Chem. Phys.* **175**, 37 (1993).
- [58] J. Tully, AT&T Bell Laboratories, personal communication (1995).
- [59] B.A. Sexton, *Surf. Sci.* **88**, 299 (1979).
- [60] M.H. Mohamed and L.L. Kesmodel, *Surf. Sci.* **185**, L467 (1987).
- [61] C. Astaldi, A. Santoni, F. Della Valle, and R. Rosei, *Surf. Sci.* **220**, 322

(1989).

- [62] C.M. Comrie, W.H. Weinberg, and R.M. Lambert, *Surf. Sci.* **57**, 619 (1976).

Chapter 5

Reactivity of Diatomic Molecules on Cu(100)¹

5.1 Abstract

The reactivity of the diatomic molecules O₂, N₂, CO, and NO on Cu(100), has been studied on cluster models representing that surface using first principles density functional calculations. For each molecule the dissociation was studied on top, bridge, and hollow surface sites.

The barriers for dissociation on the energetically most favorable reaction pathways were ordered as O₂ < NO < CO < N₂, with the N₂ and CO barriers high enough to preclude dissociation at moderate operating conditions. The recombination barriers were ordered as CO < NO < N₂ < O₂. These trends were found to be in good agreement with experiment, and they can be explained in terms of the bonding characteristics for each molecule.

In the case of O₂ the dissociation was found to be preceded by a weakly adsorbed state where O₂ is lying parallel to the surface. O₂ dissociation was favored over a hollow surface site. NO, CO, and N₂ showed a slight preference for dissociation over the bridge site. An alternative mechanism was found for NO dissociation whereby the NO goes through a bent adsorbed state in a hollow site and then dissociates over the neighboring bridge of metal atoms. For O₂ and NO we calculated for the lowest energy reaction paths the pre-exponential factors for dissociation and recombination using transition state theory.

¹M.A. van Daelen, M. Neurock, and R.A. van Santen, submitted for publication.

5.2 Introduction

Surface reactivity of small molecules has relevance to many important heterogeneously catalyzed processes. For instance, in the Haber process [1] for synthesizing ammonia from nitrogen and hydrogen gases, it is crucial that the catalyst can break the H_2 and N_2 bonds. Iron metal is very effective in catalyzing H_2 and N_2 bond breaking. The Fisher-Tropsch process is another example, where hydrocarbons are built from synthesis gas that consists of carbon monoxide and hydrogen [2]. The catalyst for this reaction has to activate the CO and H_2 bonds, but at the same time leave other bonds like C=C bonds intact to prevent side reactions.

An example directly related to the present study is the NO decomposition reaction. In the ideal process under non-lean conditions, nitric oxide (NO) is reduced and at the same time carbon monoxide (CO) is oxidized to carbon-dioxide (CO_2). The NO molecule has to dissociate, while it is crucial that the CO bond is left intact. Dissociation of CO will almost certainly disrupt the decomposition reaction since it causes carbon atoms to deposit on the surface causing coking of the catalyst, or alternatively, leading to unwanted products like hydrocarbons. In addition, it is important that other dissociation products like atomic nitrogen are able to react to favorable products, for instance nitrogen gas, that can then desorb from the surface. These are important design criteria that have to be addressed when selecting an appropriate catalyst for this reaction.

These basic reactions have therefore attracted considerable interest in the area of experimental surface science and theoretical modeling. In particular a computationally study is well suited to answer questions as detailed as the ones outlined above. One is able to work with very well defined model systems that allows studying trends in reactivity, without typical experimental artifacts as impurities of the catalyst, side reactions, diffusion limitations, and reaction conditions that are difficult to control. Computational modeling serves very much an analogous role to surface science experimentation in that it foremost increases our fundamental understanding of a complex catalytic system.

In Chapter 4 of this thesis we investigated the reactivity of CO and NO on copper surfaces [3]. We found very clear trends in the surface reactivity between these two molecules. CO was found to dissociate with barriers in excess of 70 kcal/mol while NO dissociation involved barriers that were much

smaller (30 kcal/mol). It was concluded that at moderate operating conditions (such as exist in an automotive exhaust catalyst) CO dissociation is not likely to occur while NO dissociation is a relatively fast reaction. It was also found that the Cu(100) surface shows higher dissociation reactivity than the Cu(111) surface, and that the energetically most favorable reaction path on Cu(100) was the one where the diatomic is bending over an ensemble of two metal surface atoms instead of bending over the top of a metal atom as has been found for the (111) surface [4]. Recombination barriers were predicted to be approximately the same for both molecules.

Experimental data on reactivity of copper-adsorbate systems as described above are of rather qualitative nature. Balkenende *et al.* [5, 6] found NO dissociative adsorption to be weakly activated and did not observe dissociation of CO. Additionally, they found the more open (100) surface to have a higher reactivity than the more closely packed (111) surface.

In its ground state, molecular nitrogen (N_2) will not react with copper surfaces [7]. Molecularly adsorbed nitrogen has not been observed on this surface and dissociative adsorption is a highly activated process. Atomic nitrogen on the other hand interacts strongly with copper, chemisorbing in high coordination sites. It can be formed from electronically excited nitrogen molecules [8], or from dissociation of nitric oxide [5, 6]. The strength of this bonding is manifested by a high activation energy for the associative desorption of nitrogen [7]. On Fe nitrogen is known to have a molecularly adsorbed state that acts as a precursor for the dissociation.

Yokoyama [9] studied the adsorption of oxygen on Cu(100) and found a physisorbed molecular state at temperatures below 50 K, a chemisorbed state at temperatures till 100 K, and an atomic adsorption state at temperatures above 100 K. These results indicated that the barrier for oxygen dissociation is very low for this surface. In the case of adsorbed oxygen atoms the interaction with the surface is weaker than for nitrogen. The electronic configuration of N allows for a strong interaction of all p orbitals with the surface. In the case of O, the p_z orbital is fully occupied, resulting in a somewhat less favorable surface interaction than for N_2 , due to increased Pauli repulsion [10].

There are a number of other theoretical studies on the dissociation properties of diatomic molecules on copper surfaces. We discussed CO and NO adsorption on metal surfaces in Chapter 4 [3]. Panas and Siegbahn studied dissociation of oxygen on Ni(100) for three different reaction paths. They

found very stable molecularly adsorbed oxygen and a very similar mechanism for dissociation over three different surface sites [11].

The present study illustrates the use of density functional theory to study the trends in reactivity for dissociation and recombination of N_2 , O_2 , NO , and CO on copper surfaces. These molecules form an interesting series of test cases since they cover a range of very distinct electronic characteristics. CO is a closed shell molecule, with a lone pair 5σ orbital on the carbon atom. This allows it to form a strong bond with a metal surface. The anti-bonding $\text{CO } 2\pi^*$ orbital is empty and needs to be populated to induce dissociation. N_2 is iso-electronic with CO but its lone pair interaction is much weaker. This makes that it bonds only weakly to metal surfaces. NO is an open shell system with an electronic structure similar to CO but with one electron populating the $2\pi^*$ orbital. Its relatively low energy allows NO to form bonds to surfaces in linear or bend geometries. Dissociation of NO is easier than for CO since it takes less charge donation to critically populate the $2\pi^*$ orbital. Lastly, O_2 has two electrons in the $2\pi^*$ orbital. It prefers to bond parallel to a surface, which further facilitates the activation of the bond.

We have used cluster models to represent the $\text{Cu}(100)$ single crystal surface. These models have shown to be suitable to give accurate trends in surface reactivity, provided that they are adequately sized (> 10 atoms) and nonlocal gradient corrections are included. We will analyze three different dissociation sites on the $\text{Cu}(100)$ surface and discuss the possibility of a surface dissociation versus a direct dissociative adsorption on each of these sites.

In Section 5.3 we discuss the methodological details of the density functional calculations. Section 5.4 describes the results for the transition state calculations for our series of diatomics and compares the trends that we find for the dissociation and recombination reactions of these molecules on $\text{Cu}(100)$. We conclude in Section 5.5.

5.3 Methodology and Theoretical Background

The computations reported in this work were performed using the density functional program DMol, which is an implementation of the Kohn–Sham equations [12, 13]. We used numerical basis sets of double- ζ quality and additional polarization functions for Cu. The Von Barth–Hedin parameterization [14] of Ceperley and Alder’s homogeneous electron gas calculations [15] was used to describe the exchange–correlation energy. Becke–Perdew

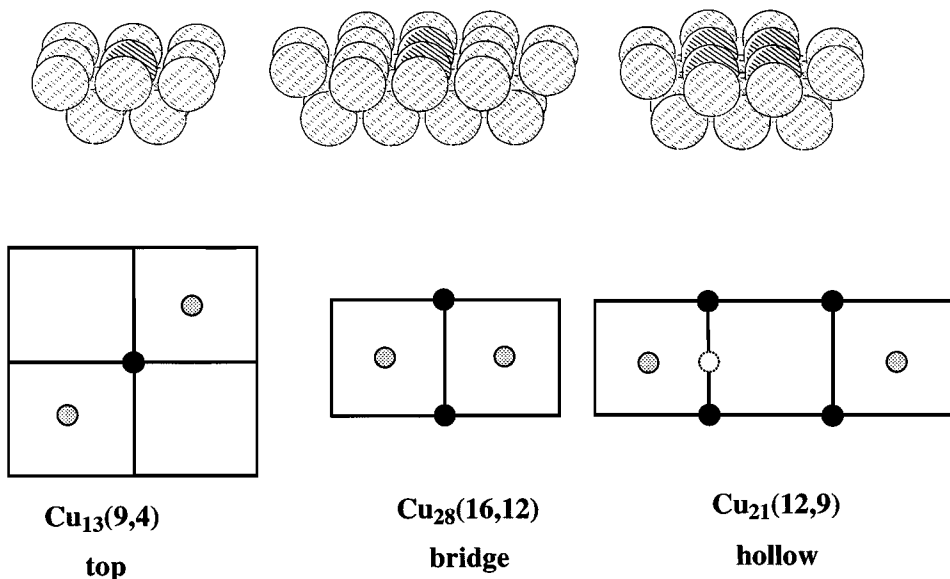


Figure 5.1. Cluster models used to study *top*, *bridge*, and *hollow* dissociation. The dissociation site is indicated by the darker atoms. The schematic depiction on the bottom shows the atoms directly neighboring the site in the first layer. Atoms are connected by lines. The lighter circles indicate the 4-fold hollow sites where the dissociated fragments adsorb after dissociation. For a *top* and *bridge* surface dissociation the molecule starts adsorbed in one of the hollow sites. For the *hollow* mechanism the molecule starts in a 2-fold site, indicated by the open circle. For the direct dissociation the diatomic approaches symmetrically from the gas phase.

nonlocal gradient corrections [16, 17] were applied self consistently to the optimized geometries of the stationary points on the reaction paths. To improve the SCF convergence we allowed charge smearing for orbitals within 0.01 Ha of the Fermi level. In addition, a DIIS procedure was implemented [18, 19], saving on SCF cycles an additional 70 percent.

The energetics and dynamics of the dissociation and recombination of O₂, N₂, CO, and NO were investigated on cluster models that were 13, 21, and 28 atoms in size, representing three different dissociation sites. These clusters were clipped from the extended Cu(100) surface with a lattice constant of 3.61 Å. The models give a reasonable geometrical representation of

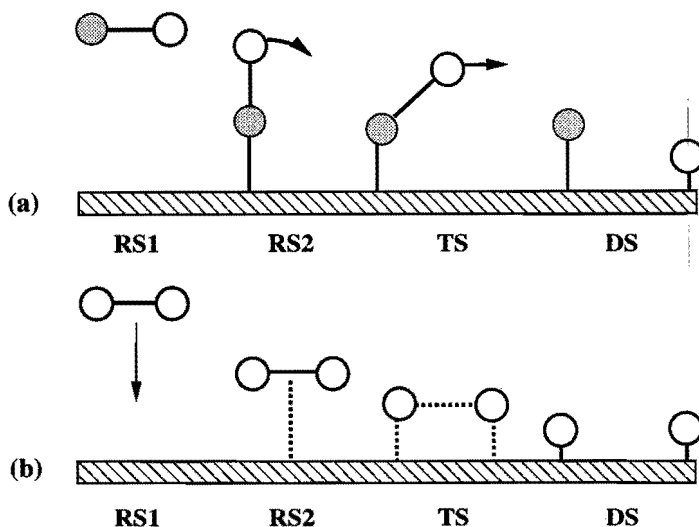


Figure 5.2. (a) Schematic depiction of mechanism for surface dissociation (asymmetric mechanism, C_s symmetry), (b) direct dissociative adsorption (symmetric mechanism, C_{2v} symmetry).

an extended surface since the Cu(100) surface is known to reconstruct only to a small extent [20, 21]. The size of these clusters has been proven to be sufficient to produce energetic trends that are reasonably well converged with cluster size² [3].

The present work focuses on reactivity at three different types of surface sites that differ in that the diatomic dissociates over a top, a bridge, or a 4-fold hollow site. These pathways are hereafter referred to as *top*, *bridge*, and *hollow* dissociation (Figure 5.1). We further distinguished between a surface dissociation mechanism where dissociation is preceded by adsorption of the molecule in approximately an end-on geometry, versus a direct dissociative mechanism where the diatomic dissociates immediately from the gas phase, possibly preceded by an adsorbed state with the molecular bond approximately parallel to the surface (Figure 5.2).

The reactions were investigated by determining the major stationary points on the reaction pathways. Since both the gas phase molecular state and the molecularly adsorbed state can be considered reactant states we refer

²Chapter 4 of this thesis

to these states as reactant states RS1 and RS2, respectively.

For the top and bridge paths the surface dissociation is considered to start with the diatomic adsorbed in a hollow site [22]. For the hollow path the diatomic is more likely to start from a 2-fold site rather than the neighboring hollow site. We will investigate if this is a valid choice for the reactant state. RS2 refers to a predissociative state where the molecule is adsorbed either end-on or parallel to the surface. For all pathways the dissociation products end up in 4-fold hollow positions, known to be the equilibrium positions for chemisorbed atoms on Cu(100) [23]. The final state with the atoms isolated on the surface will be referred to as the *product state* or *dissociated state* (DS). The saddle point connecting the reactant and product valley is the *transition state* (TS). All reaction paths lie in the C_s symmetry plane of the cluster. For the symmetric dissociation of the homonuclear species O_2 and N_2 there is an additional plane of symmetry resulting in a pointgroup C_{2v} for these systems.

It is important to realize that the use of symmetry constraints in an optimization can disguise the true character of the optimized stationary points. A minimum can turn out to be a saddle point, while a transition state becomes a second order saddle point when a symmetry constraint is lifted. However, using these constraints is sometimes inevitable for reasons of computational efficiency and to prevent cluster size artifacts. We will comment on this issue in the following section.

We used a “normal mode following” algorithm developed and implemented by Baker [24] to optimize all the degrees of freedom for the adsorbate atoms of the intermediate structures in the symmetry pointgroup of the system. Typically 6–8 iterations were needed to locate the transition state. Speed up of this procedure was achieved by sharing the Hessian matrices between cluster-adsorbate systems of varying sizes. All calculations were performed on SGI Indigo2 workstations and took between 1 h for the smaller clusters and up to 10 h for the largest systems to complete.

5.4 Results and Discussion

Although we investigate only the stationary points on the reaction pathway we find that this approach in most cases captures the essential chemistry of the dissociation and recombination processes. We will present a few situations though where reaction path following resulted in different stationary

points. Molecular adsorption and desorption processes were also not explicitly considered. In particular desorption processes can be quite slow and influence the overall rate of the process.

The dissociation process sometimes involves surface diffusion of a molecule from the lowest energy adsorption site to a site that is higher in energy but that is better suited to start the dissociation. This process is not explicitly considered in the calculations of the energy profiles. This simplification appears justified since experiments indicate that barriers for molecular surface diffusion for these systems are generally low, typically about 10–20 % of E_{ads} [25].

The minimum energy reaction pathway (MEP) that we calculate in essence represents the reaction mechanism that is followed at zero temperature. As a consequence, the reaction will not follow the MEP precisely at practical operating conditions and it will not traverse directly through the stationary points. Therefore, *ab initio* investigations as presented here rather function as the initial stage in mapping out the PES of a surface reaction. This can then, for instance, serve as input to a dynamical approach based on a parameterization of first principles results [26]. In addition, first principles calculations can provide energetic parameters like adsorption energies, reaction barriers, and pre-exponential factors that can be used in molecular dynamics or Monte Carlo simulations, or alternatively in process simulations as performed by chemical engineers. Another role of first principles work, as presented here, is to indicate possible precursor states, transition states, and intermediates to reactions to establish mechanistic principles.

The dissociation energetics were calculated using both a local and a nonlocal density functional. We will analyze the results mainly using the nonlocal energies, since these are now generally accepted to produce more reliable energetics [27, 28]. When appropriate we will discuss some notable differences between local and nonlocal results.

The adsorption energies are calculated with respect to the gas phase diatomic and bare cluster:

$$E_{\text{ads}} = E_{\text{b}}(\text{Cu}_n\text{AB}) - E_{\text{b}}(\text{Cu}_n) - E_{\text{b}}(\text{AB}). \quad (5.1)$$

We used the calculated diatomic dissociation energies as shown in Table 5.1. The dissociation barriers are defined as the difference between the total energies of the transition state and the molecularly adsorbed state (RS2), or,

molecule	E_b	
	L	NL
CO	-288.0	-266.5
N ₂	-248.2	-225.0
NO	-185.0	-162.3
O ₂	-142.7	-120.1

Table 5.1. Local and nonlocal diatomic binding energies (in kcal/mol) used to calculate the molecular adsorption energy.

as is sometimes convenient, with respect to the gas phase diatomic (RS1). In terms of binding energies we can then write:

$$\Delta E_{\text{diss}}^\ddagger = E_b(\text{TS}) - E_b(\text{RS1}, \text{RS2}) \quad (5.2)$$

When appropriate the tables include both these numbers and are referred to as $\Delta E_{\text{diss},1}$ and $\Delta E_{\text{diss},2}$. Similarly, the barrier for recombination is defined as

$$\Delta E_{\text{rec}}^\ddagger = E_b(\text{TS}) - E_b(\text{DS}). \quad (5.3)$$

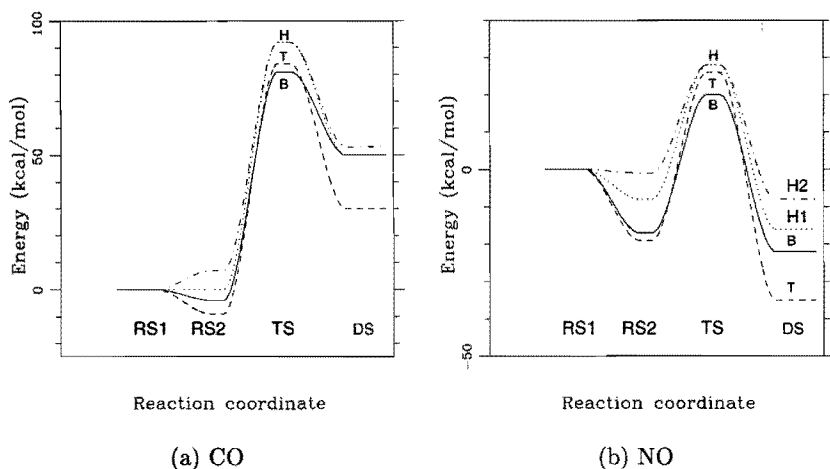
We have plotted the energy profiles for all the dissociation pathways. For convenience we connected the stationary points RS1, RS2, TS, and DS with a smooth curve. This does not necessarily describe the minimum energy reaction pathway, but functions as an aid in visualizing the energetic profiles. To facilitate comparison between various reaction pathways we defined the energy zero as the energy of the gas phase state.

For NO and CO most evidence points to a mechanism where the molecule first adsorbs before it dissociates [22]. For O₂ and N₂ the dissociation usually also involves a molecularly adsorbed state as a precursor, but this is typically a state with the molecule lying parallel to the surface [11]. These two mechanisms are usually referred to as a surface dissociation and a direct dissociative adsorption, respectively. We will first concentrate for each molecule on its common mechanism. For a small number of reaction pathways we will compare the energetics for the two mechanisms.

5.4.1 CO and NO Dissociation

Some of the results for CO and NO dissociation have been discussed in Chapter 4 [3]. For completeness we have summarized them here. Table 5.2 and

Figure 5.3. Energy profiles for top (T, ---), bridge (B, —), and hollow I (H1, ...) and hollow II (H2, · - ·-) pathways for CO and NO dissociation and recombination. H1 and H2 refer to two different types of hollow site dissociation, as is explained in the text.



CO	E_{ads}		$\Delta E_{\text{diss},1}$		$\Delta E_{\text{diss},2}$		ΔE_{rec}	
	L	NL	L	NL	L	NL	L	NL
top	-36	-9	52	84	88	93	70	54
bridge	-32	-5	42	80	74	85	30	20
hollow	-29	0	53	92	82	92	52	42
NO	E_{ads}		$\Delta E_{\text{diss},1}$		$\Delta E_{\text{diss},2}$		ΔE_{rec}	
	L	NL	L	NL	L	NL	L	NL
top	-47	-19	-6	25	41	44	71	54
bridge	-46	-17	-10	21	35	38	46	34
hollow I	-39	-8	-11	27	28	36	53	43
hollow II	-45	-1	-11	27	34	28	46	36

Table 5.2. Energetics for dissociation of NO and CO on Cu(100). Energies are in kcal/mol. Hollow I and II refer to different choices for reactant and dissociated states (see text). Top and bridge dissociation starts with the diatomic adsorbed in a 4-fold hollow site, hollow dissociation starts from a 2-fold site (see Figure 5.1)

Figure 5.3 show the calculated dissociation and recombination barriers. The mechanisms refer to the reactive sites as pictured in Figures 5.1 and 5.2.

The adsorption energies for CO adsorbed in a 4-fold hollow or 2-fold bridge sites, which are the geometries of the reactant states, are calculated to be small: -9 and -5 kcal/mol (4-fold) and 0 kcal/mol (2-fold), respectively. These numbers appear quite reasonable since they are expected to be higher than the top adsorption energy (exptl: -16.5 kcal/mol [25]) which is the lowest energy adsorption site on Cu(100). The local binding energies are predicted too low, which indicates the importance of including nonlocal corrections. The fact that the numbers for 4-fold adsorption differ for the top and bridge model is an artifact of the cluster approach: the adsorption energy on the bridge model (Cu_{28}) is lower than on the top model (Cu_{13}) because the metal atoms binding the adsorbate atom on Cu_{13} are to a lesser degree coordinatively unsaturated.

For all reaction pathways the dissociation of CO is endothermic with respect to both RS1 and RS2 (Figure 5.4(a)). The CO dissociation barriers are high (> 80 kcal/mol), in particular compared to the CO adsorption energy. Upon adsorption a CO molecule will not be able to overcome the barrier for dissociation; it is expected to adsorb molecularly, which is in agreement with experiment [5, 6]. Although dissociation of CO on any copper surface is not likely at moderate conditions, it can be instructive, however, to further analyze the trends for this highly activated process.

Comparing the bridge and the top reaction paths we see that the bridge path has the lowest dissociation barrier, both with respect to RS1 and RS2 (80 and 85 kcal/mol, respectively), but the difference with top and hollow paths is less than 10 kcal/mol. The recombination barrier is, however, significantly lower for the bridge pathway than for any of the other pathways. This stems from the fact that the dissociated state on this path is relatively high in energy because the atomic fragments are at relatively short distance (3.61 Å for the bridge site vs. 2.73 Å for the top site) and still repel each other to some degree.

Summarizing, a bridge dissociation is energetically favored for CO, although the energy difference with the activation barrier on the top path is small. The dissociation can then be followed by surface diffusion of the atomic fragments to reduce the atom-atom repulsion. Barriers for recombination are relatively low; recombination over a bridge site is energetically favored, but in this case atomic fragments first have to diffuse to hollow

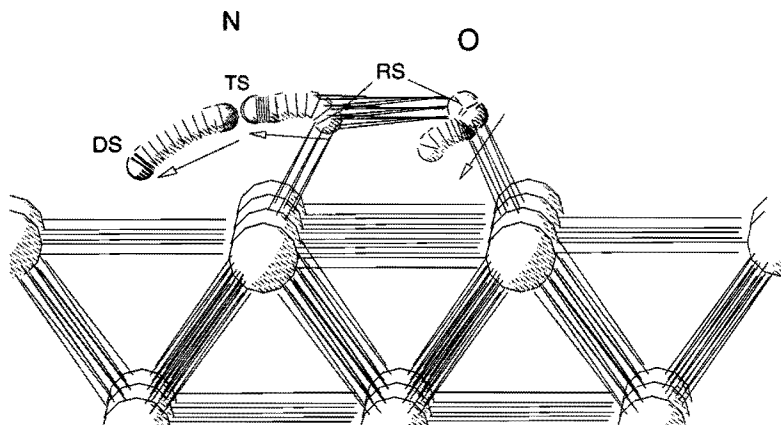


Figure 5.4. Hollow II pathway for NO dissociation (see text). On the left, the nitrogen atom moves from the NO molecule over a bridge site to a neighboring 4-fold hollow site. On the right, the oxygen atom moves closer to the surface and also adsorbs in a 4-fold hollow surface site.

sites, which costs a significant amount of energy. Which reaction pathway is actually followed will certainly depend on the surface coverage. If, at high coverage, there is no ensemble of empty surface sites, a direct dissociative adsorption is not possible. A molecule will be forced to adsorb first, and can dissociate as soon as a neighboring site becomes available. For these cases dissociation barriers with respect to RS2 rather apply, assuming that adsorption is fast. For very low coverages adsorption can be directly followed by dissociation. In this case the barriers with respect to RS1 will be more relevant. The significance of lateral interactions between adsorbates was also observed for intermediates in the oxidation of ammonia [29].

For NO the reactant state for the top and bridge paths is a state where the molecule is adsorbed in a hollow site neighboring either the top or bridge dissociation site. This has been confirmed by following the reaction path from the transition state to the reactant state. For the hollow path it was initially assumed that NO starts the dissociation from the bridge site that neighbors the 4-fold hollow dissociation site. These results are indicated with *hollow I*. However, the transition state that was obtained by doing a full geometry

optimization is shifted with respect to the center of the 4-fold hollow site (Figure 5.4). Following the reaction path from the transition state into the reactant and product valley reveals that the reactant state for NO is in fact a bent species adsorbed in a hollow site, and that the NO bond is activated by the neighboring bridged metal atoms. Such a state has also been observed experimentally [30]. The experimental NO stretch frequency for this state is 776 cm^{-1} , in reasonable agreement with the stretch frequency of 859 cm^{-1} that we calculated.

This finding suggests that activation of the molecular bond is preferred by a close interaction of the bonds with the surface atoms, and that stationary points initially used to calculate energetics for the *hollow I* mechanism are not likely intermediates. The corrected energetics are indicated in Table 5.3 with *hollow II*.

For the dissociation of NO we see a picture that is also clearly different than for CO. With respect to the gas phase reactants the pathways are all slightly exothermic with respect to RS1. The adsorption energies for NO in hollow sites are -17 and -19 kcal/mol, which is about twice as large as the adsorption energies for CO. The dissociation barriers for NO are considerably lower than those for CO. With respect to RS2 the barriers are between 28 and 44 kcal/mol. One would therefore expect that NO when adsorbing on a copper surface will be able to surmount the activation barrier for dissociation, even at moderate operating conditions. This is in agreement with Cu(100) single crystal surface experiments [5, 6] that show that NO adsorbs dissociatively on this surface with a very small energy barrier. For such experiments the observed activation barrier for dissociation is rather taken with respect to the gas phase state, i.e.

$$\Delta E_{\text{act}}^{\text{exp}} = \Delta E_{\text{act}} - \Delta E_{\text{ads}} \quad (5.4)$$

Comparison of our activation energies with experiment in a more quantitative manner is difficult because the error due to the cluster approximation is in some cases still significant.

Analogous to the CO dissociation, for NO the bridge pathway is also slightly favored over the top pathway. Again, the atomic fragments are clearly stabilized if the fragments diffuse to occupy sites that share only one metal atom. A pseudo symmetric mechanism has also been investigated for NO to be compared to the more common asymmetric mechanism. This has been done for adsorption over the bridge site. We located the transition state and

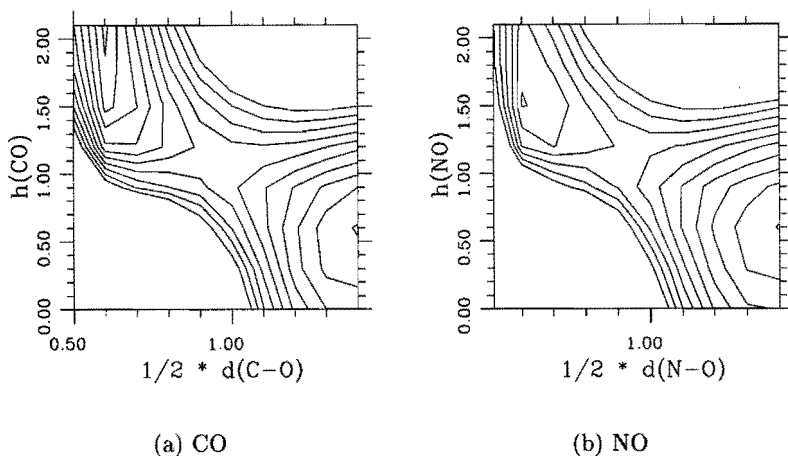


Figure 5.5. Potential energy surfaces for CO and NO approaching a bridge Cu(100) site. Relative energy is plotted as a function of the height of the CO/NO bond with respect to the surface (h) and the distance between C/N and the oxygen atom (d). Neighboring contours differ 10 kcal/mol in energy.

a possible precursor on the bridge site by varying the N–O distance and the distance between the center of the NO bond and the surface. This ensures a pseudo C_{2v} symmetry for the system. These calculations were done using a local functional. The potential energy surfaces are shown in Figure 5.5. For NO there is a weakly bonded state with the molecule adsorbed about 1.5 Å above the surface. This state has an energy of -12 kcal/mol with respect to the gas phase, and is as expected less stable than an end-on adsorbed geometry. The barriers for dissociation with respect to the gas phase can be read from the plots and are 57 and 14 kcal/mol, respectively, for CO and NO. These are both higher than the (local) surface dissociation barriers $\Delta E_{\text{diss},1}$ (from Table 5.2), which were 42 and -10 kcal/mol for CO and NO, respectively. This supports the fact that for CO and NO a surface dissociation is more favorable than a direct dissociative adsorption.

5.4.2 O_2 and N_2 Dissociation

The energetics for N_2 and O_2 dissociation are summarized in Table 5.3 and Figure 5.6. We studied only a symmetric approach for N_2 . The end-on ad-

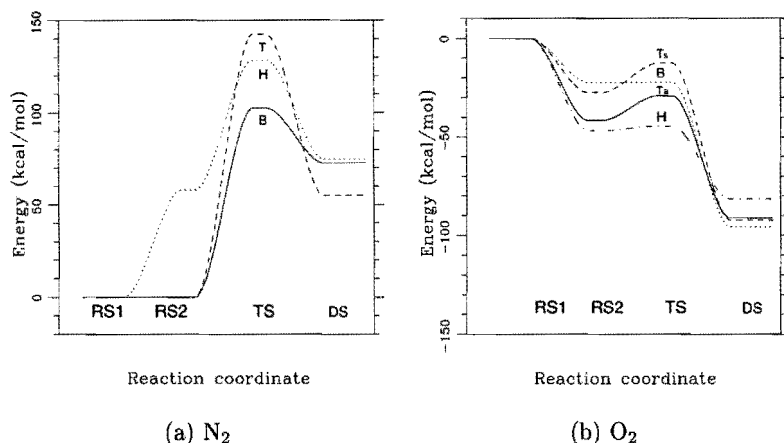


Figure 5.6. Energy profiles at the nonlocal level for dissociation and recombination of N₂ and O₂. The shoulder on the profile for N₂ indicates a metastable precursor for dissociation. Labeling of pathways as in Figure 5.3. T_s and T_a refer to a symmetric and asymmetric mechanism, respectively, as is explained in the text.

sorption energy for N₂ is very unfavorable ($> +70$ kcal/mol). This state was obtained by energy minimizing, in the local density approximation, from the transition state and doing a non-local point calculation at the minimum. We did not investigate the barrier that has to exist between RS1 and RS2 as that was not an objective of this study. This is an unlikely precursor for dissociation and it rules out a surface dissociative mechanism. Figure 5.6(a) shows that N₂ dissociation is strongly endothermic. We found a local minimum for parallel adsorption on the hollow pathway which was +58 kcal/mol non-binding. Note that in Figure 5.6(a) this state does not appear as a local minimum because we did not calculate a barrier for adsorption. The barriers for N₂ dissociation are very high: between 116 and 143 kcal/mol with respect to the gas phase reactants. As for CO, it is not to be expected that N₂ dissociates on the Cu(100) surface at moderate reaction conditions. Analogous to CO and NO, we see that for N₂ the bridge pathway has a lower dissociation barrier than the top pathway. The bridge path also shows the lowest barrier for recombination: 37 kcal/mol. However, this observed barrier for associative adsorption of N₂ is likely higher since the dissociated state for

N ₂ mechanism		E _{ads}		ΔE _{diss,1}		ΔE _{rec}			
		L	NL	L	NL	L	NL		
top	sym	-	-	117	143		119 88		
bridge	sym	-	-	81	116		47 37		
hollow	sym	+3	+58	89	128		67 54		
O ₂ mechanism		E _{ads}		ΔE _{diss,1}		ΔE _{diss,2}		ΔE _{rec}	
		L	NL	L	NL	L	NL	L	NL
top	asym	-50	-30	-61	-35	< 1	< 1	68	57
	sym	-46	-28	-32	-13	15	15	99	80
bridge	sym	-46	-22	-51	-25	0	0	80	71
hollow	sym	-85	-47	-82	-44	3	2	42	37

Table 5.3. Local (L) and nonlocal (NL) energetics for dissociation of N₂ and O₂ on Cu(100). For oxygen energies are listed for both a symmetric and an asymmetric mechanism. Energies are in kcal/mol. For O₂ ΔE_{rec} is defined with respect to the gas phase state since the desorption of O₂ is highly activated (see Figure 5.6(b)).

the bridge path is significantly less stable than the dissociated states for the top and hollow paths. An additional diffusion step would add another 20 kcal/mol to the N₂ recombination barrier (Figure 5.6(a)). On Cu(111) TPD measurements revealed a nitrogen desorption temperature of 620 K with a barrier of 29 kcal/mol [7]. Our calculated barriers on Cu(100) are somewhat larger, but the trend is in line with the NO results: the calculated barrier for NO dissociation is only 20–25 kcal/mol, and is observed to dissociate spontaneously at low temperatures [5, 6].

The existence of different routes for recombination is in line with TPD experiments showing multiple peaks for recombinative N₂ desorption [7]. The authors attributed this to the existence of different adsorption sites such as top, bridge, and hollow sites that have similar stabilities, but are separated by rather high diffusion barriers. Our explanation is different in that we found nitrogen atoms to be preferably adsorbed in hollow sites and differences in stability result from increased repulsion when atoms are adsorbed in neighboring sites.

For O₂ dissociation we made in some cases a distinction between a symmetric and an asymmetric pathway. On all pathways dissociation of O₂ is

strongly exothermic with no significant activation barrier. The reaction energies vary from -82 to -96 kcal/mol. Although none of the mechanisms are activated the most favorable pathway is probably the hollow pathway, because the precursor state is more stable here (-45 kcal/mol) than on any of the other pathways. For the asymmetric top pathway there appeared to be only a very small barrier that separates RS2 and DS. In RS2, oxygen is adsorbed in the hollow site and is tilted towards the central metal atom. The dissociation is very weakly activated and the predissociative state is not very stable with respect to the dissociated state. Figure 5.6(b) shows that this precursor state is significantly lower in energy than the precursor state on the symmetric top pathway (-62 vs. -64 kcal/mol). O_2 dissociation on this site will be favored in an asymmetric approach. On the bridge and hollow pathways we did not calculate energetics for an asymmetric mechanism. The symmetric bridge pathway was also found to have no transition state separating RS2 and DS. This step is not activated and the predissociative state is metastable.

On the hollow pathway there is a transition state with a small barrier with respect to RS2 of 2 kcal/mol. Lifting the C_{2v} symmetry constraint does not change the character of the transition state and a calculation of the normal modes of vibration of the system confirmed that this was actually a true transition state (see Section 5.4.4). As a result we do not expect that an asymmetric approach would be more favorable on this pathway. These findings agree with NEXAFS experiments showing that molecular oxygen on copper is very unstable and can only be detected at low temperatures (100 K) [9]. Because of the strong exothermicity of oxygen dissociation, recombination is highly activated with barriers over 80 kcal/mol.

To investigate further the dissociation mechanism we calculated the bond-lengths and Mulliken populations for the intermediates and transition states for the three reaction paths for the O_2 and N_2 dissociation (Figure 5.4). For O_2 it can be seen that the bond stretch is fairly significant upon adsorption. This goes along with a significant increase in the Mulliken charge population for the oxygen atom (from 0 to -313), indicating that after adsorption the bond is already substantially weakened. For a precursor state that was found on the hollow path for N_2 , this effect is not as strong (1.11 to 1.24 Å). The transition state structure has the atomic fragments at larger distance than

Table 5.4. Structural parameters for N₂ and O₂ dissociation on symmetric pathways. Bond lengths in Å, charges x10³e.

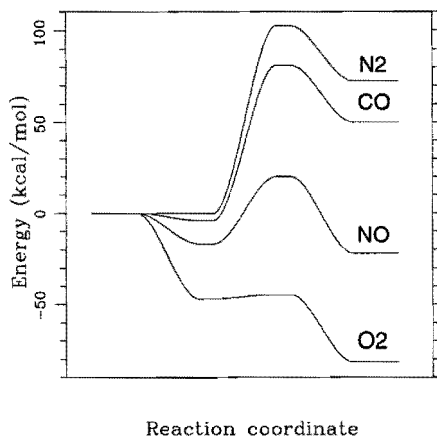
site	bond length				Mulliken charge on N/O			
	RS1	RS2	TS	DS	RS1	RS2	TS	
N ₂	top	1.11	—	2.19	3.74	0	—	-409
	bridge	1.11	—	1.84	2.73	0	—	-440
	hollow	1.11	1.24	3.00	5.28	0	-397	-549
O ₂	top	1.23	1.43	1.79	3.75	0	-313	-436
	bridge	1.23	1.54	—	2.90	0	-369	—
	hollow	1.23	1.55	1.90	5.32	0	-347	-491

for O₂, because of the stronger molecular bond of N₂ compared to O₂. The full d-shell of copper does not allow for a favorable interaction with N₂ which is necessary for the breaking of the bond. Indeed, metals like Fe and Ru with 6 and 7 d-atoms, respectively, show much lower barriers for dissociation of N₂ [1].

5.4.3 Dissociation and Recombination Trends

The dissociation profiles for the four molecules on the energetically most favorable pathways are shown in Figure 5.7. They correlate well with the gas phase dissociation energies (Table 5.1) with the exception of N₂ and CO. CO dissociates easier on a surface although the CO bond is somewhat stronger than the N₂ bond. N₂ dissociation barriers are higher because activation of the 2π* orbital is more difficult (N₂ is more inert), resulting from the larger 5σ-2π* band gap for N₂ than for CO. Although CO and N₂ are iso-electronic, the gas phase bond strength for CO is greater than for N₂. Because of the asymmetry of the CO bond the 5σ lone pair is localized on one of the atoms and is essentially non bonding. For N₂ the 5σ is slightly anti-bonding.

The barrier heights for the dissociation and recombination reactions for each molecule can be applied to a complex catalytic process as the NO decomposition. This will give an indication what reactions are possible on the surface, and what the rate limiting steps will be in the overall catalytic cycle. Nitric oxide that is present in an automotive exhaust stream will be able to dissociate readily on Cu(100). The large barrier for CO dissociation on the other hand will preclude any dissociation, but adsorbed CO can be



	$\Delta E_{\text{diss},1}$	ΔE_{rec}
N ₂	116	54
CO	80	42
NO	21	36
O ₂	-82	82
CO ₂	69	35

Figure 5.7. Energetics for dissociation and recombination on hollow pathways on Cu(100). Energies are in kcal/mol. The CO₂ results [31] are for the dissociation of CO₂ from the gas phase, to form adsorbed CO and O.

oxidized with a barrier of approximately 30 kcal/mol [31]. Any O₂ present will instantly oxidize the surface. This can slow down the reaction since the reverse reaction, the formation of O₂ from oxygen atoms, is very difficult. Nitrogen species that are deposited for NO dissociation can recombine to form N₂ at elevated temperatures, to form N₂ which is inert in this catalytic environment.

5.4.4 Reaction Rates

The qualitative aspects that we discussed are good indications of what happens on a catalyst surface. More accurate calculations seem necessary to obtain hard numbers that can be used to calculate reaction rates, and to address the performance of the catalyst under practical conditions. A first attempt to address this problem for some of these reactions is presented here. Since we have determined the transition states for the dissociation and recombination reactions, we can apply transition state theory to calculate a pre-exponential factor from the vibrational properties of the stationary points on the reaction paths. For a detailed description of this procedure the reader is referred to Chapter 4 of this thesis, or textbooks on this topic [32]. The reactions of most practical interest are the dissociation and recombina-

Table 5.5. Vibrational frequencies (cm^{-1}) of O_2 and NO at stationary points on the *hollow II* reaction paths. An index i denotes an imaginary frequency. The partition functions at 300 K derived from these modes are shown in the last column.

path	state	ν_1	ν_2	ν_3	ν_4	ν_5	ν_6	$Q_{\text{vib},T=300}$
O_2	RS	225	387	425	439	487	568	2.8
	TS	171	401	453	477	511	i 317	2.9
	DS ^b	353	353	389	389	389	389	2.9
NO	RS	238	373	405	483	524	859	1.9
	TS	170	412	479	548	589	i 279	2.6
	DS ^b	289	528	528	353	389	389	2.7

^b from Chapter 4

tion of O_2 and NO since these have barriers that are sufficiently low to let the reaction occur at reasonable temperatures. A vibrational analysis for the adsorbate in reactant, transition, and product states resulted in six frequencies for each stationary point. These are shown in Table 5.5, together with the resulting vibrational partition function. Besides the imaginary frequency associated with the NO reaction coordinate, the frequencies for the five other modes are all above 200 cm^{-1} , indicating a tight transition state with little vibrational freedom.

In contrast to earlier calculations on CO and NO [4] the reactant state shows no high entropy modes such as a hindered translation. The lower entropy of the reactant states results from the strong bonds that the molecules form upon adsorption. O_2 and N_2 show very similar partition functions for RS, TS, and DS and as a result the pre-exponential factors for dissociation and recombination are close to 10^{13} s^{-1} , or $ek_{\text{B}}T/h$, only for NO dissociation these are somewhat lower ($5 \times 10^{12} \text{ s}^{-1}$) because of the higher entropy of the NO reactant state.

Both theoretical and experimental pre-exponentials have significant error bars, what complicates a comparison. Since O_2 dissociation is strongly exothermic, this reaction is expected to be very fast with a sticking coefficient close to unity. The reaction will be rather diffusion limited until it is

slowed down when the surface coverage increases. O_2 is then forced to first adsorb first before it can dissociate. The calculated pre-exponential rather applies to the situation where desorption of coadsorbed atoms is competitive with the O_2 dissociation. The value of 10^{13} s^{-1} is in line with data for O_2 dissociation on Pt(100) (10^{11} s^{-1}) [33].

Addressing rates not only warrants accurate calculations of pre-exponential factors, but also an accurate determination of the activation barrier. The error made in the calculation of the dissociation barrier is realistically at least 10–20 percent. This can influence the rate for the reaction dramatically because of the exponential dependence on the activation energy.

5.5 Conclusions

We have been able to qualitatively predict trends for adsorption of a series of diatomic molecules on copper surfaces. Although the use of clusters to model reactions at infinite surfaces is known to introduce an error in the energetics, we have shown that this type of study is very useful for investigating mechanistic details of particular reactions. We have been able to derive optimal reaction pathways for a set of different diatomics and we have calculated the minimum energy that is needed to convert each of those molecules.

The barriers for dissociation on the energetically most favorable reaction pathways were ordered as $O_2 < NO < CO < N_2$, with the N_2 and CO barriers high enough to preclude dissociation at moderate operating conditions. The recombination barriers were ordered as $CO < NO < N_2 < O_2$. These trends were found to be in good agreement with experiment, and they can be explained in terms of the characteristic electronic structure for each molecule.

Dissociative adsorption versus surface dissociation can be understood by calculating energetic profiles for these processes. For CO and NO it is energetically more favorable to first adsorb on the surface and then to dissociate. CO, NO, and N_2 prefer to dissociate over a bridge of two metal atoms. An interesting mechanism for NO dissociation was found with a relatively low barrier: the NO molecule adsorbs in a tilted geometry in a hollow site, and it then slides over the neighboring bridge site, after which the dissociated fragments end up in neighboring hollow sites. In contrast, oxygen prefers to dissociate over a hollow site, which consists of an ensemble of four metal atoms, directly from the gas phase. It goes through an unstable linearly adsorbed predissociative state.

For two particular reaction pathways we have calculated the pre-exponential factors for dissociation and recombination based on transition state theory. These were all approximately 10^{13} s^{-1} , except for the NO pre-exponential factor for dissociation, which was $5 \times 10^{12} \text{ s}^{-1}$. An interesting follow up of this study would be to use the calculated reaction barriers and pre-exponential factors as input in classical Monte Carlo simulations. Such a study is currently underway in our group [34].

References

- [1] A. Ozakai and K. Aika, *Catalysis: Science and Technology*, Springer, Berlin (1981).
- [2] P. Biloen and W.H.H. Sachtler, *Adv. Catal.* **30**, 165 (1981).
- [3] M.A. van Daelen, Y.S. Li, J.M. Newsam, and R.A. van Santen, *Chem. Phys. Lett.* **226**, 100 (1994).
- [4] M.A. van Daelen, Y.S. Li, J.M. Newsam, and R.A. van Santen, *J. Phys. Chem.* **2279**, 100 (1996).
- [5] A.R. Balkenende, A.L.J. Gijzeman, and J.W. Geus, *Appl. Surf. Sci.* **37**, 189 (1989).
- [6] A.R. Balkenende, H. den Daas, M. Huisman, A.L.J. Gijzeman, and J.W. Geus, *Appl. Surf. Sci.* **47**, 341 (1991).
- [7] A. Berko and F. Solymosi, *Surf. Sci.* **55**, 193 (1992).
- [8] A.P. Baddorf and D.M. Zehner, *Surf. Sci.* **238**, 255 (1990).
- [9] T. Yokoyama, D. Arvanitis, T. Lederer, M. Tischer, L. Tröger, K. Baberschke, and G. Comelli, *Phys. Rev. B* **48**, 15405 (1993).
- [10] T. Lederer, D. Arvanitis, G. Comelli, L. Tröger, and K. Baberschke, *Phys. Rev. B* **48**, 15390 (1993).
- [11] I. Panas, P.E.M. Siegbahn, and U. Wahlgren, *J. Chem. Phys.* **90**, 6791 (1989).
- [12] B. Delley, *J. Chem. Phys.* **92**, 508 (1990).
- [13] E.J. Baerends, D.E. Ellis, and P. Ros, *Chem. Phys.* **2**, 41 (1973).
- [14] U. von Barth and L. Hedin, *J. Phys. C* **5**, 1629 (1972).
- [15] D.M. Ceperley and B.J. Alder, *Phys. Rev. Lett.* **45**, 566 (1980).
- [16] A.D. Becke, *Phys. Rev. A* **38**, 3098 (1988).
- [17] J.P. Perdew, *Phys. Rev. B* **33**, 8822 (1986).
- [18] P. Pulay, *J. Comp. Chem.* **3**, 556 (1982).
- [19] C.M. Kölmel, unpublished results (1995).

- [20] D.M. Lind, F.B. Dunning, G.K. Walters, and H.L. Davis, *Phys. Rev. B* **35**, 9037 (1987).
- [21] S.A. Lindgren, L. Wolldin, J. Rundgren, and P. Westrin, *Phys. Rev. B* **29**, 576 (1984).
- [22] A. de Koster and R.A. van Santen, *Surf. Sci.* **233**, 366 (1990).
- [23] M.H. Mohamed and L.L. Kesmodel, *Surf. Sci.* **185**, L467 (1987).
- [24] J. Baker, *J. Comp. Chem.* **7**, 385 (1986).
- [25] J.C. Tracy, *J. Chem. Phys.* **56**, 2748 (1972).
- [26] M. Head-Gordon and J. Tully, *Chem. Phys.* **175**, 37 (1993).
- [27] P.H.T. Philipsen, G. te Velde, and E.J. Baerends, *Chem. Phys. Lett.* **226**, 583 (1994).
- [28] M. Neurock and R.A. van Santen, *J. Am. Chem. Soc.* **116**, 4427 (1994).
- [29] M. Neurock, R.A. van Santen, W. Biemolt, and A.P.J. Jansen, *J. Am. Chem. Soc.* **116**, 6860 (1994).
- [30] J.F. Wendelken, *Applic. of Surf. Sci.* **11/12**, 172 (1982).
- [31] M.A. van Daelen, unpublished results (1995).
- [32] R.A. van Santen and J.W. Niemantsverdriet, *Chemical Kinetics and Catalysis*; Plenum Press, New York (1995).
- [33] C.T. Campbell, Y.K. Sun, and W.H. Weinberg, *Chem. Phys. Lett.* **179**, 53 (1991).
- [34] A. Fahmi and R.A. van Santen, to be published.

Chapter 6

Promoting Effect of Chlorine on the Adsorption of Oxygen and the Epoxidation of Ethylene on Ag(110)¹

6.1 Abstract

Density functional calculations have been used to study the effect of coadsorbed chlorine atoms on the chemisorption of atomic oxygen on Ag₄, Ag₁₀, Ag₁₄, and Ag₂₆ cluster models representing the Ag(110) surface. The chlorine atoms introduce in most cases an antibonding interaction between silver and the chemisorbed atomic oxygen that weakens the chemisorptive bond strength. To model the catalysis of the epoxidation of ethylene we investigated the interaction between the adsorbed oxygen and an incoming ethylene molecule. The presence of chlorine changes the character of the interaction between an ethylene molecule and an adsorbed oxygen atom from repulsive to attractive. Both factors can explain the enhanced activity of the silver catalyst in the ethylene epoxidation process in the presence of chlorine. Further study should reveal if this is the only mechanism that explains the promoting mechanism of chlorine, or that perhaps the enhanced epoxidation selectivity can also be explained by an increased inhibition of the combustion reaction.

¹M.A. van Daelen, Y.S. Li, and J.M. Newsam, to be published.

6.2 Introduction

Silver has been used for many decades as a catalyst for the partial oxidation of ethylene to ethylene epoxide, a key industrial process that exceeds several billion dollars in revenue each year [1, 2]. Silver as a catalyst is unique since it can adsorb oxygen dissociatively while forming relatively weak bonds with atomic oxygen. The presence of these species allows formation of epoxide upon reaction with ethylene. The selectivity of epoxidation is determined by the relative rates of the epoxidation and the complete oxidation (combustion) reaction. Alkali metals and chlorine, among others, are used commercially as moderators to increase the epoxidation selectivity [1, 2].

Some experimental reports claim that adsorbed O_2 can react directly to an epoxide, but most experimental evidence points to atomic oxygen as the reactive species that is formed by dissociative adsorption of O_2 . Support for this mechanism comes from experimental data on the selectivity of this reaction. If we assume that only adsorbed dioxygen will react with ethylene, and that atomic oxygen takes part in the combustion reaction, six ethylene molecules can react to six epoxide molecules, leaving behind six adsorbed oxygen atoms. However, one ethylene molecule is needed to remove the remaining adsorbed oxygen through combustion. The theoretical maximum selectivity is therefore $6/7$ or 85.7 % [3]. Until recently, most reported selectivities were well below this value, explaining the broad support for the mechanism involving molecular oxygen. However, recent reports indicate selectivities around the maximum value, or even higher, causing an increasing support for the mechanism that has atomic oxygen as the reactive species [4].

For the mechanism involving atomic oxygen, the oxidation proceeds via

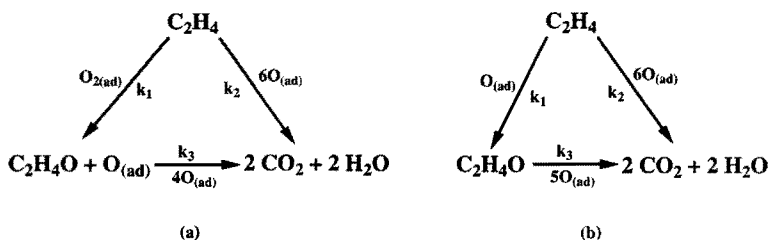


Figure 6.1. Epoxidation and combustion reactions with (a) molecular oxygen and (b) atomic oxygen as reactive intermediate in the epoxidation step.

a Langmuir–Rideal type mechanism, where the ethylene approaches an adsorbed oxygen atom from the gas phase reacting to an adsorbed epoxy species [1]. This is considered to be the rate limiting step of the epoxidation reaction, quickly followed then by desorption of the epoxide. Isotope experiments indicate that oxygen insertion may occur asymmetrically where one of the carbon atoms is electrophilically attacked by oxygen [1].

Little is known about the basis of the promoting effect of chlorine and also the location of the chlorine atoms in the catalyst is uncertain. Some evidence points to a subsurface location of the chlorine atoms, that withdraw electrons from silver atoms binding to atomic oxygen, hence weakening the surface–adsorbate bond [1]. Jørgenson and Hoffman performed tight binding slab calculations on the silver–oxygen system and found that Cl decreases the Ag–O overlap population; an indication of a weakening of the surface–oxygen bond [5]. A different explanation is given by Carter and Goddard, who argue that chlorine increases the selectivity by inhibiting the competitive combustion process [6, 7].

Theoretical studies are able to shed some light on this matter. The silver–oxygen system has been studied theoretically by various methods that have provided detailed information about the nature of the oxygen adsorption site, the oxygen–surface distance and the oxygen–surface stretch frequency [5, 8]. Van de Hoek *et al.* studied the effect of subsurface oxygen on the epoxidation of ethylene and found the oxygen to affect the epoxidation in two ways. First, it weakens the bond of the adsorbed oxygen atom by withdrawing charge from the bonding area. Second, it removes the repulsive barrier that exists for the ethylene molecule approaching the surface. Carter and Goddard [6, 7] propose two distinct atomic oxygen species, one oxygen atom in a long bridge site ($\text{di-}\sigma$) and an oxygen atom adsorbed in a 3–coordinate binding site (di-oxylradical) located on the sides of the troughs of the (110) surface. The bridge site is slightly lower in energy than the 3–fold site and only at coverages $\theta > 0.5$, 4–fold sites are being occupied. The authors suggest that the di-oxylradical is the reactive species, while $\text{di-}\sigma$ oxygen is relatively inert. Chlorine promotes the epoxidation by effectively blocking the bridge sites, forcing oxygen to occupy the slightly less stable but more reactive 3–fold sites.

In this paper, we investigate the influence of chlorine atoms on the adsorption characteristics of atomic oxygen using the density functional method in the local density approximation (LDA) [9, 10]. We will simulate a simpli-

fied epoxidation mechanism where the ethylene is approaching symmetrically, forming an epoxide with an oxygen adsorbed in a long bridge site. This can answer the question if chlorine directly affects the activity of the epoxidation reaction. Further study will be needed to evaluate the importance of the mechanism whereby chlorine increases the selectivity by inhibiting the combustion reaction.

The use of clusters as models for extended systems within the LDA scheme has provided physically reasonable descriptions of such properties as bond lengths, vibrational frequencies, and binding energies arising from the short-range metal-adsorbate interactions in a range of systems. Reported typical examples include various studies of chemisorption on metals such as Ni, Pd, and Pt [11]. In most cases, the calculations have proven to give an accurate description of the metal-adsorbate interactions, although for modeling single crystal surfaces using finite clusters, care should be taken that properties of interest have converged with cluster size.

6.3 Computational Details

The computations are performed using the density functional package DMol [12], in which molecular orbitals are represented as linear combinations of numerically generated basis functions. The basis sets for silver, oxygen and chlorine are of double zeta quality and polarization functions have been added. A frozen core approximation is used for the Ag 1s-4p and Cl 1s-2p shells. The exchange-correlation energy is described by the Von Barth-Hedin potential [13]. We employ Ag₄, Ag₁₀, Ag₁₄, and Ag₂₆ clusters as models for the Ag(110) surface (Figure 6.2), using geometry and distance as in the bulk material (fcc structure with lattice constant of 4.09 Å). Since experiments suggest that a chemisorbed oxygen atom occupies the long bridge site at less than half monolayer coverages [14], we have focused our attention on this adsorption configuration, although the 3-coordinated oxygen species as proposed by Carter and Goddard [6, 7] also deserve attention. The long bridge site is in fact a 4-fold coordinated site for atomic oxygen since the atom is also coordinating to two atoms in the second layer of metal atoms. This better explains the preference for this site as atomic adsorbates in general prefer to adsorb in high coordination sites.

The distance between the oxygen atom and the Ag surface is optimized on all the cluster models in the presence and absence of chlorine atoms. Unfor-

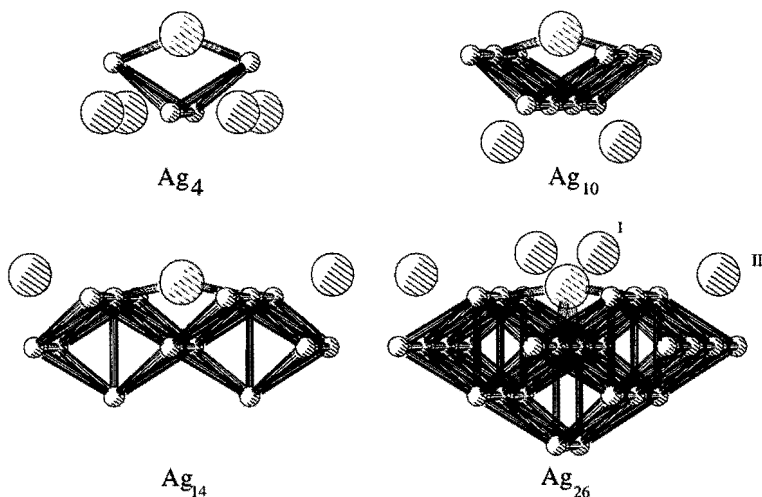


Figure 6.2. Ag_4 , Ag_{10} , Ag_{14} , and Ag_{26} clusters with oxygen adsorbed in the long bridge site. Different chlorine positions are indicated for the Ag_{26} cluster (see text).

tunately, there is no direct experimental data available on the exact location of chlorine atoms in this system. A subsurface location seems unlikely since the hollow interstitial sites are too small to accommodate an atom the size of Cl. A typical Ag–Cl bond length is 2.55 Å for bulk silver chloride, while 6-fold coordinated chlorine in a hollow site would, without reconstruction, allow for a Ag–Cl distance of only 2.00 Å. For Ag_{14} and Ag_{26} the chlorine atoms were put in 3-fold surface sites, with a Ag–Cl distance of 2.55 Å. The Ag–Cl distances were kept fixed in the optimization. For the smaller clusters there are no real surface sites available, forcing us to place them in hollow sites on the opposite side of the cluster. Because of its size, the 26-atom cluster allows us to study local adsorbate relaxation of those surface metal atoms that are fully coordinated in the surface. This effect can be an important stabilization factor and could also influence the oxygen–surface stretch frequency.

The location of the stationary points on the epoxidation reaction path was roughly determined by calculating the total energy of the surface–adsorbate system on a two dimensional grid, for which we varied independently the oxygen–surface and the ethylene–oxygen separation, while keeping the in-

ternal coordinates of the ethylene molecule frozen. The energy minimum is refined by moving all adsorbate atoms in the direction of analytically calculated forces until these are smaller than 0.01 eV/bohr. This procedure results in the detailed geometry and energetics of the product state of the ethylene epoxidation. The transition state for the epoxidation reaction is located using a “normal mode following” algorithm developed and implemented by Baker [15], by optimizing all degrees of freedom of the adsorbate while retaining the symmetry of the system and constraining the surface metal atoms.

6.4 Results and Discussion

In this section we describe two different aspects of the promoting effect of chlorine in the epoxidation reaction. We will first analyze the adsorption of atomic oxygen on the Ag(110) surface and changes in the bonding characteristics when chlorine is introduced. We then compute the energetics for the reaction of ethylene with the adsorbed oxygen species, again in the presence and absence of chlorine atoms. We will analyze the energetics for these processes mostly in terms of the nonlocal binding energies since these are known to give more accurate energetics as obtained from the local density approximation [16, 17].

6.4.1 Adsorption of Atomic Oxygen

Calculated adsorption parameters for atomic oxygen on the Ag₄, Ag₁₀, Ag₁₄, and Ag₂₆ clusters are listed in Table 6.1 together with available experimental data [14, 19, 18]. The error bars for reported experimental bond lengths are quite large; it is unclear whether the atom is located just below or just above the plane of the surface atoms [14]. When we allow for the larger cluster a local relaxation of the binding site, we see that, although the relaxation energy is relatively small (< 4 kcal/mol), the height of the adsorbed oxygen atom is affected significantly; the relaxation of the binding site atoms allows the oxygen atom to sink deeper into the surface. Taking this relaxation into account results in adsorbate–surface vibrational frequencies that are in better agreement with experiment. As expected, for bond lengths and vibrational frequencies, there is a good agreement between our cluster results and experiments because these parameters are known to be “localized”; they are mainly governed by short range interactions. The vibrational frequencies

Table 6.1. Calculated chemisorption energies (ΔE_{ads} , in kcal/mol) for atomic oxygen on cluster models of the Ag(110) surface, distances from O to the plane through the first layer Ag atoms (r , in Å), vibrational frequencies (ω , in cm^{-1}) for oxygen adsorption on cluster models of the Ag(110) surface in the presence and absence of chlorine, and the experimental values. For the 26-atom cluster different locations of chlorine atoms are indicated, corresponding to Figure 6.2. Indicated is if the local environment of the adsorption site was relaxed (see text).

without Cl	E_{ads}		r	ω		
	L	NL				
Ag ₄	-120	-93	0.30	277		
Ag ₁₀	-97	-51	0.30	253		
Ag ₁₄	-105	-80	0.54	239		
Ag ₂₆	-113	-86	0.37	257		
Ag ₂₆ (rel)	-116	-89	0.20	314		
exptl	-80 ^a		0.0 ^{+0.7} _{-1.0} ^b	310 ^c		
other calculations ^d						
Ag ₄	101	-	0.33	286		
Ag ₁₀	66	-	0.34	257		
Ag ₂₄	87	-	0.49	265		
with Cl	E_{ads}		r	Δr	ω	$\Delta\omega$
	L	NL				
Ag ₄ + 4Cl	-57	-34	(+59)	0.82 (+0.52)	238	(-39)
Ag ₁₀ + 4 Cl	-114	-92	(-41)	0.61 (+0.31)	233	(-20)
Ag ₁₄ + 2 Cl	-93	-69	(+13)	0.45 (-0.09)	234	(-5)
Ag ₂₆ + 2 Cl I	-123	-93	(-7)	0.26 (-0.11)	308	(+69)
Ag ₂₆ + 2 Cl II	-106	-64	(+22)	0.37 (0.00)	242	(-15)
Ag ₂₆ + 2 Cl II (rel)	-109	-66	(+23)	0.01 (-0.19)	300	(-14)
Ag ₂₆ + 4 Cl	-118	-85	(+1)	0.30 (+0.04)	261	(+4)
Ag ₂₆ + 4 Cl (rel)	-121	-89	(+1)	0.20 (0.00)	295	(-19)

^a From reference [7]. ^b Reference [14] gives an upper and lower limit for the Ag-O distance. ^c Reference [18]. ^d Reference [8].

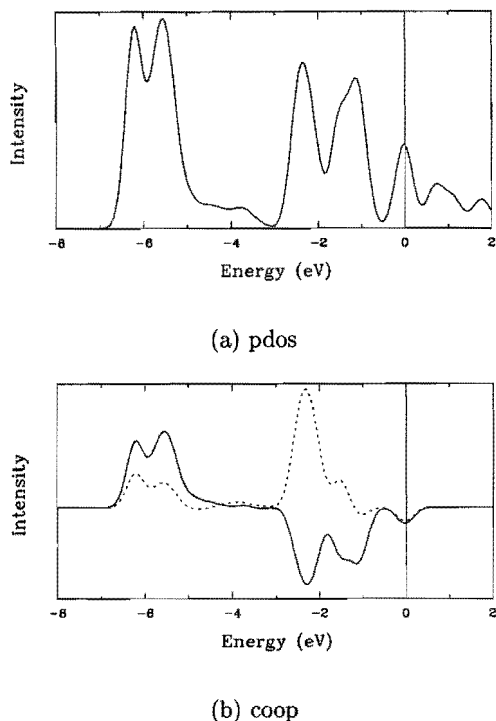


Figure 6.3. (a) The partial density of states (PDOS) of the O-2p orbitals and (b) the crystal orbital overlap population spectrum (COOP) of the interactions between O-2p and Ag-d orbitals (solid) and between O-2p and Ag-sp orbitals (dashed). The Fermi energy is set to zero.

are significantly lower than experiment for the cluster where we did not allow the surface to relax. For the 26-atom cluster the stretch frequency after local relaxation of the surface was 310 cm^{-1} , in good agreement with the experimental value of 300 cm^{-1} .

The calculated binding energies show a significant size dependence, but we see reasonable agreement between the nonlocal binding energy for the 14 and 26-atom cluster and the experimental value. The local binding energies are about 20–25 % too low, which is typical in the LDA approximation. The nonlocal binding energy on the 10-atom cluster is significantly lower than experiment (-51 vs. -80 kcal/mol). This cluster is probably not a suitable model to study oxygen adsorption, as a similar deviation was found using the HFS-LCAO method on the same system [8]. This method uses the local X_α potential, which is very similar to DFT in the LDA approximation.

To study the character of the bond between oxygen and the surface we plotted the partial density of states (PDOS) of the p orbitals of the chemisorbed oxygen atoms, and the crystal orbital overlap population (COOP)

[20] between the O-2p and Ag-d and Ag-sp orbitals for the Ag₁₄ system (Figure 6.3(a)). The COOP spectrum indicates whether the states in the PDOS spectrum are bonding (positive COOP) or anti-bonding (negative COOP). As reported previously [5, 8], there are two bands in the partial density of states of the O-2p orbitals. The band at lower energy is mainly responsible for bonding between the O-2p and Ag-d orbitals, as suggested by the positive COOP in Figure 6.3(b). The bonding interaction between O-2p and Ag-sp orbitals also contributes slightly to this lower energy band. The higher energy band is the combination of the antibonding interaction between O-2p and Ag-d orbitals and the bonding interaction between O-2p and Ag-sp orbitals. Due to the cancellation of these interactions this band is approximately Ag-O nonbonding in nature. These calculations provide a picture of the Ag-O bonding similar to that suggested by Van den Hoek and coworkers [8], namely a Ag-O bonding band about 6 eV below the Fermi level and a nonbonding band just below the Fermi energy.

We now shift attention to changes in the system when introducing chlorine. The general trend is, with some exceptions discussed below, that the presence of the chlorine atoms weakens the surface-oxygen bond. For the 26-atom cluster the effect of chlorine is more subtle as it turns out that the position of the chlorine atom with respect to the adsorption site is also a factor that determines how the bond will be affected. The type I clusters have chlorine in a 3-fold site, coordinated to a silver atom that is not directly binding to the oxygen atom, but that is a second nearest neighbor of the adsorbed oxygen atom Figure 6.2. In the type II clusters the chlorine is also 3-fold coordinated, but now bonded directly to the metal atom binding the adsorbed oxygen atom. The cluster with four chlorine atoms has two pairs of atoms, one in each of those geometries.

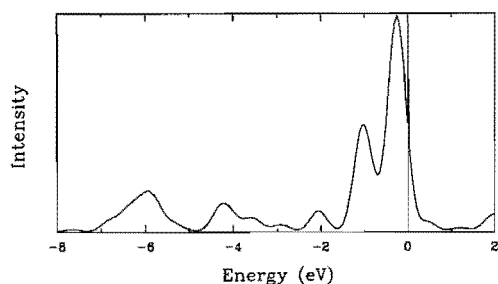
If located in a first nearest neighbor position (type II) the chlorine clearly weakens the Ag-O interaction; the cluster with chlorine is 22 kcal/mol less stable than the cluster without chlorine. In contrast, the presence of chlorine makes the interaction with oxygen 7 kcal/mol more stable for the type I cluster, where chlorine is a second nearest neighbor. This effect is similar to the observed bond weakening of NH₃ on Cu(111) in the presence of surface oxygen [21]. On the cluster with four chlorine atoms both effects approximately cancel out, resulting in a destabilization of oxygen of only 1 kcal/mol.

This is accompanied by a decrease in the surface-oxygen vibrational frequency, and an increase in the surface-oxygen bond length, as shown by

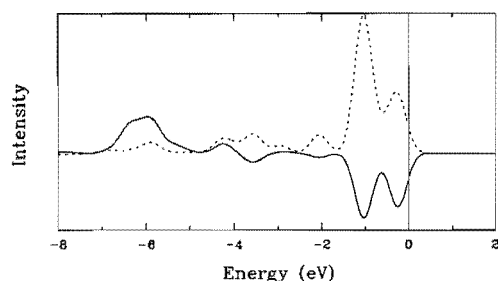
Table 6.2. Mulliken populations for adsorbate, cluster, and chlorine atoms. Populations $\times 10^3$; cluster models as in Figure 6.2. For the silver atoms that are coordinating to the oxygen is indicated if these are in the first or second layer.

	Ag(I)	Ag(II)	O	Cl
Ag ₄	-175	175		
Ag ₄ O	293	143	-764	
Ag ₄ -Cl ₄	473	414		-443
Ag ₄ O-Cl ₄	557	487	-656	-358
Ag ₁₀	-7	-40		
Ag ₁₀ O	140	13	-670	
Ag ₁₀ -Cl ₄	196	230		-481
Ag ₁₀ O-Cl ₄	426	306	-792	-492
Ag ₁₄	19	-21		
Ag ₁₄ O	207	30	-709	
Ag ₁₄ -Cl ₄	140	-35		-410
Ag ₁₄ O-Cl ₄	287	91	-711	-395
Ag ₂₆	12	30		
Ag ₂₆ O	146	105	-706	
Ag ₂₆ -Cl ₄	122	-34		-381
Ag ₂₆ O-Cl ₄	284	120	-743	-372

results in Table 6.1. The oxygen-surface distance is increased from 0.3 Å to 0.82 Å for Ag₄, and from 0.3 Å to 0.61 Å for the Ag₁₀ cluster. In contrast, for the 14 and 26-atom clusters we see only small changes in the surface-oxygen bond length. For the relaxed surface calculations oxygen in some cases lowers to a position just below the plane of the Ag atoms. This seems to contradict the observed decrease in binding energy. A possible explanation could be that the relaxation of Ag atoms is exaggerated because we did not optimize the positions of Cl. These might pull Ag atoms away from O, leaving more room for the oxygen atom to lower its height. The weakening of the Ag-O bond appears to be less pronounced for the larger clusters, because the polarization of the cluster caused by chlorine is stronger on a per atom basis for smaller clusters. The overall composition of the adsorption region, for in-



(a) pdos



(b) coop

Figure 6.4. Same as in Figure 6.3, now in the presence of coadsorbed chlorine atoms.

stance, changes from Ag : Cl = 1 (Ag_4Cl_4) to Ag : Cl = 6.25 ($\text{Ag}_{26}\text{Cl}_4$). The amount of charge that is actually withdrawn from the bonding area when chlorine is introduced is 0.648 ($0.473+0.175$) for the 4-atom cluster, and only 0.110 ($0.122-0.012$) for the 26-atom cluster (Table 6.2). More surface experiments seem necessary to determine the detailed surface composition of the catalyst so that these theoretical models can be improved.

Changes similar as found here for chlorine have been observed in the presence of oxygen [8], that is also known to act as a moderator in the ethylene epoxidation reaction. To understand the nature of this effect, we calculated the partial density of states for the O-2p orbitals and the COOP for the various Ag-O and Cl-O interactions in the case of the Ag_{14} cluster (Figure 6.4). The O-2p band at 6 eV below the Fermi level has split, due to the interaction of the Ag 4d band with chlorine states.

The emerging O-2p band at 4 eV below E_F is a combination of an antibonding interaction between O-2p and Ag-4d, and two antibonding interactions between O-2p and Ag-sp, and O-2p and Cl-sp, respectively. However,

because of the cancellation between the antibonding and bonding interactions, this is approximately a nonbonding band. In addition to the original Ag–O interactions just below E_F , we also see new antibonding and bonding interactions between oxygen and chlorine. Both the bonding and antibonding states are occupied and lead therefore to a weakening of the chemisorption bond. This is the primary mechanism responsible for the weakening of the Ag–O bond strength by chlorine.

The changes introduced by chlorine on the adsorption of oxygen are very subtle, but it might explain the observed enhanced selectivity in the epoxidation reaction. The dependencies of the adsorption properties on surface coverage and cluster size is worth further study for instance by using a slab approach.

6.4.2 Epoxidation of Ethylene

To investigate the implications of the weakening of the oxygen–surface bond to the catalysis of the epoxidation reaction, we have studied the interaction between an incoming ethylene molecule and chemisorbed oxygen Ag_4 clusters in the presence and absence of chlorine. The ethylene molecule is configured to approach the oxygen atom with its molecular plane parallel to the silver surface as proposed by Van Santen and Kuijpers [1]. To reduce the dimensions for the transition state optimization the path for the approaching ethylene molecule was chosen to obey the symmetry of the cluster (C_{2v}). Van de Hoek [8] also studied a simplified asymmetric attack, where ethylene coordinates with the C–atom and C–H bond, respectively. However, since the number of degrees of freedom for the asymmetric mechanism increases significantly (from 6 for C_{2v} to 12 for C_s) we were not able to perform a full geometry optimization for these structures at the same level of detail as the symmetric attack.

Intuitively, we expect three stationary points on the reaction pathway that are of interest. The reactant state is the silver surface with an adsorbed oxygen atom and the ethylene molecule at infinite separation. The other potential energy minimum is when the epoxy bond has been formed and the epoxide is (weakly) attached to the surface. Somewhere in between the system is expected to traverse through a transition state.

In a first attempt to map out the ethylene–AgO potential energy surface (PES) we calculated for a frozen ethylene molecule the interaction energy

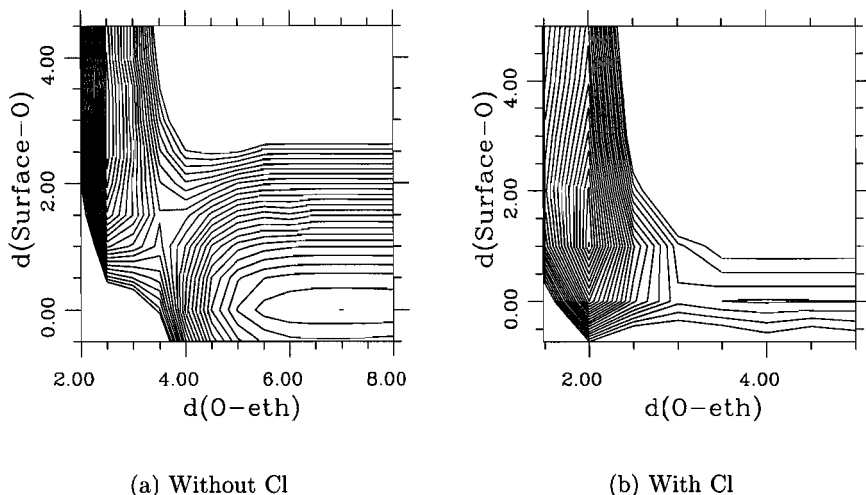


Figure 6.5. Potential energy surface for ethylene epoxidation. Neighboring contour lines differ 10 kcal/mol in energy.

with the AgO system with varying surface–oxygen and oxygen–ethylene distances (Figure 6.5). These rough profiles already provide valuable information about the oxygen–ethylene interaction and the influence of the chlorines. For the epoxidation reaction in the absence of Cl the energy surface indicates a significant barrier, whereas there is no barrier for ethylene approaching the surface in the presence of chlorine. The epoxide product remains on the surface in a weakly adsorbed state.

Introduction of chlorines drastically lowers the reaction barrier and changes the character of the oxygen–ethylene interaction from repulsive to attractive. The profiles are very similar to those found by Van den Hoek *et al.* [8] for identical systems in the presence of subsurface oxygen. This similarity shows that the moderating mechanism is essentially the same for chlorine and subsurface oxygen.

If we include the energetics for the gas phase reactants and products we can construct an energy profile for the epoxidation reaction. This is done for the case without chlorine in (Figure 6.6). The activation barrier is 39 kcal/mol for the forward reaction (epoxidation) and 42 kcal/mol for the reverse reaction. The adsorbed epoxide product is 3 kcal/mol lower in energy than the reactant state: the free ethylene molecule and the cluster. In the case without chlorine the epoxide product is –3.5 kcal/mol binding

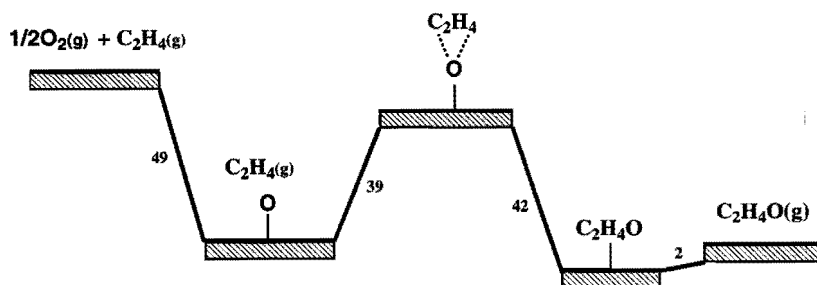


Figure 6.6. Energy profile for epoxidation in the absence of chlorine. Energies are in kcal/mol.

with respect to the gas phase species, in the case with chlorine this is -5 kcal/mol. At the product state, the oxygen–ethylene distance is 1.46 \AA , very close to the equilibrium distance for ethylene epoxide of $1.47 \pm 0.01 \text{ \AA}$. The epoxide bond has formed and the oxygen is binding weakly to the surface (-2 kcal/mol).

6.5 Conclusions and Recommendations

We have studied the promoting effect of chlorine on the adsorption of oxygen and the epoxidation of ethylene on a Ag(110) surface with both density functional theory with both local and nonlocal functionals. We found that chlorine atoms introduce a subtle antibonding interaction between silver and chemisorbed atomic oxygen that weakens the silver–oxygen bond strength. The location of the chlorine atoms with respect to the oxygen binding site is an important factor determining the effect on the oxygen chemisorption strength. The bonds are significantly weakened when Cl is binding to one of the Ag atoms that is binding O, whereas it is actually increasing the Ag–O bond strength if Cl is coordinated further from the binding site.

The potential energy surfaces were mapped out on the smallest cluster for the adsorbed oxygen atom and an incoming ethylene molecule. In the case without chlorine a reaction barrier was found of 39 kcal/mol with respect to the gas phase state (chemisorbed oxygen and a free ethylene molecule) and 42 kcal/mol with respect to the product state (weakly adsorbed ethylene epoxide). The presence of chlorine atoms essentially removes this reaction barrier and changes the character of the interaction between an incoming

ethylene molecule and the adsorbed oxygen atom from repulsive to attractive. Both these factors contribute to the moderating effect of chlorine in the epoxidation of ethylene. This moderating mechanism appears very similar to what has previously been found for subsurface oxygen.

Future work could address the effect of chlorine moderators on the competing combustion reaction. This could be an equally important mechanism explaining the enhanced epoxidation selectivity in the presence of chlorine. Slab calculations will be useful to eliminate any cluster size dependencies, as we experienced that in this study the 10-atom cluster produced unreliable energetics. It will be interesting then to also look at the 3-fold adsorption site proposed by Carter and Goddard, and compare its stability relative to the long bridge site. This could be done at different degrees of Cl coverage to verify the hypothesis that at higher coverages there will be an increase in oxygen occupying 3-fold surface sites. A slab approach will also allow a more rigorous treatment of surface relaxation effects, which was found to be of some importance.

References

- [1] R.A. van Santen and H.P.C.E. Kuipers, *Adv. Catal.* **17**, 265 (1987).
- [2] C.T. Campbell and M.T. Paffett, *Surf. Sci.* **139**, 396 (1984).
- [3] M. Barteau and R.J. Madix, in: *The Chemical Physics of Solid Surfaces and Heterogeneous Catalysis*, D.A. King and D.P. Woodruff, eds. Vol. 4 ch. 4. Elsevier, Amsterdam (1982).
- [4] A. Ayame, T. Kimura, M. Yamaguchi, H. Miura, N. Takeno, H. Kanoh, and I. Toyoshima, *J. Catal.* **79**, 233 (1983).
- [5] K.A. Jørgensen and R. Hoffman, *J. Phys. Chem.* **94**, 3046 (1990).
- [6] E.A. Carter and W.A. Goddard III, *J. Catal.* **112**, 80 (1988).
- [7] E.A. Carter and W.A. Goddard III, *Surf. Sci.* **209**, 243 (1988).
- [8] P.J. van den Hoek, E.J. Baerends, and R.A. van Santen, *J. Phys. Chem.* **93**, 6469 (1989).
- [9] P. Hohenberg and W. Kohn, *Phys. Rev. B* **136**, 864 (1964).
- [10] W. Kohn and L.J. Sham, *Phys. Rev. A* **140**, 1133 (1965).
- [11] J.K. Labanowski and J.W. Andzelm, eds., *Density Functional Methods in Chemistry*, Springer-Verlag, New York (1991).
- [12] B. Delley, *J. Chem. Phys.* **92**, 508 (1990).
- [13] U. von Barth and L. Hedin, *J. Phys. C* **5**, 1629 (1972).

- [14] W. Heiland, F. Iberl, E. Taglauer, and D. Menzel, *Surf. Sci.* **53**, 383 (1975).
- [15] J. Baker, *J. Comp. Chem.* **7**, 385 (1986).
- [16] P.H.T. Philipsen, G. te Velde, and E.J. Baerends, *Chem. Phys. Lett.* **226**, 583 (1994).
- [17] M. Neurock and R.A. van Santen, *J. Am. Chem. Soc.* **116**, 4427 (1994).
- [18] B.A. Sexton and R.J. Madix, *Chem. Phys. Lett.* **76**, 294 (1980).
- [19] H. A. Engelhardt and D. Menzel, *Surf. Sci.* **57**, 591 (1976).
- [20] R. Hoffmann, *Rev. Mod. Phys.* **60**, 601 (1988).
- [21] M. Neurock, R.A. van Santen, W. Biemolt, and A.P.J. Jansen, *J. Am. Chem. Soc.* **116**, 6860 (1994).

Chapter 7

Theoretical and Experimental Study on the Selectivity of Dehydrogenation of α -Limonene in ZSM-5 and Zeolite-Y¹

7.1 Abstract

Dehydrogenation of the natural terpene α -limonene to the industrially important p-cymene was studied over two zeolite supported Pd catalysts, ZSM-5 and zeolite-Y. Reactor tests indicate that transalkylation of the p-cymene product can be avoided by employing the shape selective properties of a medium-pore ZSM-5 catalyst. The diffusion properties of the three isomers of cymene were then calculated in the two zeolites using molecular mechanics. For ZSM-5, p-cymene was found to have the the lowest barrier of the three isomers for diffusion through the straight, spherical channel of the zeolite. For zeolite-Y differences in diffusivity for the three isomers were very small. Theory and experiment showed, in excellent agreement, that only ZSM-5 selectively produces p-cymene. This work shows that molecular mechanics is a powerful and reliable method for the screening of zeolites for performing shape selective catalysis.

¹M.A. van Daelen, P. Weirich, A.M. Gorman, and W. Hölderich, to be published.

7.2 Introduction

p-Cymene is an important starting material for the production of many intermediates and end products, such as p-cresol, fragrances, herbicides, pharmaceuticals, and heat transfer media [1, 2]. Conventionally, cymenes are manufactured by Friedel-Crafts-alkylation of toluene with propene using hazardous catalysts like AlCl_3 [3]. However, this process is non-selective and leads to cymene mixtures in thermodynamic equilibrium composition.

Recently, selective synthesis of p-cymene by zeolites has been thoroughly investigated [4, 5, 6]. Zeolite based processes avoid (1) the disposition of spent catalyst, (2) product contamination by the catalyst, (3) separation of the catalyst from the product, and (4) corrosion of the reactor and tubes. However, the formation of undesired n-propyltoluene in addition of p-cymene is seen particularly on MFI type zeolites (ZSM-5), whereas large pore zeolites yield significant amounts of m- and o-cymene, besides p-cymene.

Other approaches to synthesize p-cymene selectively start from α -limonene, a material with a structure very similar to p-cymene. α -Limonene is widely available as a byproduct in the production of orange juice. Earlier studies [7, 8] showed that α -limonene can be disproportionated to p-menthane and p-cymene over Pd and Pt catalysts on carrier materials. Also Se promoted PdO on a carrier material has been suggested as a catalyst [9]. Recently, Hölderich *et al.* reported a zeolite supported Ce promoted Pd catalyst for enhanced dehydrogenation activity during α -limonene conversion [10].

In this study, we investigated the impact of zeolite structure, acidity and preparation method upon α -limonene conversion. To establish a relationship between zeolite structure and selectivity we performed a modeling study on the diffusion behavior of the three cymene isomers in zeolite-Y and ZSM-5. These calculations have demonstrated the ability to provide valuable insights into the dynamical behavior of guest molecules in porous materials [11]. The predictions of the computational study are compared to the results of the reactor tests. This will indicate the value of these methodologies as predictive tools in future studies.

7.3 Methodology

7.3.1 Catalyst Preparation

All zeolite supported samples were prepared by ion-exchange of two parent NaZSM-5 (AlSi-Penta-SN55 and AlSi-Penta-SN27) and a parent H-ZSM-5 (AlSi-Penta-SH55), provided by VAW Aluminium AG. The H-ZSM-5 and a US-Y zeolite (CBV760, provided by the PQ Corp.) were used as such. The crystallinity of the zeolites was verified by X-ray diffraction. Prior to ion-exchange, the zeolites were extruded to cords 2 mm in diameter, dried overnight in air at 110°C overnight and calcined in air at 550°C for 6 h to remove the binder. The catalyst was then crushed over sieves to particles of 1.0–1.6 mm diameter.

The zeolite pellets were used without prior washing or neutralization. First, Ce was inserted in the zeolite by circulating 800 ml of a 0.1 M $\text{Ce}(\text{NO}_3)_3$ -solution over 80 g of the zeolite particles at 80°C for 24 h. The zeolite was subsequently filtered, washed with 2 L doubly de-ionized (DDI) water, dried in air at 110°C overnight and calcined in air at 550°C for 6 h. The Ce-exchange was performed three times. Pd-exchange was performed in the same way on the parent zeolite and the Ce-exchanged zeolite by circulating 800 ml of a $\text{Pd}[\text{NH}_3]_4(\text{NO}_3)_2$ -solution over 20 g of the zeolite for 24 h at 80°C. The catalyst was subsequently filtered, washed with 2 L DDI-water, dried in air at RT and stored until used. Catalysts denoted *slow calc* were calcined *in situ* in a flow of pure oxygen (2000 ml/min) by slowly ramping the temperature with 0.5 K/min from RT to 500°C. The catalyst is then held at 500°C for 2 h and subsequently cooled down to RT in flowing N_2 . Catalysts without denotation or denoted *fast calc* were calcined under static conditions in air by ramping the temperature from RT to 550°C with 2 K/min in an oven. All catalysts were reduced in flowing hydrogen *in situ* prior to reaction by ramping the temperature with 8 K/min from RT to 230°C and then with 1 K/min from 230°C to 250°C. The temperature is held for 20 min at 250°C after which it is brought to reaction temperature in flowing N_2 .

7.3.2 α -Limonene Conversion

α -Limonene conversion was studied in an integral reactor at 250°C and 300°C. The catalysts were used as pellets of 1.0–1.6 mm diameter in a stainless steel reactor with an internal diameter of 6 mm. 3.2 g of catalyst is used

Table 7.1. Potential parameters used in the diffusion path simulation; aromatic carbon (cp), sp-3 hybridized carbon (c), and hydrogen (h).

Bond lengths: $E = k_i(r - r_0)^2$				
Potential types		r_0 (Å)	k_i (kcal mol ⁻¹ Å ⁻²)	
c	h	1.105	340.6175	
cp	h	1.080	363.4164	
cp	cp	1.340	480.0000	
cp	c	1.510	283.0924	
Bond angles : $E = k_i(\theta - \theta_0)^2$				
Potential types			r_0 (Å)	k_i (kcal mol ⁻¹ Å ⁻²)
h	c	h	106.4	39.5
h	c	c	110.0	44.4
cp	cp	h	120.0	37.0
cp	cp	cp	120.0	90.0
h	c	cp	110.0	44.4
c	cp	cp	120.0	44.2
cp	c	cp	110.5	46.6
Non bonded interactions: $E = A_{ij}/r^{12} - B_{ij}/r^6$				
Potential types		A (kcal mol ⁻¹ Å ¹²)	B (kcal mol ⁻¹ Å ⁶)	
h		7108.4660	32.87076	
c		1981049.2250	1125.99800	
cp		2968753.3590	1325.70810	
si		3149175.0000	710.00000	
o		272894.7846	498.87880	

for each experimental run. α -Limonene of 97 is brought into the reactor by means of a volumetric pump at a rate of 5 ml/h. The feed evaporates at the reactor inlet and the vapor is transported via a flow of 4 Nl/h N₂ over the catalyst bed. The resulting α -limonene partial pressure in the feed is 16 kPa, the resulting WHSV is 1.3 h⁻¹. On-line analysis of the products was made with a Siemens RGC 202 system, equipped with a 50 m OV 1701 CS column and a flame ionization detector.

7.3.3 Simulations

The molecular mechanics calculations were carried out using the Discover simulation package [12], part of the Solids_Diffusion module of the InsightII program [13]. The potential parameters were taken from the consistent valence forcefield of Hagler *et al.* [14], shown in Table 7.1. The nonbonded interaction potentials were of the Lennard–Jones form combined with a term describing the electrostatic interaction,

$$E_{nb} = \sum_i \sum_{j>i} \left[\frac{A_{ij}}{r_{ij}^{12}} - \frac{B_{ij}}{r_{ij}^6} + \frac{q_i q_j}{r_{ij}} \right], \quad (7.1)$$

where q_i and q_j are partial atomic charges, and the summation extends over all pairs of atoms i, j . Constants A_{ij} and B_{ij} are derived from atomic Lennard–Jones parameters using combination rules:

$$A_{ij} = (A_i A_j)^{1/2}; B_{ij} = (B_i B_j)^{1/2}. \quad (7.2)$$

The intra-molecular interactions of the sorbate were described with regular bond length and bond angle expressions (Table 7.1). During these calculations the framework was held fixed at the crystallographically determined geometry.

ZSM-5 has a two dimensional intersecting pore system of sinusoidal and straight channels. The pores are approximately circular with a pore diameter of 5.5 Å. The zeolite-Y structure can be thought of as being made up of sodalite cages, fused through their six-ring faces (diameter 2.2 Å) by hexagonal prisms (double six-rings) (Figure 7.1). This creates large spherical cavities, or supercages, of approximate diameter 13 Å. Access to the supercages is afforded by twelve-ring windows with a free aperture of 7.3 Å in diameter, which are tetrahedrally distributed around the center of the supercage. The cymene isomers are shown in Figure 7.2. *p*-Cymene has the smallest cross section of the three isomers.

7.4 Results and Discussion

7.4.1 Experimental

As was confirmed by their XRD patterns all zeolite samples were highly crystalline. Catalytic studies with zeolites ZSM-5 and zeolite-Y have been done

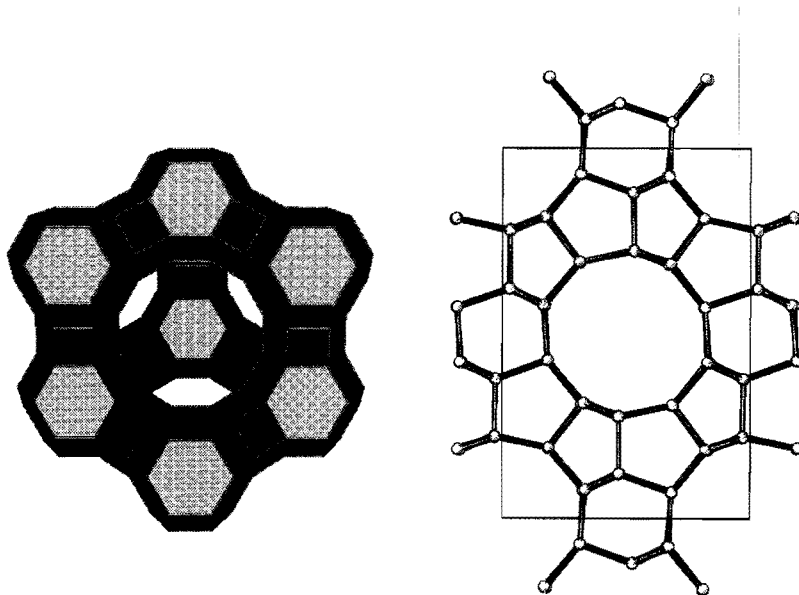


Figure 7.1. Crystal structures of zeolite-Y and ZSM-5.

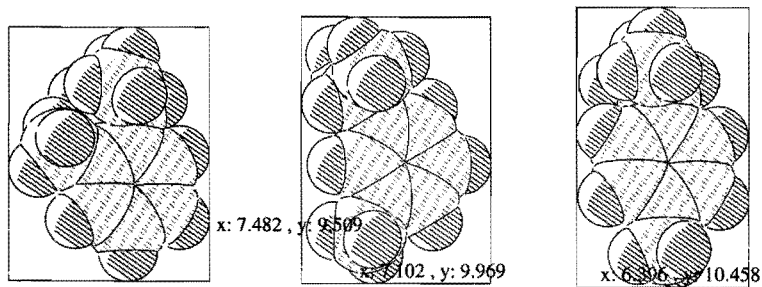


Figure 7.2. Structures and effective dimensions (in Å) of (a) ortho-, (b) meta-, and (c) para-cymene.

Table 7.2. Impact of zeolite structure on shape-selectivity for ZSM-5 and zeolite-Y at 473°C and 573°C. WHSV is 1.3 h⁻¹ and TOS is 0.5 h.

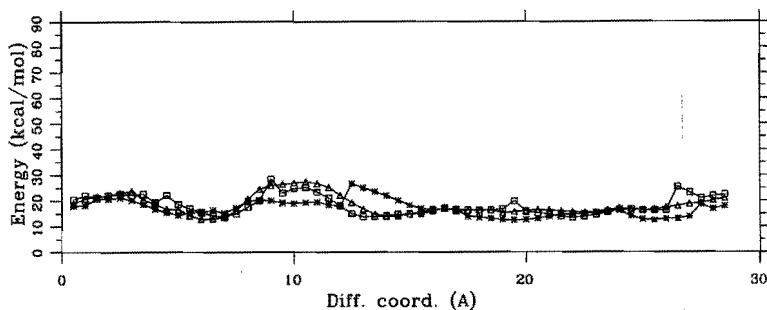
zeolite	H-ZSM5	US-Y	H-ZSM5	US-Y
temperature [K]	473	473	573	573
α -limonene conversion [wt%]	87.8	99.5	99.2	100
cym. selectivity [wt%]	11.7	22.3	18.1	7.7
meta-para ratio	0.02	0.76	0.09	1.83

in H-form to investigate the impact of the zeolite structure upon shape selectivity. The results reveal that the zeolite structure has an impact on cymene selectivity. The m/p-cymene ratios obtained with zeolites ZSM-5 and Y are presented in Table 7.2 as a measure of the shape selective properties of the zeolite. α -Limonene conversion over large pore zeolite US-Y yields an initial m-/p-cymene ratio of 1.83 at 300°C, which is close to the thermodynamic equilibrium composition of m- and p-cymene of 2.0. Over the medium-pore zeolite ZSM-5 only small amounts of m-cymene are formed initially even at elevated temperatures as represented by the low value of the m-/p-cymene ratio of 0.02. No m-cymene is detected after a TOS of 4 h over ZSM-5.

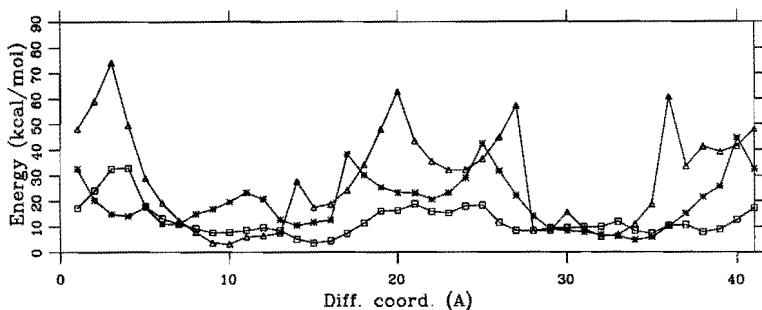
The results of this study show that α -limonene can be selectively transformed into a p-menthane terpene structure over ZSM-5. Transalkylation to m- or o-cymene or p-n-propyltoluene is inhibited due to steric constraints. Conversion over large pore Y-type zeolites yield m- and p-cymene, initially almost in thermodynamic equilibrium composition initially, expressed by the m-/p-cymene ratio of 2.0. Although zeolite cracking of p-cymene to toluene and propene and propane is dominant over acidic H-ZSM-5 or Pd/H-ZSM-5, only traces of m-cymene are found in the product. The shape selective properties of ZSM-5 are well known and have previously been used for various reactions as the xylene isomerization [15].

7.4.2 Simulations

Inspection of the shapes of the three cymene isomers indicates that each isomer has a distinct cross section. This can lead to dramatic differences in diffusivity in zeolite channels, provided that the channels have appropriate dimensions. In principle one could perform molecular dynamics calculations to calculate diffusion rates by evaluating the migration of the sorbates as a function of time. However, for large molecules, diffusion is too slow to



(a)



(b)

Figure 7.3. Energy profiles for diffusion for ortho- (Δ), meta- (*), and para-cymene (\square) in (a) zeolite-Y and (b) ZSM-5. ZSM-5 clearly exhibits differences in diffusion properties for the three isomers.

be observed on a typical molecular dynamics time scale (100 ps). By making assumptions about the diffusion pathway, however, one can calculate the variation of the interaction energy along this pathway, which provides a measure on the relative diffusion barriers of different sorbates. This approach has proven to predict reliable trends in the diffusion properties of hydrocarbons in porous oxidic materials [11]. The sorbate is minimized at regular length intervals along the diffusion path, producing the “zero kelvin” diffusion barrier. The diffusion path is defined by a pair of points at either side of the pore under investigation. At regular intervals along this path, the energy for the sorbate is minimized for the degrees of freedom perpendicular to the diffusion path in the zeolite framework. The sorbate is kept in its place by an

artificial harmonic potential applied from either anchor point. The restraint energy is subtracted at the end of the calculation. This procedure ensures that one obtains a minimum energy path for diffusion along the channel.

A computational screening of diffusion properties of the *o*-, *m*-, and *p*-cymene isomers was carried out using this *biased diffusion* methodology [16]. The minimizations were carried out using periodic boundary conditions. This increases the accuracy of the interaction energies and allows one to simulate over shorter length scale, since edge effects are eliminated. For ZSM-5 we simulated diffusion through the straight channel, which is larger in diameter than the sinusoidal channel. For zeolite-Y the diffusion channel is made up of spherical cages and the twelve ring windows connecting them. As a starting point we chose the middle of the intersection of the straight pore and the unit cell, and we simulated for the length of the cell.

Since the diffusive behavior of molecules will most importantly be determined by the topology of the pore system, and only to a lesser degree by the presence of extra framework particles such as metal clusters and extra framework cations, we have performed the simulation on the silicious analogues of these zeolites, silicalite (ZSM-5) and faujasite, also for reasons of computational expediency. Also because the majority of the interaction is with the framework oxygen, the strict Si/Al ordering is of less importance. The zeolite structural models were taken from the literature [17, 18].

Figure 7.3(a) shows the energy profiles for the diffusion of the three isomers in ZSM-5. The variation of the interaction energy between the host framework and the guest molecule provides information on the relative diffusion barriers of different guest molecules. It is evident that the diffusion of the *para* isomer is significantly less hindered than the diffusion of the *ortho* and *meta* isomers. The barriers for *para* diffusion are of the order of 30 kcal/mol while the barriers for the *meta* and *ortho* isomers are 50 and 75 kcal/mol, respectively. These differences in diffusion barrier height will result in different life times of the molecule in the pore system. The *ortho* and *meta* isomers are clearly obstructed in ZSM-5, but they seem to interact favorably with the zeolite between the activation barriers. This is probably in the channel intersections where the sorbates are less sterically hindered. This will allow conversion of these isomers when reacting on active sites on the inner surface of the pore system. If conversion leads to the *para* form, it will be able to diffuse at relatively fast speed and be able to leave the pore system with the carrier gas. This can also rationalize the increase in the

meta-form with increasing temperature (Table 7.2). While the low barrier for para-diffusion is less affected by temperature, as it already has enough energy to surmount the barrier, the meta diffusion may increase because a higher temperature will increase the probability to overcome the diffusion barrier.

The diffusion profiles for the three isomers in zeolite-Y are different (Figure 7.3(b)). There is no significant diffusion barrier for any of the isomers. Isomerization of cymenes will not result in changes in diffusivity of the gas, and it is expected that the reaction will lead to equal proportions of the three isomers. This supports the experimental finding that this zeolite shows no noticeable selectivity for the reaction.

Besides differences in diffusion rates there might be other factors that enhances the selectivity. The reaction from limonene to cymene itself may be influenced by steric constraints imposed by the zeolite framework. The transition state for the conversion to o- and m-cymenes is likely to be more "bent" than the transition states for the para isomer. These bent transition states would be less favorable in the smaller channels and will also increase the selectivity for the para isomer, whereas these reactions would have equal probability in the gas phase. These reactions will preferably take place at the pore intersections as there is more room to accommodate a bulky transition state. Since both zeolite-Y and ZSM-5 have a two dimensional connected pore structure, it is expected that transition state selectivity as discussed here is of less importance than in one dimensional zeolitic frameworks as e.g. zeolite-L.

7.5 Conclusions

α -Limonene can be easily dehydrogenated to p-cymene, but care has to be taken to avoid the secondary reactions and rapid deactivation of the catalyst due to coke deposition and presumably Pd agglomeration. Employing a medium-pore ZSM-5 zeolite as support for the Pd catalysts avoids transalkylation of p-cymene as observed for large pore zeolite support.

Molecular mechanics calculations confirmed the experimental findings that ZSM-5 can perform the hydrogenation selectively to produce preferentially p-cymene. Zeolite-Y was predicted to have no selectivity towards any of the cymene isomers, also in agreement with the experiment. The good agreement between experiment and modeling confirms the reliability of

molecular modeling methods in the screening of zeolites for shape-selective reactions.

References

- [1] J.M. Derfer and M.M. Derfer, *Kirk-Othmer Encyclopedia of Chemical Technology* **22**, 709 (1978).
- [2] W.J. Welstead Jr., *Kirk-Othmer Encyclopedia of Chemical Technology* **9**, 544 (1978).
- [3] K. Ito, *Kirk-Othmer Encyclopedia of Chemical Technology*, p. 89 (1973).
- [4] P. A. Parikh, N. Subrahmanyam, Y. S. Bhat, and A. B. Halgeri, *Chem. Eng. J.* **54**, 79 (1994).
- [5] B. Wichterlova, A. Kapustin, and J. Cejka, *Appl. Catal. A* **108**, 187 (1994).
- [6] P. A. Parikh, N. Subrahmanyam, Y. S. Bhat, and A. B. Halgeri, *Appl. Catal. A* **90**, 1 (1992).
- [7] J. Zelinski, *Ber.* **57**, 2058 (1924).
- [8] R. P. Linstead, K. O. Michaelis, and S. L. S. Thomas, *J. Chem. Soc.*, p. 1139 (1940).
- [9] R. Martin and W. Gramlich, patents DE 36 07 448 (1987) and US 4 720 603 (1987).
- [10] W. D. Mross W. F. Hölderich, R. Fischer and F.-F. Pape, patents DE 3 513 569 (1986), US 4 665 252 (1987), and EP 0199 209 (1988).
- [11] J.A. Horsley, J.D. Fellmann, E.G. Derouane, and C.M. Freeman, *J. Catal.* **147**, 231 (1994).
- [12] Discover 4.0.0, Molecular Simulations, Inc., San Diego, CA.
- [13] InsightII 4.0.0, Molecular Simulations, Inc., San Diego, CA.
- [14] A.T. Hagler, S. Lifson, and P. Dauber, *J. Am. Chem. Soc.* **101**, 5122 (1979).
- [15] J. Wie, *J. Catal.* **76**, 433 (1982).
- [16] S.D. Pickett, A.K. Nowak, and J.M. Thomas, *Zeolites* **9**, 123 (1989).
- [17] D.H. Olson, *J. Phys. Chem.* **74**, 2758 (1970).
- [18] H. van Koningsveld, H. van Bekkum, and J.C. Jansen, *Acta Crystallogr. B* **43**, 127 (1987).

|

Summary

The first part of this thesis presents an overview of the most important modeling methods that are used nowadays in industrial catalysis. Applications are described encompassing catalyst characterization, electron microscopy, simulation of crystal morphology, and simulation of diffusion of organic molecules in porous materials. An overview is also presented of the most important quantum mechanical methods for doing electronic structure calculations, in particular density functional theory as applied to new materials. The theory underlying these calculations is summarized, and the parallelization of these programs for multi-processor architectures is discussed. Parallelization of these programs makes calculations possible on systems of realistic sizes in tractable time spans, which is particularly important in practical industrial applications. We discuss applications that treat the structure of metal clusters, C_{60} chemistry, an oxygen defect in alpha-quartz, and the structure of template molecules in zeolite synthesis.

The main focus of this thesis is the treatment of elementary reactions on metal surfaces using density functional theory. This is one of the first studies in the literature that predicts a transition state for a surface reaction from first principles calculations. This has been made possible by recent improvements in geometry optimization algorithms. We have studied the dissociation of CO and NO on cluster models of the Cu(100) and Cu(111) surfaces by fully optimizing the transition states for various possible reaction pathways. The dissociation barriers for CO are high for all reaction pathways. Because the adsorption energy for CO is low this implies that CO will generally not dissociate on copper. For NO we have calculated dissociation barriers that are significantly lower than barriers for CO, while the NO adsorption energy is substantially higher than for CO. This indicates that dissociation of NO is easier than for CO which is in agreement with experimental measurements. The transition states have very little degree of freedom which results in a low entropy for these states. The reactant states are not as 'tight' due to

translational modes of vibration on the surface that have low frequencies. Using classical transition state theory we have determined the pre-exponential factors for the dissociation and recombination reactions, which are in good agreement with experimental measurements on these systems.

In the following chapter we studied the adsorption and dissociation of the four diatomic molecules CO, NO, O₂ and N₂ on three different sites on the (100) surface of copper. The characteristic electronic structure of each of these molecules allows us to study the electronic factors that play a role for dissociation on a metal surface. The dissociation of O₂ is strongly exothermic without a significant dissociation barrier. The barrier for NO dissociation is also small and it will allow dissociation at relatively low temperatures. For NO on O₂ we compared the energy profiles for a direct dissociative mechanism with that of a surface dissociation. For O₂ we found a precursor state where the molecule is adsorbed parallel to the surface. In this state the molecular bond is weakened and the dissociation barrier for this state is just a few kcal/mol. For NO we found a favorable dissociation mechanism whereby the molecule first adsorbs on the surface, after which it dissociates on a neighboring 2-fold site in a motion that is parallel to the surface. These findings are applicable to the NO decomposition reaction (DeNO_x). NO dissociation and N₂ recombination are the rate limiting steps of the process, until the surface is covered with oxygen atoms. The presence of CO is crucial to remove these from the surface by oxidation. In lean conditions adsorbed oxygen will therefore be unreactive, hence poisoning the copper surface.

Chapter 6 describes the influence of chlorine on the epoxidation of ethylene on Ag(110) on cluster models varying in size between 4 and 26 atoms. The first part of this study concentrated on the adsorption of oxygen atoms in the long bridge site and the changes in the adsorption parameters that were caused by introducing the promoter chlorine. Chlorine is found to weaken the oxygen surface bond. In most cases this is accompanied with a longer oxygen-surface bond length and a lowering of the oxygen-surface stretch frequency. Further study shows that the effect of chlorine on the adsorption of chlorine is rather short range: it is only weakened if it is adsorbed to the same atom as the oxygen atom. In other positions it is found in fact to increase the oxygen bond strength. Relaxation of the metal atoms close to the adsorption site stabilizes the oxygen bond with a few kcal/mol. Next we probed the influence of chlorine on the epoxidation of ethylene catalyzed by the silver surface. For the epoxidation reaction in the absence of chlorine we

found a barrier of 39 kcal/mol. The introduction of chlorine not only weakens the oxygen bond to the surface, but it was also found that to remove the barrier for an ethylene molecule approaching the oxygen atom. This study has shown that in cluster studies the effect of cluster size on adsorption energies can still be significant. By studying model systems with periodic boundary conditions (slabs) one can circumvent this artifact. Such a study is also better suited for dealing with surface relaxation and reconstruction, and for the calculation of the relative strength of different adsorption sites.

The last chapter describes a combined experimental and theoretical study on the conversion of alpha-limonene to para-cymene in zeolites. We simulated the diffusion of three cymene isomers in two zeolites, ZSM-5 and zeolite-Y. The diffusion profiles are very different for each isomer which is in agreement with the experimental measurements that show that ZSM-5 has a very high selectivity with respect to the para-cymene reaction.

!

:

Samenvatting

Het eerste deel van dit proefschrift geeft een overzicht van de belangrijkste modelerings methodes die momenteel gebruikt worden in de industriële katalyse. Toepassingen worden beschreven in, onder andere, katalysator karakterisering, elektron microscopie, simulatie van de kristal morfologie en de simulatie van diffusie van organische moleculen in poreuse materialen. Er wordt een overzicht gegeven van de belangrijkste quantum methodes voor elektronen structuur berekeningen, in het bijzonder de dichtheids functionaal theorie, als toegepast op nieuwe materialen. De theorie achter deze berekeningen wordt kort beschreven, alsmede de parallellisatie van deze programma's voor gebruik op computers met meerdere processoren. Parallellisatie van de programma's maakt berekeningen mogelijk aan systemen van realistische afmetingen in een relatief korte tijdspan. Dit is met name van belang in praktische industriële toepassingen. Toepassingen van deze methodes worden besproken aangaande de structuur van metaal clusters, C_{60} chemie, een zuurstof defect in alfa-kwarts en de structuur van *template* moleculen in de zeoliet synthese.

Het zwaartepunt van het proefschrift bestaat uit de beschrijving van elementaire reacties van moleculen op metaal oppervlakken met behulp van dichtheids functionaal theorie. Dit is een van de eerste studies in de literatuur waarbij met *ab initio* technieken de transition states bepaald zijn voor een oppervlakte reactie. Dit is mogelijk door recente ontwikkelingen in geometrie optimalisatie technieken. Bestudeerd is de dissociatie van CO en NO op cluster modellen van de Cu(111) en Cu(100) oppervlakken, door voor verschillende reactiepaden de transition states volledig te optimaliseren. De barrières voor dissociatie van CO zijn hoog voor alle reactiepaden. Omdat de adsorptie energie van CO laag is betekent dit dat CO in het algemeen niet zal dissociëren op koper oppervlakken. Voor NO hebben we barrières berekend die beduidend lager zijn dan voor CO, terwijl de oppervlakte binding voor NO beduidend sterker is dan die voor CO. Dit is een indicatie

dat dissociatie van NO aanzienlijk gemakkelijker is dan van CO, hetgeen in overeenstemming is met experimentele metingen. De transition states zijn erg *star* (hebben weinig bewegingsvrijheid) wat resulteert in een lage entropie voor deze toestand. The reactanten hebben meer bewegingsvrijheid vanwege een translatie vibratie op het oppervlak met een lage frequentie. Met behulp van transition state theorie hebben we de pre-exponentiële factoren bepaald, welke in goede overeenstemming zijn met experimentele metingen aan deze systemen.

In een volgend hoofdstuk zijn voor de vier twee-atomige moleculen CO, NO, O₂ en N₂ de adsorptie en dissociatie bestudeerd over drie verschillende sites op het (100) oppervlak van koper. Vanwege de karakteristieke elektronische structuur geeft deze set moleculen een goede indicatie van de elektronische factoren die een rol spelen voor dissociatie aan een metaal oppervlak. CO en N₂ blijken moeilijk te dissociëren op Cu(100). De dissociatie van O₂ is sterk exothermisch zonder een noemenswaardige activerings energie. De barrière voor NO dissociatie is laag en kan verlopen bij relatief lage temperaturen. Voor NO en O₂ zijn de energie profielen voor een directe dissociatieve adsorptie vergeleken met die van een oppervlakte dissociatie. Voor O₂ vonden we een precursor waarbij het molecuul is geadsorbeerd parallel aan het oppervlak. In deze toestand is de moleculaire binding al sterk verzwakt, en de dissociatie barrière voor deze toestand is slecht enkele kcal/mol. Voor NO vonden we een gunstig dissociatie mechanisme waarbij het molecuul eerst geadsorbeerd is en dan dissocieert over een naburige tweevoudige site in een beweging parallel aan het oppervlak. Deze bevindingen zijn direct toepasbaar op de NO decompositie reactie (DeNO_x). NO dissociatie en N₂ recombinitie zijn de snelheids bepalende stappen voor de reactie, totdat het oppervlak bedekt is met zuurstof atomen. De meest voor de hand liggende manier waarop deze van het oppervlak verwijderd kunnen worden is door oxidatie van CO, wat een snellere reactie stap is.

De invloed van chloride op de epoxidatie van etheen op Ag(110) is bestudeerd op cluster modellen van 4 tot 26 atomen. Het eerste gedeelte van deze studie concentreert zich op de adsorptie van zuurstof atomen in de lange brug site en de veranderingen in de adsorptie parameters onder invloed van de promotor Cl. Chloor blijkt de binding van zuurstof op het oppervlak te verzwakken. In de meeste gevallen gaat het introduceren van chloor gepaard met een langere Ag-O binding en een verlaging van de Ag-O stretch frequentie. Voor de epoxidatie reactie in de afwezigheid van Cl vonden we

een barrière van 39 kcal/mol. De promotor bewerkstelligt nog een effect: het verlaagt de repulsieve barrière voor een etheen molecuul dat een geadsorbeerd zuurstof molecuul op het metaal oppervlak nadert. Nadere studie wijst uit dat chloor de Ag-O binding vooral verzwakt als het geadsorbeerd is aan hetzelfde atoom als zuurstof. In andere posities kan het de binding juist versterken. Relaxatie van de metaal atomen dichtbij de adsorptie site stabiliseert de zuurstof binding met enige kcal/mol. Deze studie heeft uitgewezen dat in cluster studies het effect van cluster grootte of adsorptie energieën aanzienlijk kan zijn. Een studie aan model systemen met periodieke randvoorwaarden (slabs) kan dit artifact verhelpen. Zo'n studie kan is ook beter geschikt voor de bestudering van oppervlakte relaxatie en reconstructie, en voor het berekenen van de relatieve sterkte van verschillende adsorptie sites.

In het laatste hoofdstuk beschrijven we een experimentele en theoretische studie naar de conversie van α -limoneen naar para-cymeen. Hiertoe simuleerden we de diffusie van cymeen isomeren in twee zeolieten, ZSM-5 en zeoliet-Y. De diffusie patronen voor de verschillende isomeren blijken sterk te verschillen, hetgeen in overeenstemming is met de experimentele waarneming dat ZSM-5 een hoge selektiviteit heeft met betrekking tot de para-cymeen reactie.

Dankwoord

Allereerst wil ik Rutger van Santen bedanken voor het geven van de gelegenheid om dit onderzoek uit te voeren. Het was een waar genoegen om jou enthousiasme mee te mogen maken in de afgelopen jaren en ik heb veel geleerd van onze 'werk besprekingen' in Chicago, San Diego, Berlijn, Parijs, Frankfurt en, ja, ook in Eindhoven. Evert-Jan Baerends en Hans Niemantsverdriet wil ik bedanken voor de interessante discussies die we hebben gehad door de jaren heen en hun waardevolle suggesties.

I would like to thank John Newsam for creating the opportunity to do this work in San Diego, and for his 'tremendous' enthusiasm that kept me going. I also would like to thank, in no particular order (and this is by no means a complete list), colleagues Clive, Steve, Alan, Ron, Jan, Frank, Julie, and all the other people I had the pleasure working with at MSI for creating an extremely pleasant and stimulating working environment. In particular I would like to thank Sean Li for providing his bright physicist point of view during the first two years of this project. I also want to single out Christoph Kölmel's help that has been extremely valuable throughout the full period of the project; help such as keeping the DMol program running, jotting down some formulas that I would have had to look up otherwise, and assistance on many other occasions.

Uiteraard wil ik ook vrienden bedanken in Eindhoven voor het goede contact de laatste jaren. Joris, bedankt voor het kritisch doornemen van een aantal hoofdstukken, en Pieter, bedankt voor het kleurrijke ontwerp van de omslag. Ik bedank mijn ouders, broer en zus voor alle aanmoediging en vertrouwen in de afgelopen jaren. En tenslotte wil ik Hilde bedanken voor alle steun, gezelligheid, en het doorstaan van dit alles de afgelopen 4 jaar.

!

Curriculum Vitae

Ton van Daelen werd geboren op 22 Augustus 1967 in Waalwijk. Hij doorliep het VWO aan het Newman College te Breda. Na het eindexamen in 1985 begon hij de opleiding Scheikundige Technologie aan de Technische Universiteit in Eindhoven. Zijn keuzevakken waren quantum chemie, oppervlakte chemie en katalyse, en hij volgde een stage op het Koninklijke Shell Laboratorium in Amsterdam. In 1991 studeerde hij af in the vakgroep anorganische chemie en katalyse met een studie naar de invloed van kationen op de adsorptie van zwavel op iridium clusters in zeolieten.

Eind 1991 begon hij zijn promotie onderzoek bij *Biosym*, later *Molecular Simulations (MSI)* geheten, in San Diego, Californie. De resultaten van dit onderzoek zijn vastgelegd in het proefschrift dat thans voor u ligt. Naast dit onderzoek heeft hij zich ook bezig gehouden met het werk aan de quantum progamma's DMol en ontwikkelingen in de software van het *Catalysis and Sorption* project. Sinds 1 april 1996 is hij werkzaam bij MSI als product manager van de *Software Developer's Kit*.

Stellingen

behorende bij het proefschrift

Practical Application of Molecular Modeling in Heterogeneous Catalysis

Ton van Daelen

1. Het is niet verwonderlijk dat de barrières voor CO dissociatie op koper die Siegbahn berekent uitzonderlijk laag zijn. In de door hem voorgestelde transition state is het CO molecuul weliswaar gebogen maar is de CO binding niet gestretched. Omdat het hier een "late" transition state betreft is dit effect aanzienlijk.

P. Siegbahn, *Surf. Sci.*, **269/270** 276 (1992)

Hoofdstuk 4 van dit proefschrift

2. Het modeleren van oppervlakte reacties door enkel gepostuleerde stationaire punten op een potentiaal oppervlak te optimaliseren, kan in sommige gevallen een incorrecte beschrijving geven van het reactiepad.

Hoofdstuk 5 van dit proefschrift

3. Hoewel Siegbahn's concept van *bond preparation* voor adsorptie van moleculen op model clusters in veel gevallen sterk verbeterde adsorptie energieën geeft, is deze methode slechts van beperkte waarde in praktische toepassingen.

I. Panas, P. Siegbahn, and U. Wahlgren, *Chem. Phys. Lett.*, **149** 266 (1988)

4. Neyman and Roesch's voorspelling dat NO een hoge coordinatie preferereert op Ni(111) is niet goed gefundeerd vanwege tekortkomingen van de door hen gebruikte methode. Hun cluster modellen zijn te klein en de (locale) X_{α} methode is niet betrouwbaar voor het nauwkeurig voorspellen van adsorptie energieën. Van beide tekortkomingen is bekend dat ze in veel gevallen onterecht een hoge coordinatie bevoordelen.

M. Neyman and N. Rösch, *Surf. Sci.*, **307** 1193 (1994)

Dit proefschrift

5. De uitspraken die Drew *et al.* doen over de reaktiviteit van een molybdenum di-sulfide katalysator mogen gedurfd genoemd worden, gezien de beperkingen van het krachtveld model dat ze gebruiken. Hun conclusie dat moleculaire mechanica een grotere kans van success heeft voor het begrijpen van katalytische processen is tot op heden ongegrond gebleken.

M.G.B. Drew, *Catal. Today*, 2 633 (1988)

6. Parallelisatie van computer programma's is van beperkte waarde in een universitaire omgeving. Gezien de veelheid aan berekeningen die op een computer tegelijkertijd gestart worden, zou de ideale vorm van "parallelisatie" zijn het een voor een laten runnen van de jobs.

7. Dat in Amerikaanse verkiezingen de persoon van de kandidaten een grotere rol speelt dan de politieke problemen, wordt eerder veroorzaakt door de geringe politieke belangstelling van de gemiddelde Amerikaan dan door de kwaliteit van de kandidaten.

8. De druk uitgeoefend op de wetenschapper om vooral vaak te publiceren is niet bevorderlijk voor de omvang van het gepubliceerde werk.

A. Wander, *J. Phys.*, 1 183-183 (1989)

9. Voetbal zou een grotere kans van slagen hebben in de Verenigde Staten wanneer de keeper aan dezelfde regels zou worden gehouden als de veldspelers.

10. Internationale politieke ontwikkelingen van de laatste jaren bewijzen dat progressieve partijen, die voldoende lange tijd aan macht zijn, vanzelf conservatief worden.